

NAVAL POSTGRADUATE SCHOOL
Monterey, California



THESIS

AN LDV INVESTIGATION OF SUPPORT STRUCTURE
INFLUENCE ON THE FLOW FIELD NEAR THE WINGTIP
OF A STOVL CONFIGURATION IN HOVER

by

Edgar R. Enochs

September 1994

Thesis Advisor:

Co-Advisor

S. K. Hebbar

M. F. Platzer

Approved for public release; distribution is unlimited.

19950517 060

DTIC QUALITY INSPECTED 6

Unclassified

SECURITY CLASSIFICATION OF THIS PAGE

REPORT DOCUMENTATION PAGE				Form Approved OMB No. 0704-0188	
1a. REPORT SECURITY CLASSIFICATION Unclassified			1b. RESTRICTIVE MARKINGS		
2a. SECURITY CLASSIFICATION AUTHORITY			3. DISTRIBUTION/AVAILABILITY OF REPORT Approved for public release; distribution is unlimited.		
2b. DECLASSIFICATION/DOWNGRADING SCHEDULE					
4. PERFORMING ORGANIZATION REPORT NUMBER(S)			5. MONITORING ORGANIZATION REPORT NUMBER(S)		
6a. NAME OF PERFORMING ORGANIZATION Naval Postgraduate School		6b. OFFICE SYMBOL AA		7a. NAME OF MONITORING ORGANIZATION Naval Postgraduate School	
6c. ADDRESS (City, State, and ZIP Code) Monterey, CA 93943-5000				7b. ADDRESS (City, State, and ZIP Code) Monterey, CA 93943-5000	
8a. NAME OF FUNDING/SPONSORING ORGANIZATION NASA Ames Research Center		8b. OFFICE SYMBOL (If applicable) FFF		9. PROCUREMENT INSTRUMENT IDENTIFICATION NUMBER	
8c. ADDRESS (City, State, and ZIP Code) Moffet Field CA 94035-1000		10. SOURCE OF FUNDING NUMBERS			
		PROGRAM ELEMENT NO.		PROJECT NO.	TASK NO.
					WORK UNIT ACCESSION NO.
AN LDV INVESTIGATION OF SUPPORT STRUCTURE INFLUENCE ON THE FLOW FIELD NEAR THE WINGTIP OF A STOVL CONFIGURATION IN HOVER (U)					
12. PERSONAL AUTHOR(S) Enochs, Edgar R.					
13a. TYPE OF REPORT Master's Thesis		13b. TIME COVERED FROM _____ TO _____		14. DATE OF REPORT (Year,Month,Day) September 1994	
15. PAGE COUNT 134					
16. SUPPLEMENTARY NOTATION The views expressed in this thesis are those of the author and do not reflect the official policy or position of the Department of Defense or the U.S. Government.					
17. COSATI CODES			18. SUBJECT TERMS (Continue on reverse if necessary and identify by block number)		
FIELD	GROUP	SUB-GROUP			
			LDV, SUPPORT STRUCTURE, FLOW FIELD, ASTOVL, STOVL, OARF.		
19. ABSTRACT (Continue on reverse if necessary and identify by block number) Acquisition phase zero (Concept Exploration) of the Advanced Short Takeoff/ Vertical Land (ASTOVL) aircraft development includes, among other tests, evaluation of forces and moments on a large-scale powered model (LSPM) suspended in the Outdoor Aerodynamic Research Facility (OARF) at the NASA Ames Research Center. This investigation assessed the influence of the OARF support structure upon the flow field through LDV measurements in the vicinity of the struts and the wingtip of a generic flat-plate model mounted in the sub-scale NPS ground-effects test rig. The model was a twin subcritical jet configuration with the nozzles arranged in tandem. The test environment was saturation seeded using a smoke generator and LDV measurements were made in the entrained flow. Non-coincident measurements were made to determine the three component mean velocities at points in the region of interest and the component mean and composite mean velocities compared for configurations with struts present and struts removed. Variations were discernible in the component mean velocities between samples both in the same strut configuration and between the struts-installed and struts-removed configurations, but were generally small enough to be considered negligible.					
20. DISTRIBUTION/AVAILABILITY OF ABSTRACT <input checked="" type="checkbox"/> UNCLASSIFIED/UNLIMITED <input type="checkbox"/> SAME AS RPT. <input type="checkbox"/> DTIC USERS			21. ABSTRACT SECURITY CLASSIFICATION Unclassified		
22a. NAME OF RESPONSIBLE INDIVIDUAL S. K. Hebbar			22b. TELEPHONE (Include Area Code) (408) - 656 - 2997		22c. OFFICE SYMBOL AA/Hb

DD Form 1473, 84 MAR

83 APR edition may be used until exhausted

SECURITY CLASSIFICATION OF THIS PAGE

All other editions are obsolete

Unclassified

Approved for public release; distribution is unlimited.

An LDV Investigation of Support Structure Influence on the Flow Field near the
Wingtip of a STOVL Configuration in Hover

by

Edgar R. Enochs
Commander, United States Navy
B.S. United States Naval Academy, 1977

Submitted in partial fulfillment
of the requirements for the degree of

MASTER OF SCIENCE IN AERONAUTICAL ENGINEERING


from the

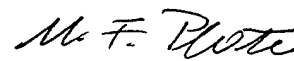
NAVAL POSTGRADUATE SCHOOL
SEPTEMBER 1994

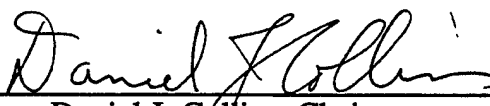
Author:


Edgar R. Enochs

Approved by :


S. K. Hebbar, Thesis Advisor


M. F. Platzer, Co-Advisor


Daniel J. Collins, Chairman
Department of Aeronautics and Astronautics

ABSTRACT

Acquisition phase zero (Concept Exploration) of the Advanced Short Takeoff/Vertical Land (ASTOVL) aircraft development includes, among other tests, evaluation of forces and moments on a large-scale powered model (LSPM) suspended in the Outdoor Aerodynamic Research Facility (OARF) at the NASA Ames Research Center. This investigation assessed the influence of the OARF support structure upon the flow field through LDV measurements in the vicinity of the struts and the wingtip of a generic flat-plate model mounted in the sub-scale NPS ground-effects test rig. The model was a twin subcritical jet configuration with the nozzles arranged in tandem. The test environment was saturation seeded using a smoke generator and LDV measurements were made in the entrained flow. Non-coincident measurements were made to determine the three component mean velocities at points in the region of interest and the component mean and composite mean velocities compared for configurations with struts present and struts removed. Variations were discernible in the component mean velocities between samples both in the same strut configuration and between the struts-installed and struts-removed configurations, but were generally small enough to be considered negligible.

Accession For	
NTIS GRA&I	<input checked="checked" type="checkbox"/>
DTIC TAB	<input type="checkbox"/>
Unannounced	<input type="checkbox"/>
Justification	
By	
Distribution/	
Availability Codes	
Dist	Avail and/or Special
A-1	

TABLE OF CONTENTS

I. INTRODUCTION	1
A. BACKGROUND	1
1. ASTOVL Development	1
2. VTOL Propulsion Aerodynamics in Hover	5
B. PURPOSE	6
C. SCOPE	7
II. EXPERIMENTAL APPARATUS	9
A. INTRODUCTION	9
B. MODEL AND STRUT CONFIGURATION	11
C. OPTICAL PROBE AND TRAVERSE MECHANISM	12
D. LDV SYSTEM	15
1. Laser and Optics Subsystem	16
2. Data Acquisition and Processing Subsystem	18
3. Particle Seeding Subsystem	22
E. CALIBRATION RIG	24
III. EXPERIMENTAL PROCEDURES	27
A. PROBE OPTICS	27
1. Mounting and Alignment	27
2. Half-angle Measurement	28
B. TRAVERSE	28
C. TEST MATRIX.....	31
1. Selection of Test Conditions	31
2. Selection of Test Coordinates	32
D. CALIBRATION.....	33
1. Pre-Calibration Surveys	33
2. Calibration Test.....	35
E. DATA COLLECTION	36
1. Control and Monitoring of Test Conditions.....	36

2. Data Acquisition Software Configuration	36
3. Order of Test Data Sets	36
4. Seeding	37
F. POST-TEST DATA ANALYSIS	37
IV. RESULTS AND DISCUSSION	38
A. EXPERIMENTAL ACCURACY	38
B. REPEATABILITY	43
1. Statistical Confidence Intervals	44
2. Short-term Velocity Variations	44
C. VARIATION OF COMPONENT MEAN VELOCITIES	45
1. Qualitative analysis	52
2. Quantitative Analysis	53
V. CONCLUSIONS	55
A. CONFIDENCE IN MEASUREMENTS	55
B. MEAN VELOCITIES	55
C. SHORT-TERM FLOW FIELD VARIATIONS	55
D. SUMMARY	56
VI. RECOMMENDATIONS	57
A. SEED PARTICLE CHARACTERISTICS	57
B. SURFACE PRESSURE MEASUREMENTS	57
APPENDIX A. SAMPLE CALCULATIONS	59
A. MEASUREMENT UNCERTAINTIES	60
B. CONFIDENCE INTERVALS	61
APPENDIX B. REDUCED TEST DATA	62
REFERENCES	124
INITIAL DISTRIBUTION LIST	126

ACKNOWLEDGMENTS

I am deeply indebted to my thesis advisors Professors S. K. Hebbar and M. F. Platzer for their support, guidance, and patience throughout the thesis process. The time and effort they expended keeping me headed in the right direction was invaluable.

I owe a special debt of gratitude to Professor Garth Hobson for his seemingly endless reservoir of patience in the face of my frequent interruptions of his work with queries about LDV systems.

Although not funded by NASA Ames Research Center, the goal of this thesis was to provide quantifiable data to supplement the efforts begun by LCDR Bill Dooley in support of NASA Ames' portion of the ASTOVL development program. The technical assistance of Messrs. Rich Margason and Clif Horne is gratefully acknowledged.

I would also like to express my appreciation to Mr. Rick Still for his assistance and patience in setting up, operating, and maintaining the Ground-Effects Test Rig and the LDV System components that composed the test apparatus.

Finally, I would like to thank my wife Pamela and my daughters Molly and Joy for their unconditional love and support.

I. INTRODUCTION

A. BACKGROUND

1. ASTOVL Development

The Advanced Research Projects Agency (ARPA) has awarded contracts to three contractors for Acquisition Phase Zero (Concept Exploration/ Demonstration: CE/D) development related to the Advanced Short-Takeoff/ Vertical-Landing (ASTOVL) aircraft. In addition to replacing the AV-8B HARRIER II currently operated by the U. S. Marine Corps, ASTOVL may be a candidate technology for the Joint Advanced Strike Technology (JAST) program. Reference 1 notes comments from the House Armed Services Committee during its markup of the Fiscal 1995 Defense Authorization Bill indicating a desire to merge the JAST and ASTOVL programs prior to 1996.

Contractors participating in ASTOVL CE/D with ARPA funding include Lockheed Advanced Development Company (LADC), McDonnell Douglas (MD), and Boeing. Artist's conceptions of the LADC and MD ASTOVL designs are presented in Figures I.1 and I.2. LADC and MD have been on contract since March 1993, while Boeing entered the competition in May 1993. Additionally, Northrop Grumman Corporation is proceeding with a company-funded, independent research and development (IR&D) effort. At the conclusion of the CE/D effort, ARPA (or potentially JAST) will select a design and contractor to transition to Acquisition Phase I (Demonstration/ Validation: DEM/VAL) in 1996 with a projected first flight of the prototype as early as 1998.

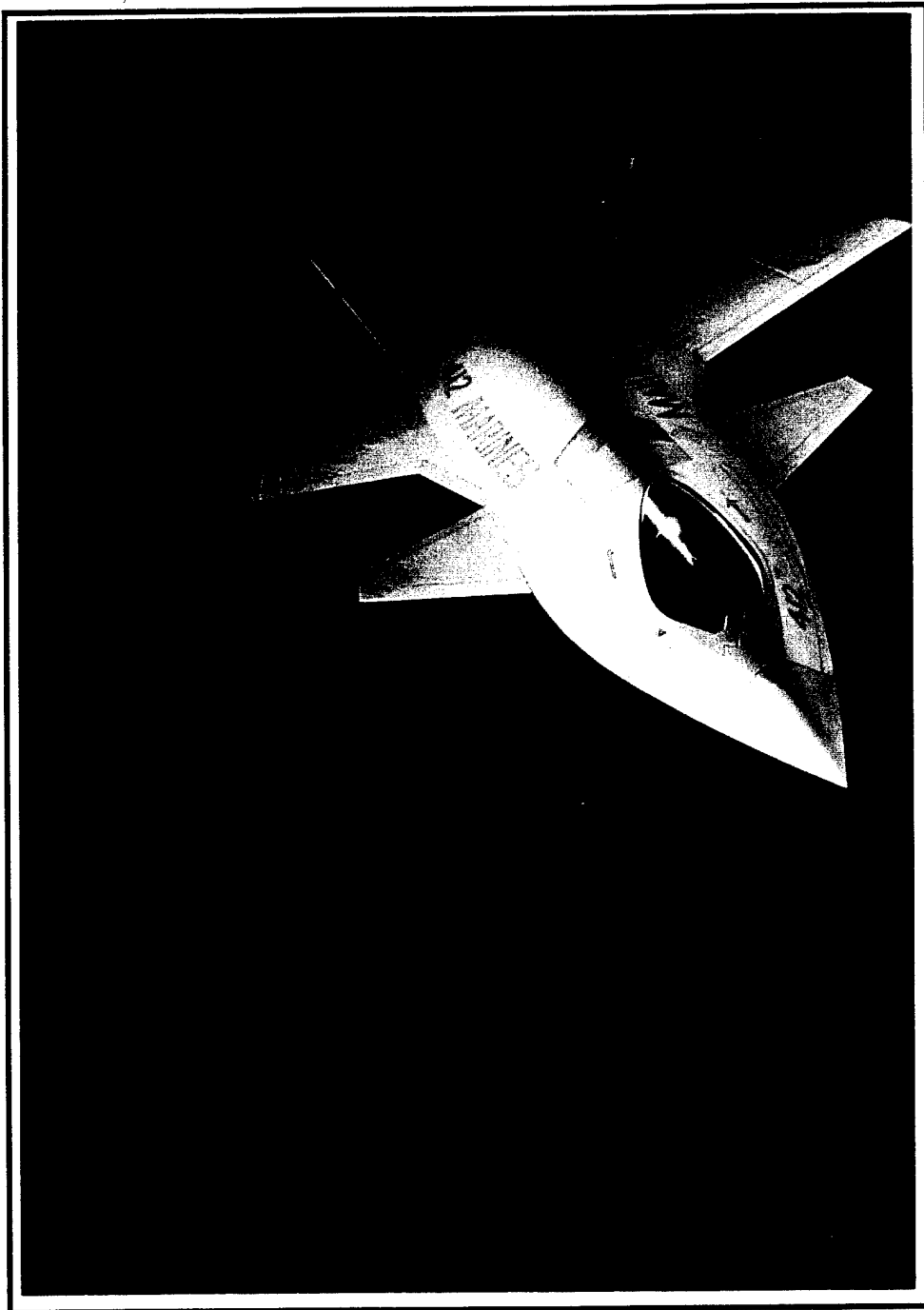


**Figure I.1 Photograph depicting Artist's Conception of Lockheed
ASTOVL Design**

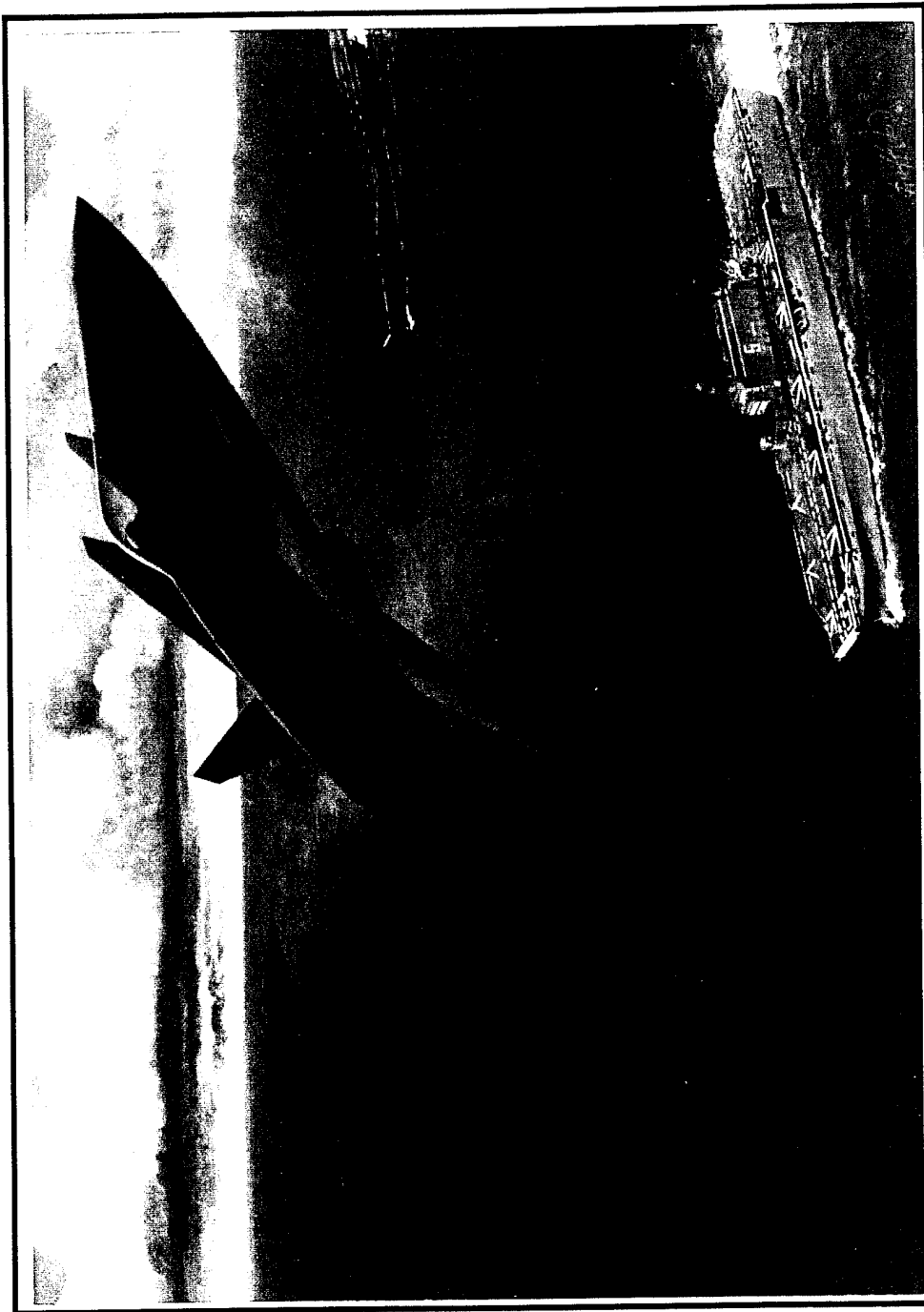


**Figure I.2 Photograph depicting Artist's Conception of McDonnell
Douglas ASTOVL Design**

Both the LADC and MD designs are powered by a single turbofan engine: the Pratt and Whitney F-119 and the General Electric F-120 engines,

respectively. Both designs also incorporate an engine-driven lift fan mounted in the forward fuselage: the LADC variant is shaft-driven and the MD design uses a gas-coupled fan. Although the details of the two proprietary designs are different, propulsive lift is provided at the aft portion of the fuselage by directed engine exhaust in both designs.

CE/D propulsion- and flight control-related development efforts include a variety of component-level test rig tests and wind tunnel model tests. LADC and MD also plan to develop Large-Scale Powered Models (LSPM). These models will be used to evaluate propulsion and stability and control (S&C) characteristics during hover in the NASA Ames Outdoor Aerodynamic Research Facility (OARF) and during transition from hover to and from wing-borne flight in the NASA Ames 80 ft x 120 ft wind tunnel.

The current OARF design comprises three telescoping struts that support a modified T-frame carriage structure which, in turn, attaches to and supports the LSPM through load cells. A three-view engineering drawing of the OARF with a generic wedge depicted attached to the carriage structure is presented in Figure I.3. OARF load cell measurements will be used to validate predicted propulsive lift performance and stability derivatives in the hover mode.

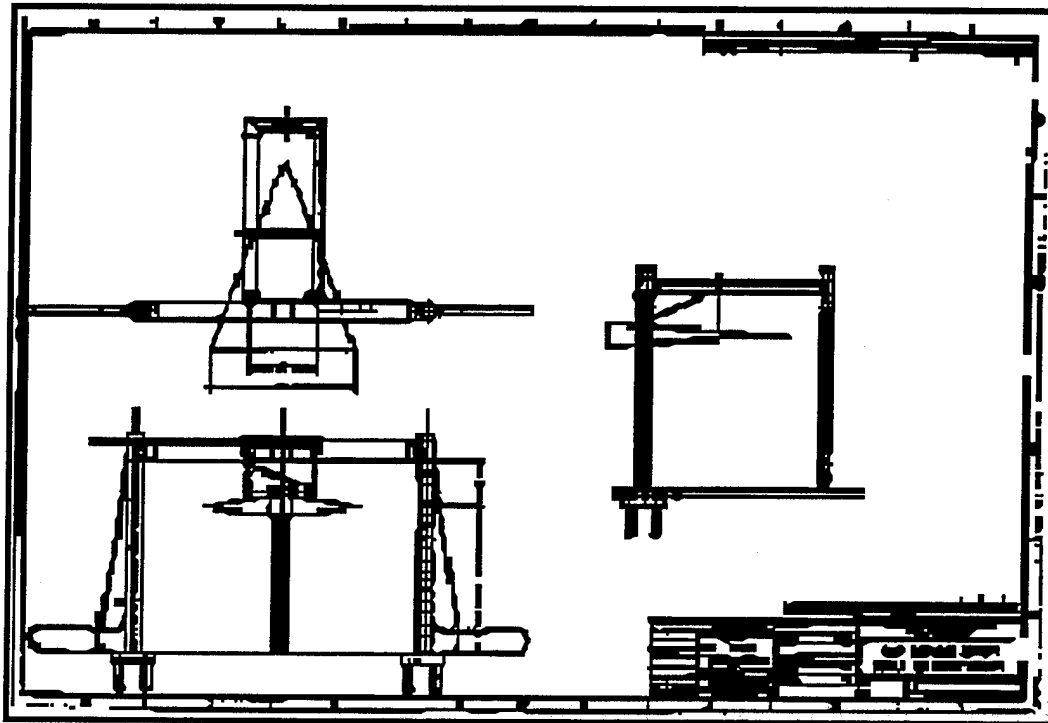


Figure I.3 Three-View Engineering Drawing NASA Ames Outdoor Aerodynamic Research Facility (OARF)

The validity of the planned OARF test results will be strongly dependent upon the degree of fidelity of the OARF-LSPM flow field with that surrounding the ASTOVL prototype in free-flight. Accordingly, an assessment of the influence of the OARF support structure upon the flow field is required as part of the CE/D effort.

2. VTOL Propulsion Aerodynamics in Hover

Reference 2 provides an excellent overview of the phenomena associated with jet V/STOL propulsion aerodynamics during hover and transition. Of particular interest in the OARF tests are the thrust-induced performance effects of "suckdown" (aerodynamic loads from entrained flow), fountain impingement on the lower fuselage, and hot-gas ingestion. The former two effects can change significantly the forces and moments acting on the vehicle as it transitions between hover-out-of-ground-effect (HOGE) and

hover-in-ground-effect (HIGE) or with small pitch and roll attitude changes during HIGE. Figure I.4 illustrates the dominant flow characteristics of a tandem nozzle configuration during jet-borne HIGE.

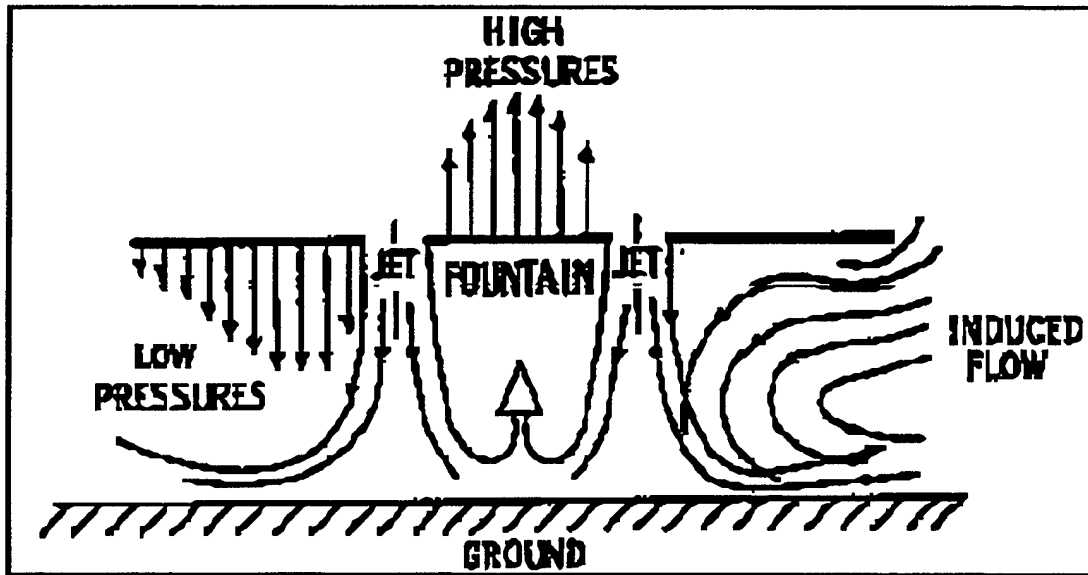


Figure I.4 Dominant Flow Characteristics of a Tandem Nozzle Configuration during Jet-Borne Hover-in Ground-Effect

Sub-scale OARF-configuration vs no-strut tests of a simple lifting jet model similar in planform and nozzle configuration to the LADC LSPM have been conducted previously for ASTOVL development risk-reduction (Reference 3). Those tests concentrated on the influence of the OARF struts on the location of the ground plane stagnation line. Measurement of the flow field characteristics near the surface of the model affords an additional measure of risk reduction by quantifying the measurable effects of the struts on the flow that directly affects forces and moments on the vehicle.

B. PURPOSE

The purpose of this investigation was to evaluate the influence of support struts modeling the OARF configuration on the flow-field in the

vicinity of the left wingtip of a generic flat-plate model STOVL configuration. Quantitative measurements of flow velocities were intended to supplement the data provided to NASA Ames Research Center by Dooley (Reference 3) from his ground plane flow visualization experiments.

C. SCOPE

Using Laser Doppler Velocimetry (LDV), this investigation measured three orthogonal components of velocity at various locations near the left wingtip of a flat-plate ASTOVL planform installed in the Naval Postgraduate School (NPS) ground-effect test rig. Measurements were taken with and without the dowels that simulate the NASA Ames OARF struts. Data were collected at a single height-above-ground-plane and single set (fore and aft) of nozzle pressure ratios. Measurements were also taken near the strut location.

The height-above-ground-plane and the set of nozzle pressure ratios used for this investigation were chosen based primarily upon the results reported in Reference 3. The set of nozzle pressure ratios chosen produced the greatest change in ground stagnation line location. The height-above-ground-plane chosen produced the second largest change with that parameter, but was chosen because its scale height corresponded to the height at which pilot workload is greatest during vertical takeoff and landing. Contamination of test data at this height by the influence of the OARF support structure would be of the greatest consequence in those planned tests.

Because of hardware limitations, the LDV measurements were non-coincident --- the three component measurements were not taken simultaneously. Each LDV data sample consisted of nominally 1024 points. At least two samples were taken for each velocity component, at each test location, for each strut configuration (installed/removed). The data samples

were reduced using a proprietary software application developed by the manufacturer of LDV hardware components. The mean velocity and standard deviation of each data sample were used to compare the statistical repeatability of measurements for a given set of test conditions and to determine whether statistically significant changes occurred with changes in the strut configuration.

The three component mean velocities at each test location were combined vectorially and plotted graphically to aid in visualization of the mean flow. The results were the equivalent of what one might visualize as segmented "oil streaks in the air" --- vectors that are tangent to the mean pathline of particles passing the point at the vector origin.

II. EXPERIMENTAL APPARATUS

A. INTRODUCTION

The ground effects test rig and model used for this investigation compose the same apparatus used by Dooley (Reference 3) in his ground plane oil flow visualization experiments. A flat-plate model with planform dimensions representing a compromise between the LADC and MD LSPM designs was flush-mounted to two vertically-oriented, circular cross-section, convergent nozzles. The nozzle air supply pressures were controlled and regulated independently to achieve the prescribed nozzle pressure ratios. Commercially manufactured, circular cross-section PVC pipes and a wooden dowel were mounted vertically on the sheet aluminum-covered "ground plane" to simulate struts. A detailed description of the construction and control mechanization of the rig is presented in Reference 3.

The LDV optical probes and the traverse mechanism on which they were mounted were the only new components introduced into the region near (within three wingspans of centerline) the model. They were positioned and oriented to minimize their potential influence on the flow field. Two photographs of the test rig are presented in Figures II.1 and II.2.

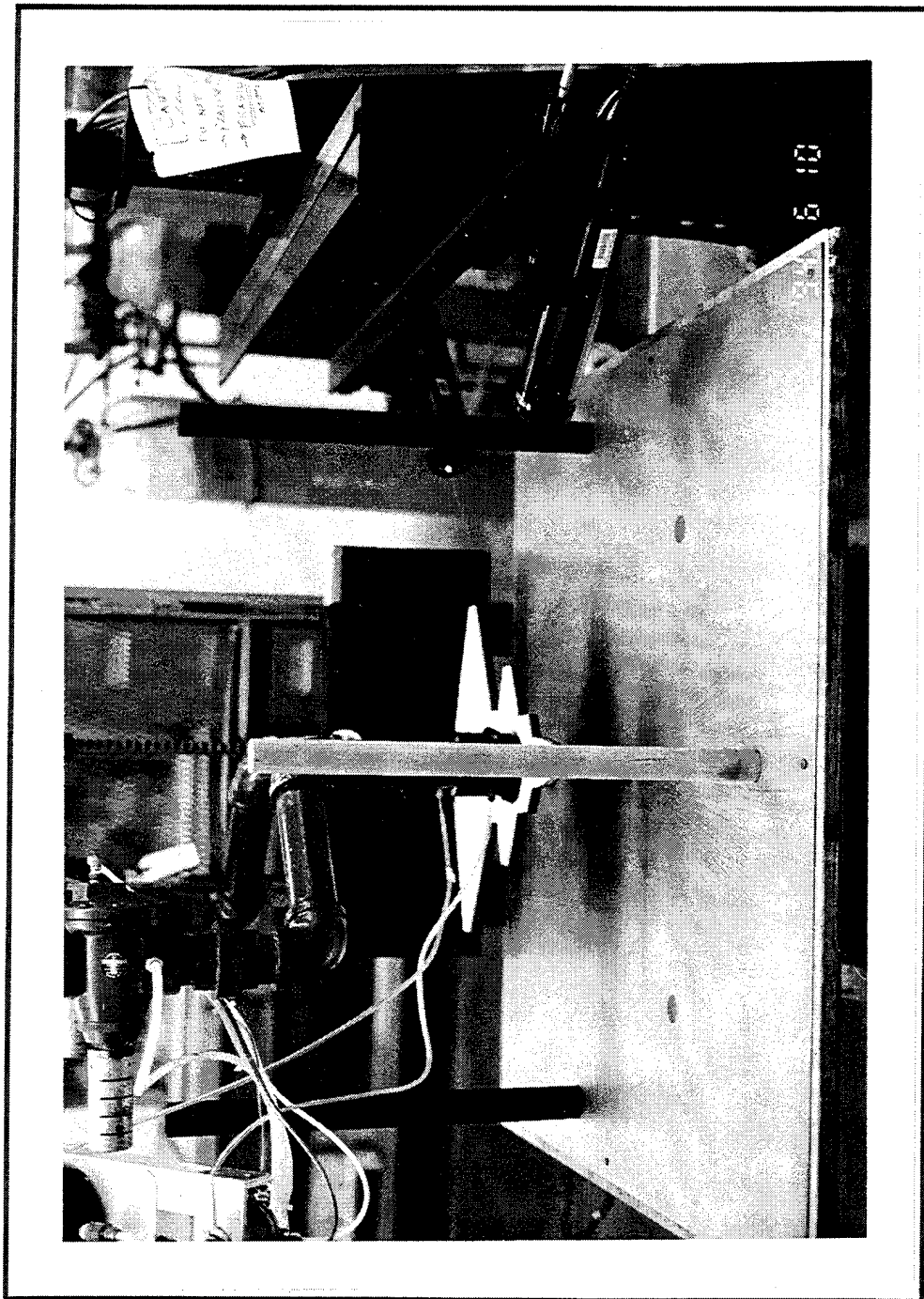


Figure II.1 Photograph showing Model Centerline View of NPS Ground
Effects Test Rig

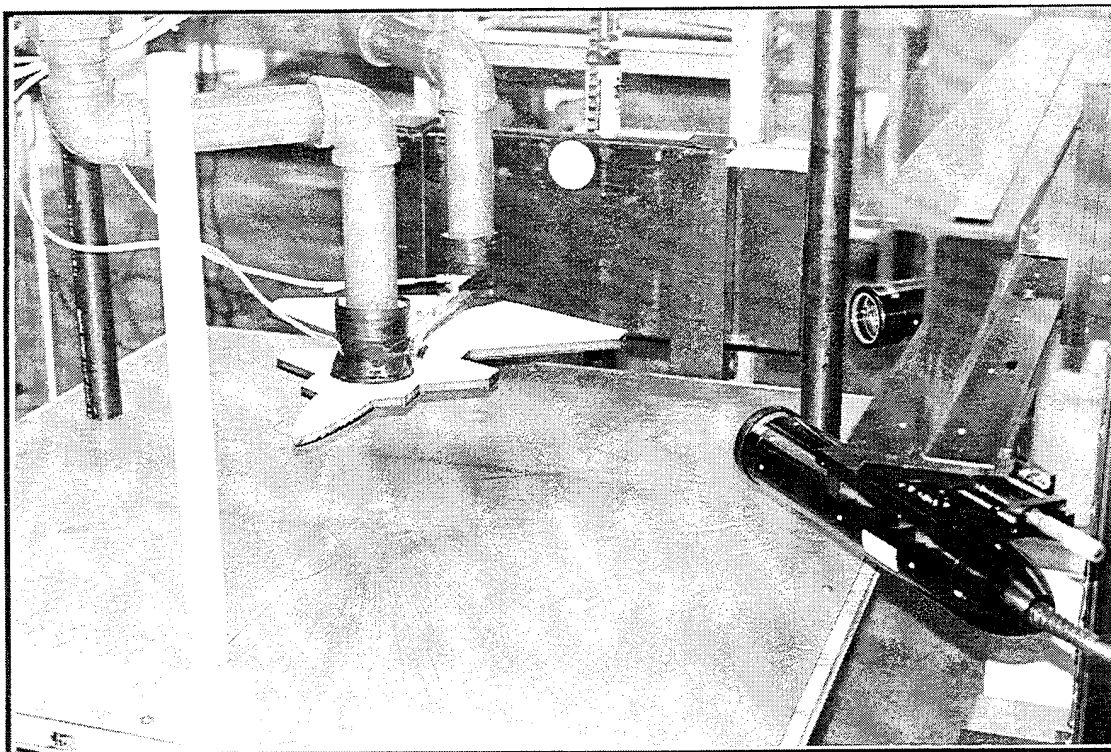


Figure II.2 Photograph showing Off-model Centerline View of Ground Effects Test Rig

B. MODEL AND STRUT CONFIGURATION

The model used for this investigation was the LADC two-nozzle configuration. Model scale factor was predicated upon the effective diameter of the LSPM lift fan compared to the one inch diameter of the forward nozzle in the test rig. The methodology for determining effective area and effective diameter of the nozzles is detailed in Reference 4 . The struts were configured to simulate the OARF configuration with 80 ft separation between main struts. A drawing depicting the test rig strut geometry is presented in Figure II.3. The actual nominal outside diameters of the PVC pipes simulating the main struts and the wooden dowel simulating the forward strut were 2 and 1 1/2 inches, respectively. The ground plane was positioned six inches beneath the exit plane of the nozzles.

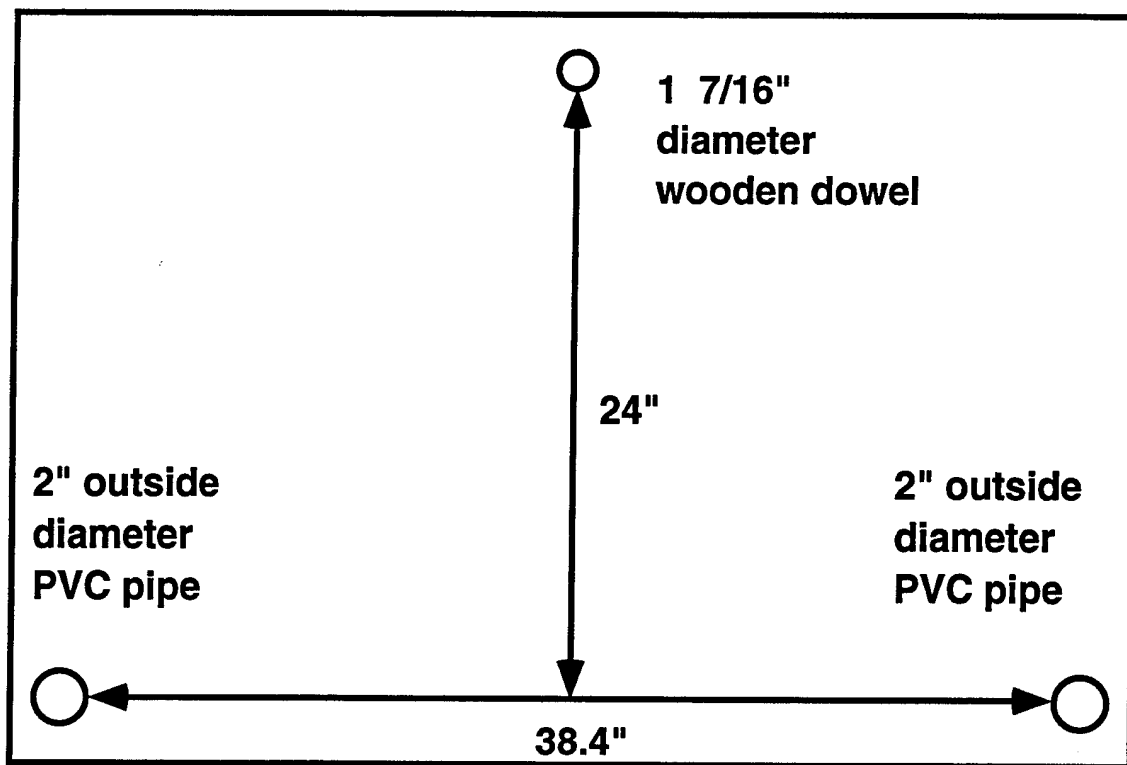


Figure II.3 Sketch of Test Rig Strut Geometry

C. OPTICAL PROBE AND TRAVERSE MECHANISM

Two TSI Inc.-manufactured optical probes were used for this investigation. A horizontally-oriented, single-component probe was mounted on one end of a steel "I-beam" and a two-component probe was mounted on the opposite end. The probes were positioned such that the centerline axes of the two probes were orthogonal to each other and their probe volumes were coincident. The probe axes formed an isosceles triangle with the I-beam at the base. This orientation allowed direct measurement of three orthogonal components of velocity and eliminated the requirement to

resolve and transform velocities into the desired coordinate system had the probes not been so oriented.

The I-beam was attached to a manually-controlled, electrically-driven traverse mechanism that is designed to provide a range of motion of 600 mm with an accuracy of ± 0.005 mm along each of three orthogonal axes. Since velocity components measured by the LDV system were oriented orthogonally to the centerline axis of their respective probes, the LDV velocity and traverse mechanism coordinate systems were not coincident. A photograph of the probes mounted on the traverse mechanism I-beam is presented in Figure II.4. The traverse system control panel is visible in the lower right corner of Figure II.5. A sketch of the orientation of the LDV velocity and traverse mechanism coordinate systems is presented in Figure II.6. A detailed description of the survey process and a physical description of the reference points chosen to orient the LDV velocity and traverse mechanism coordinate systems is presented in Chapter III.

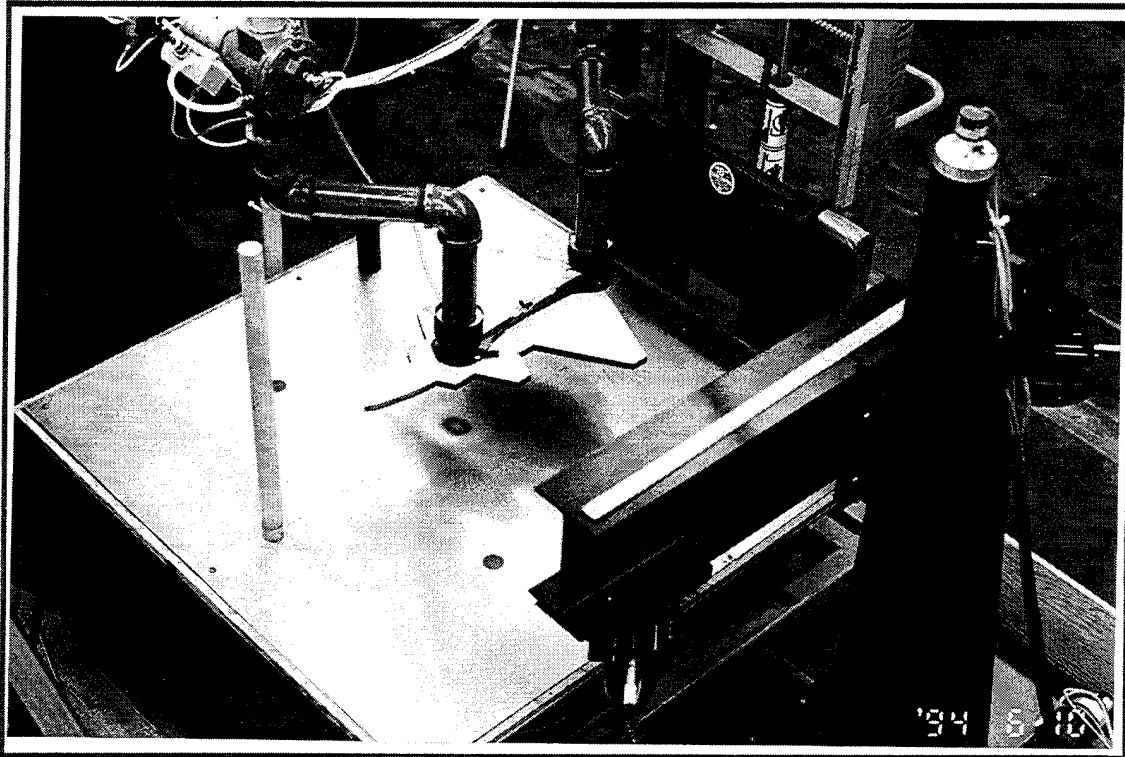


Figure II.4 Photograph of LDV Optics Probes on Traverse Mechanism

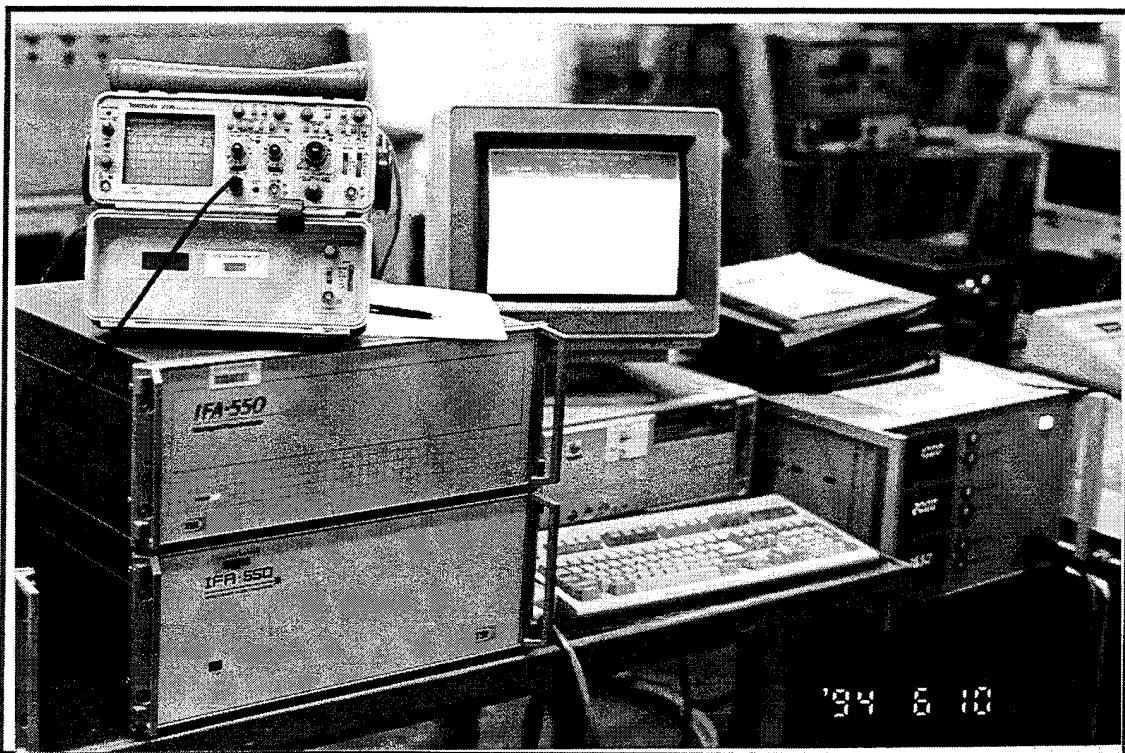


Figure II.5 Photograph of Traverse Mechanism Control Panel

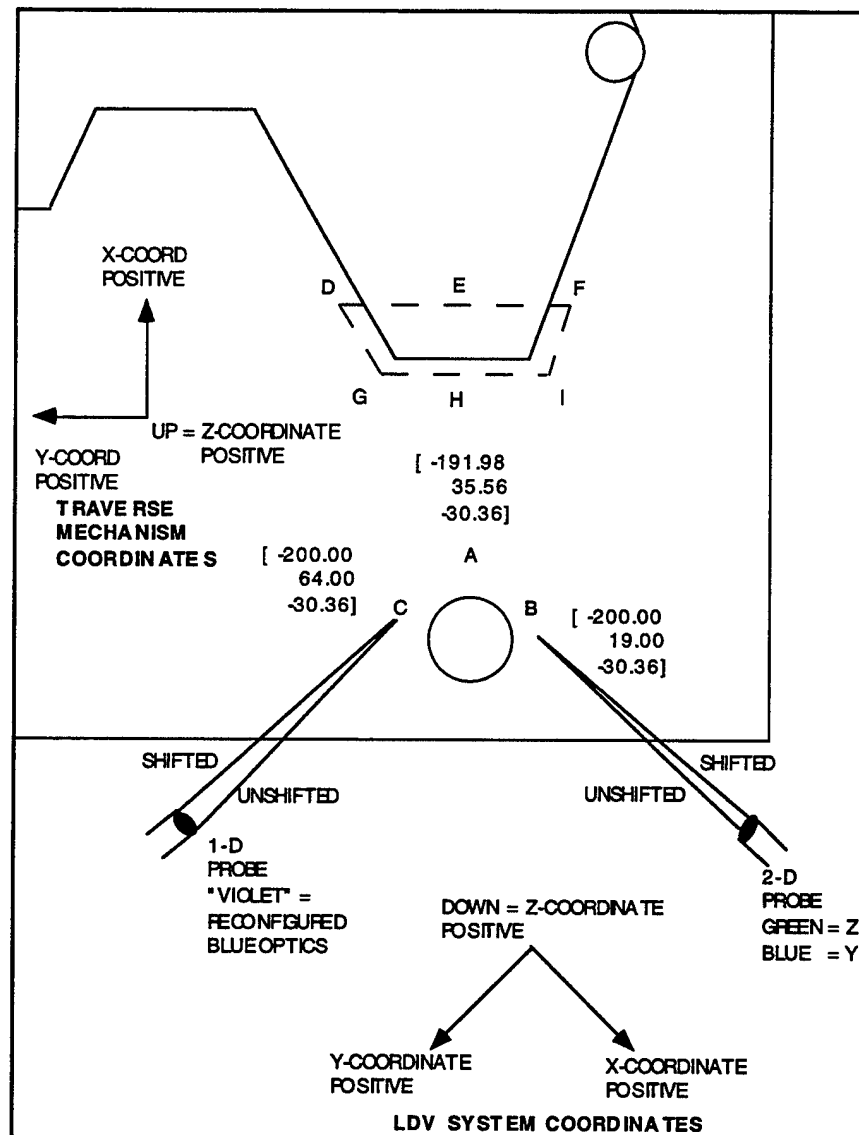


Figure II.6 LDV Velocity and Traverse Mechanism Coordinate Systems

D. LDV SYSTEM

The LDV system comprises three major subsystems: the laser and optics subsystem, the data acquisition and processing subsystem, and the particle seeding subsystem.

1. Laser and Optics Subsystem

The laser source used for this investigation was Omnicrome Model 543 air-cooled, Argon laser. This laser is rated at a maximum output power of 300 mW. Based upon results of initial tests designed to establish a single optimum set of LDV system parameters to achieve acceptable data rates at all the planned test coordinates, the laser was operated at 150 mW for these tests. The laser was aligned to radiate directly into a TSI Model 9201 Multicolor Beam Separator.

Within the beam separator the beam was bifurcated and one of the beams was passed through a Bragg cell to impart the desired frequency shift. The unaltered reference beam and the shifted beam were then passed through a prism assembly for color separation. The beams were separated into three pairs of green (514.0 nm), blue (488.0 nm), and violet (476.5 nm) beams. The green and blue beams were then reflected into two pairs of vertically-oriented optical couplers. The violet beams terminated at a blank-off plate within the beam separator.

The optical couplers were used to steer and focus the waists of the beams onto the origins of the transmitting optics fibers attached to the end of the coupler barrels. To preserve the polarization established inside the beam separator, the optical fibers are extruded with an elliptical cross section and mounted to a threaded cap with a reference post. When the cap is attached to the coupler with its post inserted into a groove cut across the threads around the opening atop the vertically-mounted coupler, the fiber is properly oriented.

The optical fiber transmits the laser energy to the TSI optics probe. The termini of the transmitting fibers are separated laterally by nominally 50 mm. After passing through beam-expanding and collimating optics, a convex

lens at the end of the probe focuses and steers the waists of the reference and shifted beams to an intersection nominally 350 mm from the face of the probe.

Scattered light from the probe volume is captured and focused onto the origin of the receiving optical fiber located on the centerline of the probe by the same convex lens used to focus and steer the transmitted light. The single receiving optical fiber terminus projected the reflected light directly into a TSI Model 9162 photomultiplier powered by a Model 916503 photomultiplier power supply. Since the photomultiplier responds to the spectra of reflected energy produced by "moving" interference fringes modulating illumination on the particles, polarization of the received energy need not be preserved.

Because only a single photomultiplier was available, velocity measurements were made a single component at a time. For example, when using the two-component probe, a data sample set was acquired with only the green, vertically-oriented beams radiating. The green beams were then masked and the blue beams, unmasked. A data set was then acquired using the horizontally-oriented blue beams.

Since only two pairs of optical couplers were available, the third velocity component, normally measured using a violet beam transmitted and received through the one-component probe, was measured using reconfigured optics. The transmitting optics fibers from the two-component probe that were attached to the blue coupler set were replaced by the transmitting fibers from the one-component probe. Similarly, the receiving optics fiber from the two-component probe was replaced by the receiving fibers from the one-component probe at the photomultiplier.

A TSI Model 9186A-4 frequency shifter controller was used both to select a discrete incremental shift of up to ± 5 MHz that was superimposed on the 40 MHz shift created by the Bragg cell and to accomplish downmixing of the signals from the photomultiplier. The output from the frequency shift controller -- the spectra resulting from the selected frequency shift combined with the doppler-induced spectra --- were output to a TSI IFA 550 Signal Processor. A detailed description of the laser and optics subsystem components is presented in References 5 through 7. Photographs of the subsystem components are presented in Figure II.7.

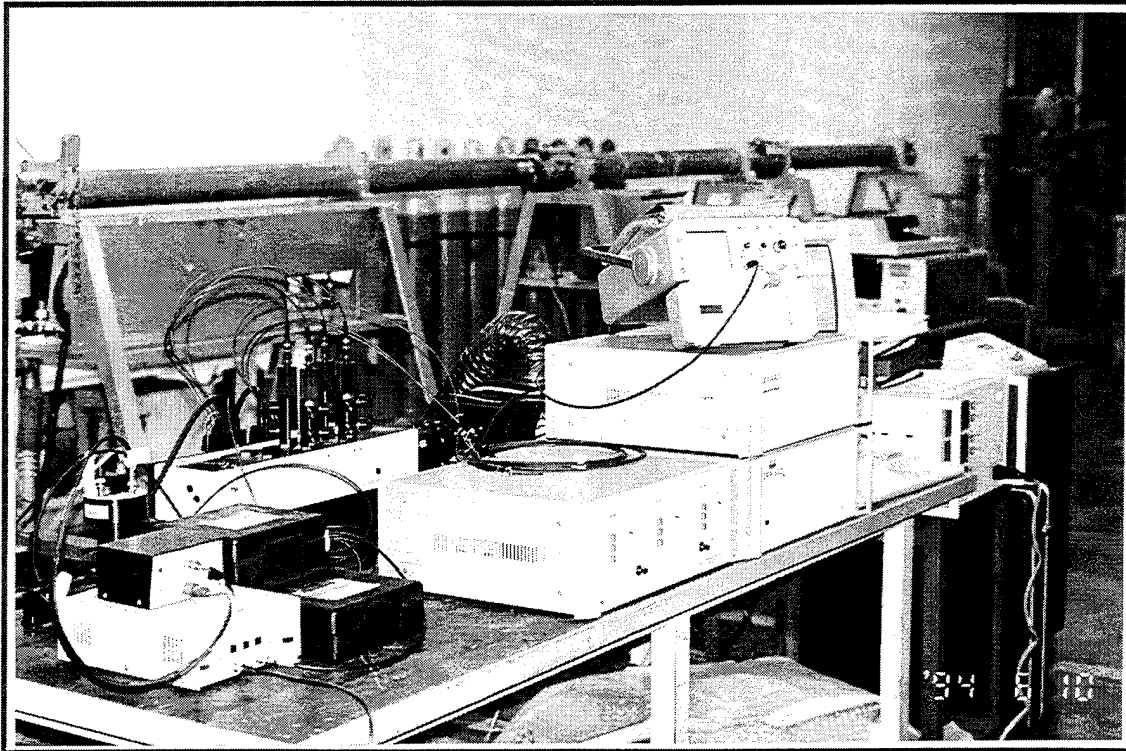


Figure II.7 Photograph of Laser & Optics Subsystem Components

2. Data Acquisition and Processing Subsystem

The data acquisition and processing subsystem comprises a single TSI IFA 550 Signal Processor integrated with an IMB PC-AT running TSI-

proprietary Flow Information Display (FIND) Software Version 3.5. Additionally, an oscilloscope was used to monitor qualitatively the character of the time-domain signals provided to the signal processor. A photograph of the subsystem components is presented in Figure II.8.



Figure II.8 Photograph of Data Acquisition and Processing Subsystem Components

Downmixed time-domain signals from the frequency shift controller were input to the signal processor where internal logic measured the time for eight cycles above the specified threshold within a given doppler burst. Predicated on manually-entered parameters of wavelength, probe beam geometry or half-angle, and selected frequency shift, the software calculated the algebraic sum of the doppler shift and the selected shift frequency or the particle component velocity for the sample point and added the point to the data sample set.

The FIND software provided the capability to collect, analyze, and display component velocity data sets as histograms and as summary tables of statistical attributes such as the sample size, mean, and standard deviation either real-time or after a prescribed number of data points had been collected. Examples of these displays extracted from Reference 8 are presented in Figures II.8 and II.9. The data sets addressed in Chapter IV were collected using the latter method, generally with a sample size of 1024 points, although in two cases 4096 points were collected. Real-time histograms provided a means to qualitatively assess the degree of unsteadiness in the flow (e.g. discernible migration or fluctuations in the location of the peak of the histogram would indicate relatively low-frequency, non-random variations of the mean flow velocity, that is, a significant short-term influence on the mean flow field from an unsteady component).

A detailed description of the data acquisition and processing subsystem components and their design performance characteristics is provided in References 8 and 9.

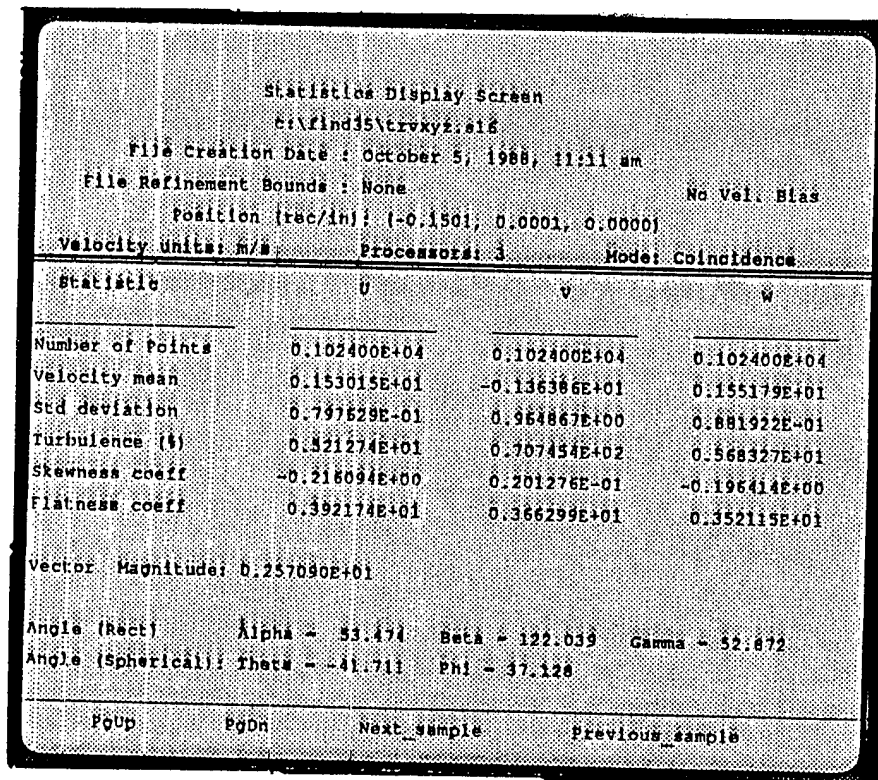


Figure II.8 Sample Statistics Display

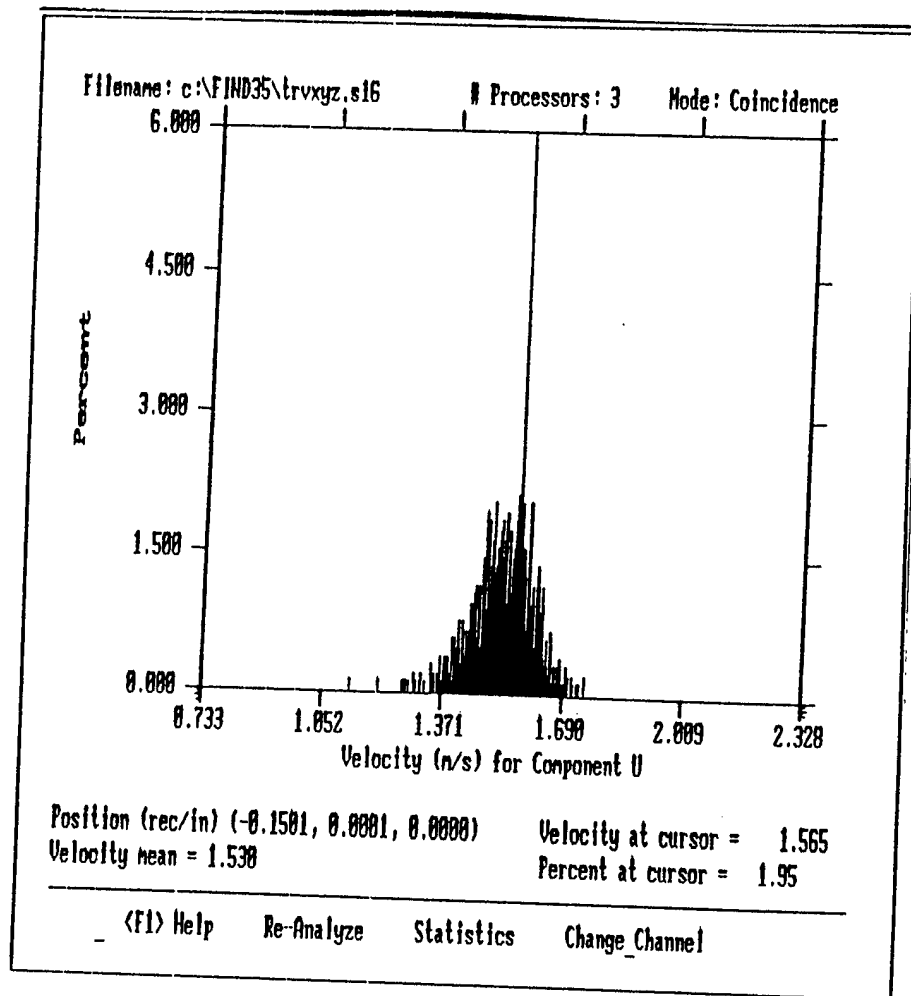


Figure II.9 Sample Histogram Display

3. Particle Seeding Subsystem

Initial attempts to seed the flow in the region of interest with distilled water and with glycerin emitted from two different wands attached to a TSI atomizer produced unacceptable results. Data rates were generally very low (less than 10 Hz) and often intermittent. Periods of five to ten seconds with no data points being collected were not uncommon. When the wand was held at an acceptable distance away from the probe volume --- more than 10 outside-diameters of the wand --- visible scattering of the light in the probe volume was often intermittent. This observation, combined with the

observed intermittent data rates was interpreted as the effect of unsteady flow on the pathlines in the region of interest. Described simplistically, the locus of points in a plane upstream of the point of interest through which the flow passed enroute to that point of interest was of greater area than the area seeded by the wand. Seeding by this method would have contaminated the sets of velocity data by imposing physical restrictions on which particle velocities were actually measured --- when the instantaneous velocity within the probe volume was tangent to a pathline not passing through the effective discharge area of the wand, no artificial seed would be in the flow and a velocity measurement would not be recorded. Accordingly, saturation seeding of the test space using a Rosco Model 1500 Fog Machine was chosen for these tests. The machine was mounted atop a nine-foot step ladder with the discharge port elevated approximately twenty degrees. A detailed description of the fog machine and its operating characteristics is provided in Reference 10. A photograph of the machine discharging smoke is presented in Figure II.10.

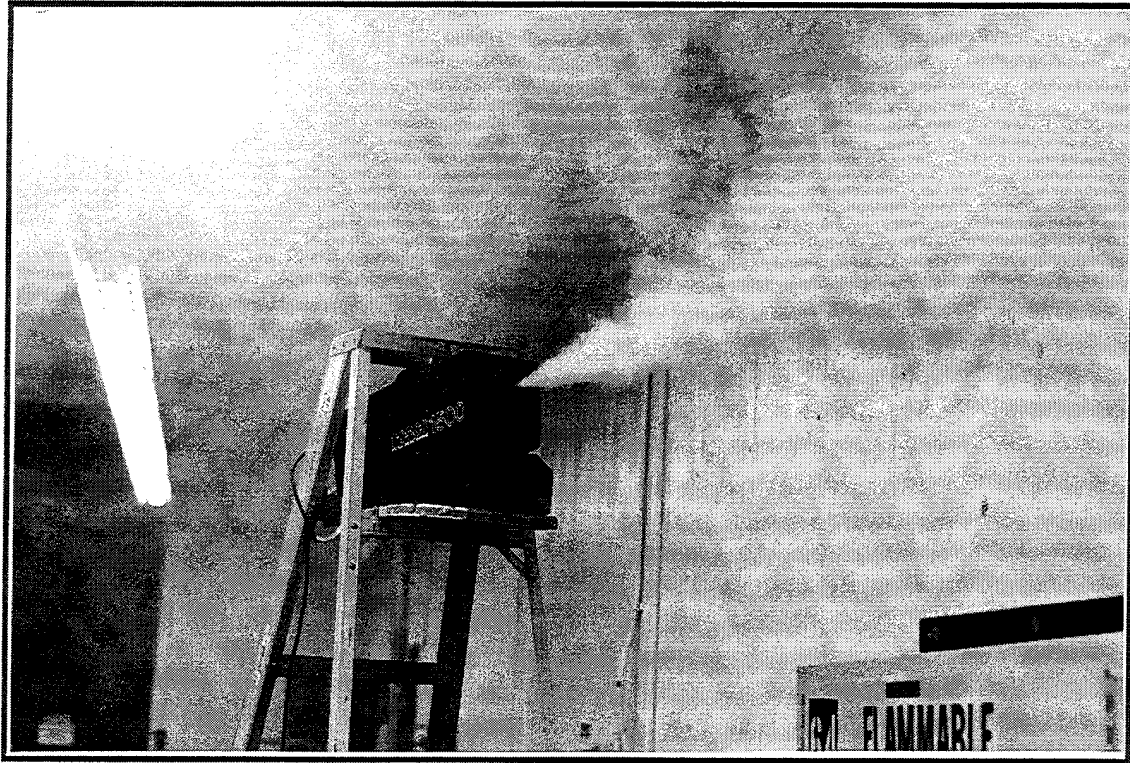


Figure II.10 Photograph of Rosco Fog Machine Discharging Smoke

According to the reference, particles emitted from the machine vary in diameter from 0.25 to 50 microns. Data were not available detailing the distribution of particles by size nor was a determination made experimentally. Those data were not considered meaningful in that buoyancy effects in the saturation seeded environment would almost certainly alter the distribution in the samples passing through the probe volumes at the prescribed test locations. An analysis of the implications of the wide range of particle sizes and the uncertainty in the distribution by size on the data is presented in Chapter IV.

E. CALIBRATION RIG

To increase confidence in the LDV system, a calibration rig was fabricated to allow comparison of LDV measurements with pitot-static measurements. An unregulated nozzle was attached to a high-pressure shop utility air hose.

The nozzle was mounted approximately on centerline at one end of a one-inch inside-diameter aluminum tube. The wand attached to the Rosco fog machine was mounted so that it would discharge smoke approximately normal to the centerline axis of the tube adjacent to the nozzle. The nozzle was designed to act as an ejector pump that would entrain smoke into the flow through the tube. Flow through the nozzle was controlled by turning a standard wheel-adjusted needle-valve.

The tube was approximately 4 ft 3 in long. A pitot-static probe was mounted with its tip on centerline approximately 3 in from the exit plane of the tube. The axes of the tube and the pitot-static probe were aligned to within $1/4$ degree using LDV traverse system measurements to survey the locations of scribed marks on the surface of the tube and the probe when the LDV probe volume was superimposed on the marks. Using a similar survey procedure, the tube and pitot-static probe were oriented parallel to the orientation of the velocity component measured by the one-component (x-component) probe. The x-component probe volume was positioned approximately $1/2$ inch directly upstream of the pitot port.

The pitot pressure connection was attached to one side of a U-tube water-filled manometer. The other side of the manometer was exposed to ambient pressure. The manometer scale was marked in millimeters. A sketch of the calibration rig is presented in Figure II.11.

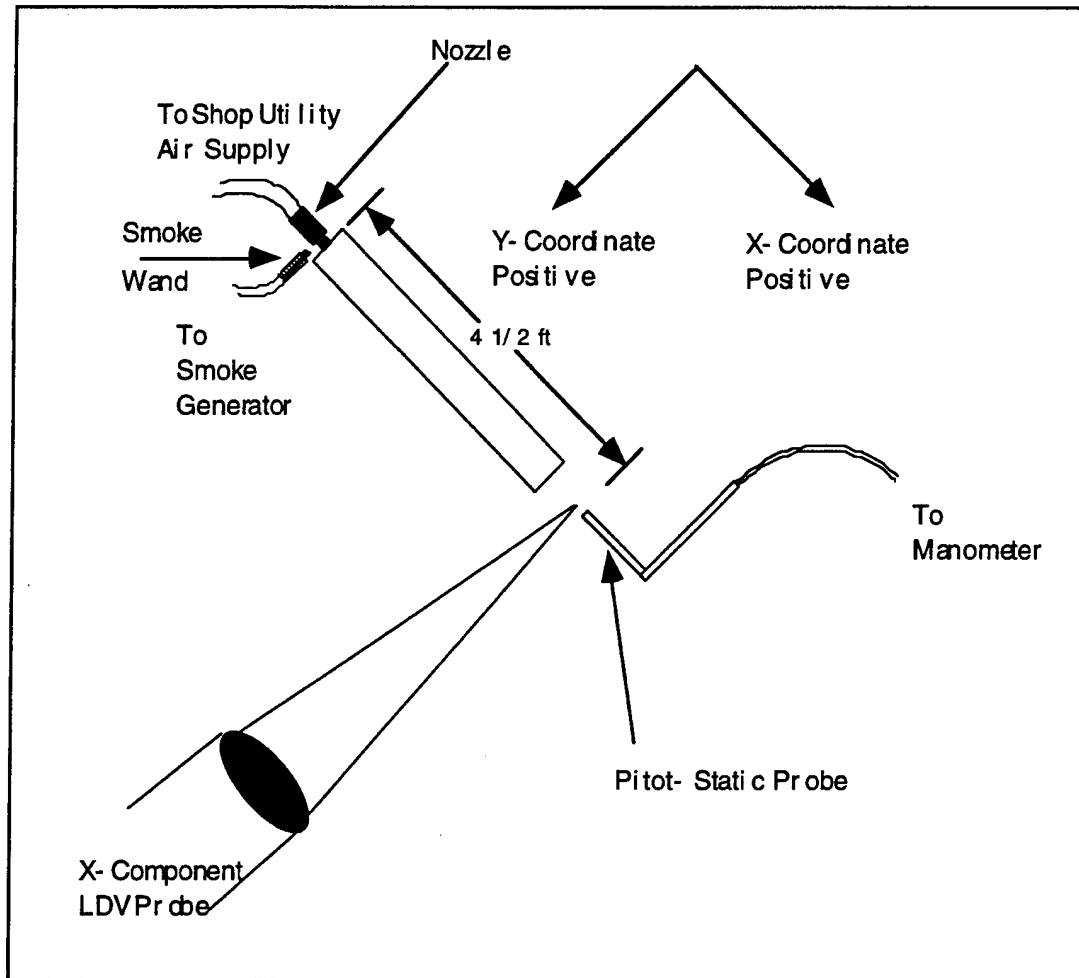


Figure II.11 Sketch of LDV vs Pitot-Static Calibration Rig

III. EXPERIMENTAL PROCEDURES

A. PROBE OPTICS

1. Mounting and Alignment

Initial alignment of the two-component probe mounted on the traverse mechanism I-beam was accomplished using a protractor scale on the I-beam base plate to which the optics probe mounting plate was attached. The centerline axis of the probe was oriented on a 45-degree angle with the I-beam. The base plate of the second one-component probe was secured to the I-beam at a distance calculated to produce the isosceles triangle geometry described in Chapter II. Coarse adjustments of the second probe alignment were accomplished by positioning the probe volume of the green beams from the two-component probe on a pinpoint on a white sheet of paper. The position of the second, one-component probe was then adjusted to bring its blue beam ("violet" for full 3-D systems) probe volume to the same pinpoint using vernier adjustment screws on mount. Final adjustments were accomplished by replacing the white paper with a microscope objective lens and bringing the beams into coincidence at the lens. Coincidence of the probe volumes was further verified by using the transmitting optics from one probe and the receiving optics of the second probe to collect sample data over a TSI six-jet atomizer emitting distilled water seed.

Additionally, in accordance with the procedures detailed in Reference 6, the coincidence of the probe volumes for the blue and green beams of the two-component probe was verified with the microscope objective, as was the coincidence of the one-component blue and two-component green beams. At minimum spot size, the blue and green patterns

overlapped by more than 95 and 90 percent in the case of the two-component beams and the two-component-to-one-component comparison, respectively.

Measurements of distances between points where the laser beams were projected onto the laboratory wall revealed the angle between the two probes was $89 \frac{3}{4}$ degrees with an uncertainty of $\pm \frac{1}{4}$ degree and that both probes were aligned within $\frac{1}{4}$ degree of the planned 45 degree angle with the I-beam as depicted in Figure III.6.

2. Half-angle Measurement

The same method used to determine the angle between the probes and the orientation of the probes relative to the I-beam was used to determine the actual half-angle between the two blue beams emitted from the one-component probe. The beams were projected onto a screen 35 feet from the probe volume and the distance between the beams measured. A one inch uncertainty in the measurements was assumed based upon a subjective judgment of the degree to which the metal tape measure used for the measurement bowed under its own weight. The resultant uncertainty in the half-angle measurement was ± 0.2 percent

B. TRAVERSE

The microscope objective was placed at various watermarks on the model and the ground plane and the LDV probe volume centered on the objective to survey the geometry of the test assembly. Pinpoints were used on the left strut in lieu of the microscope objective. The coordinates displayed by the traverse mechanism control panel defined the three-space coordinates of the survey points on the model, the struts, and the ground plane. The orientation of the traverse mechanism coordinate axes is presented in Figure II.6: x-positive is toward the model, y-positive is parallel to the I-beam and in the direction of the nose of the model, and z-positive is up.

The origin of the coordinate system was established by resetting all the traverse mechanism control panel displays to zero when the probe volume was coincident with the microscope objective lens as positioned on the model wingtip trailing edge watermark as depicted in Figure III.1.

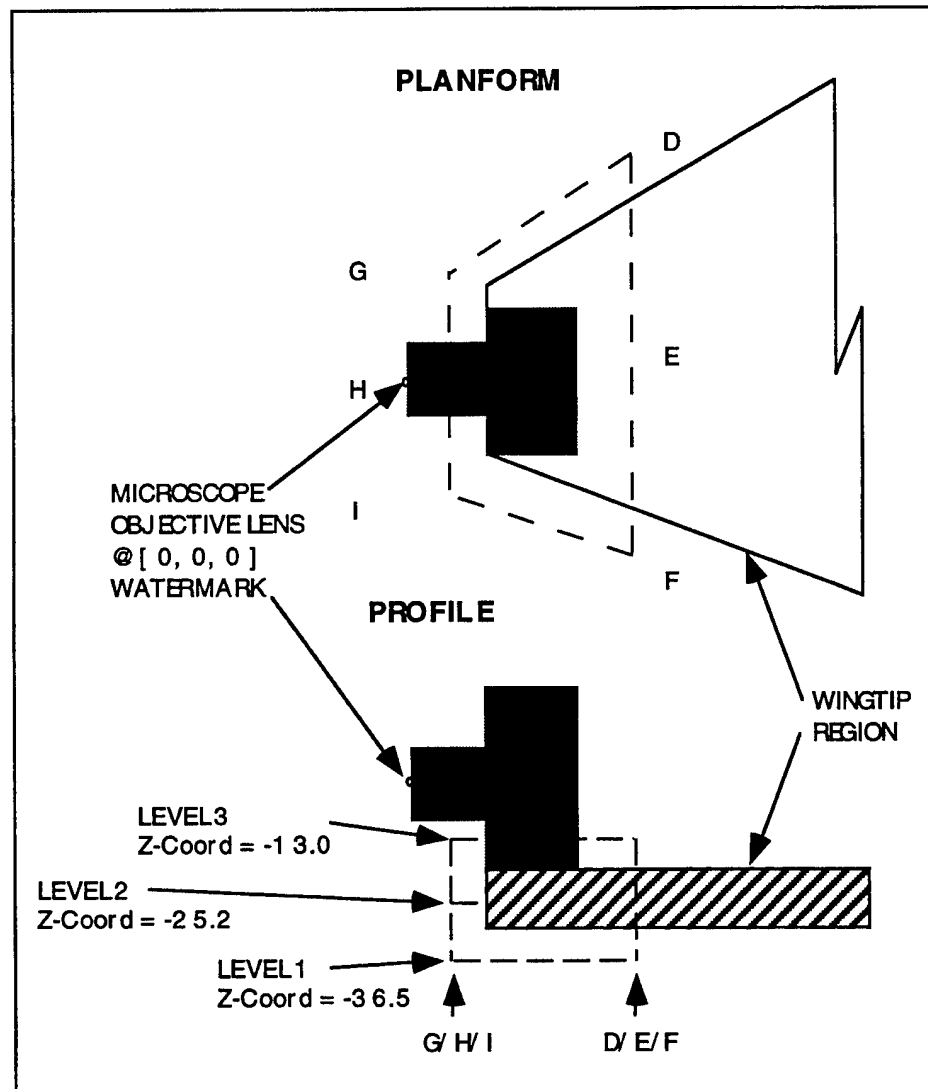


Figure III.1 Traverse Mechanism Coordinate System Origin

To ensure repeatability, the test apparatus was surveyed before and after each test. No attempt was made to quantify the mechanical freeplay and

hysteresis characteristics of the traverse mechanism, but slewing the traverse off of the origin and returning the probe volume to the microscope objective lens consistently returned the traverse to the coordinate origin ± 0.01 mm.

The coordinates of the test points in the vicinity of the left strut and the wingtip are presented in Table III.1. Additionally, the coordinates of the intersections of the upper and lower leading and trailing edges of the wing and canard with their respective tips are presented. The survey points on the left strut are not presented; however, the locations of test points A, B, and C are presented to correct scale with respect to the strut in Figure IV.6.

TABLE III.1 TEST POINT AND WING/ CANARD TIP COORDINATES

Coordinates:	X	Y	Z
Points adjacent strut:			
A	- 199.33	22.5	- 34.37
B	- 220.87	- 2.79	- 34.37
C	- 220.87	45.21	- 34.37
Points around wingtip: Z-Coordinates: Lower - 36.5			
			Mid-Plane - 25.2
			Upper - 13.0
D	50.0	42.00	
E	50.0	4.00	
F	50.0	- 34.00	
G	10.0	20.00	
H	10.0	- 1.00	
I	10.0	- 22.00	V
Wingtip/Canard Tips: Z-Coordinates: Lower - 30.0			
		Upper - 18.5	
Aft wing tip:	21.4	- 14.6	
Fwd wing tip:	21.4	17.5	
Aft canard tip:	111.8	177.2	
Fwd canard tip:	111.8	209.3	V

C. TEST MATRIX

1. Selection of Test Conditions

The test conditions selected for this investigation are presented in Table III.2. The conditions were those which produced the most significant difference in the location of the ground plane stagnation line during the tests Dooley conducted (Reference 3) with one exception. The scale height was

chosen because the corresponding full-scale height is near the point of maximum pilot workload during VTOL.

TABLE III.2 TEST CONDITIONS

<u>TEST PARAMETER</u>	<u>TEST CONDITION</u>
Thrust Ratio (Fwd/Aft)	0.67
Nozzle Pressure Ratio:	
Forward	1.624
Aft	1.323
Scale Height:	
Non-Dimensional (h/D_e)	4
Dimensional	6 inches
Standard Sea-Level Conditions	<u>Forward</u> / <u>Aft</u>
Total Pressure (P_t):	23.9 / 19.4 lb/in ²
SSL Mach Number:	0.863 / 0.642

2. Selection of Test Coordinates

The traverse system coordinates of the locations chosen for this investigation are presented in Table III.1 and depicted graphically to scale in Figures IV.2 through IV.6. In the absence of analytical tools, the points in the vicinity of the struts were chosen to be as close to the struts as beam geometries could accommodate to increase the probability that measurable differences would exist in component velocities between the struts installed and struts removed configuration. Similarly, the points near the wingtip were chosen inboard and slightly outboard of the tip such that the beam geometries would accommodate three component measurements at each point.

D. CALIBRATION

1. Pre-Calibration Surveys

Prior to taking velocity measurements prescribed in the test matrix, a number of flow visualization techniques were employed to assess the general character of the flow and the extent of seed entrainment in the regions of interest. A Helium-Neon laser sheet was used in conjunction with saturation seeding to qualitatively assess the extent of seed entrainment below the wing and the lower surface of the wing was tufted with vertically-oriented strands of yarn approximately 1/2-inch long to observe the general direction of the flow.

In a separate test, after the yarn tufts were removed, a 1/16-inch diameter steel rod was tufted with a single 1/2-inch strand of heavy thread and an L-shaped wand with a 3/4-x 1/16-inch discharge port was connected to the Rosco smoke generator. Both devices were used to "tell-tale" the direction of the flow and relative turbulence intensity at the points of interest. Sketches of the observed flow at each of the test matrix points revealed that to produce the resolved vectors in the sketch, all component velocities in the LDV coordinate system would have to be positive. Only the likely sign of the z-component at point E above and below the wing were indeterminate. Accordingly, zero frequency shift was chosen for the initial limited velocity survey.

A limited survey was conducted using the real-time histogram display to determine the approximate statistical distribution of velocity samples at points where small component velocities and significant unsteadiness were anticipated. Additionally, attempts were made to determine optimum saturation seeding density and laser power to maximize data rates for the entire set of test locations. In cases where the standard

deviation of a sample exceeded thirty percent of the velocity component, a frequency shift of 500 KHz was selected to "drive" the interference fringes opposite the flow at nominally 1.8 and 1.7 meters/second for the green and blue beams, respectively. This shift was sufficient to preclude "wrap around" of velocities beyond three standard deviations in all cases sampled and also for all cases later collected in the actual test data sets.

Processor filter settings were selected automatically by the FIND software during the pre-calibration surveys. A filter band was selected based upon the number of samples that are captured in a given filter band during a sampling routine in the first few seconds of the data acquisition cycle. In many cases, when ten or fewer points were the maximum number of points collected in any one band during the sampling cycle, the software was inconsistent in selecting the filter band. Two adjacent or overlapping bands would often collect nearly the same number of points, with one band having more in a given acquisition cycle and the other having more in the next. For example, eight successive attempts to collect data at one test condition resulted in four automatic selections of the 100 KHz to 1 MHz filter band and four selections of the 300 KHz to 3 MHz range. The mean velocities calculated for the cases of the lower filter range selection were in the 2.6 meter/second range and the 5.8 meter/second range when the higher filter range was selected. When the 100 KHz to 3 MHz filter range was selected manually, six successive data sets produced six nearly equal mean values. Accordingly, since 3 MHz was the upper bound on any filter setting found during the pre-calibration survey and above the doppler frequency including a 500 KHz shift for any of the expected velocities, a manual selection of 1 KHz to 3 MHz was chosen for the actual tests.

2. Calibration Test

Because manuals were not available for the Model 9186A-4 frequency shifter controller, tests were conducted using the TSI six-jet atomizer to ensure the 500 KHz frequency shift planned for the calibration and subsequent tests was being applied in the proper sense --- to drive the fringes opposite the flow. With all six jets selected and the dilution air valve closed, the probe volume of the green beams on the two-component probe were placed over the nozzle on the atomizer. The frequency shift was set to zero and a real-time histogram was initiated in the frequency display mode. The dilution air valve was opened to increase flow velocity in increments sufficient to observe changes in the peak of the histogram. The peak frequency increased monotonically with the increasing velocity.

The procedure was repeated with upshift and downshift values of 500 KHz and 1.0 MHz selected on the frequency shift controller. The flow was physically in the direction from the shifted to the unshifted beam as they originated from the face of the LDV probe. Upshifting the beam resulted in an increase in the initial frequency at minimum flow velocity and monotonically increasing behavior with the increasing velocity. Downshifting the beam resulted in a lower initial frequency and the frequency actually decreased with the initial increase in velocity before becoming monotonically increasing at higher velocities. An upshift of 500 KHz was selected for both the calibration and the actual tests to drive the fringes opposite the LDV system coordinate axes.

Calibration tests comparing LDV to pitot-static measurements were conducted at velocities ranging from 66 to 128 feet/second. The lower limit was determined by the minimum control valve setting at which a steady flow velocity could be achieved as defined by steady levels on the water

manometer. The upper limit was determined by opening the control valve fully.

E. DATA COLLECTION

1. Control and Monitoring of Test Conditions

The reservoir pressure for the air supply was brought to the maximum regulated pressure of 147 lbs/ in² and maintained at that pressure by a single compressor running continuously during each tests. The FAA control tower at Monterey airport was consulted every two hours to determine the ambient barometric pressure. The nozzle pressure ratios were adjusted accordingly to achieve the values listed in Table III.2.

2. Data Acquisition Software Configuration

Prior to acquiring each data set, the settings on the "Optics Configuration" and "Processor SetUp" displays of the FIND software were verified. Generally, only the wavelength and the software-computed fringe spacing were the only items that were required to be changed. All test data were collected with the frequency shift selection of 500 KHz upshift and a manual filter setting of 1 KHz to 3 MHz.

3. Order of Test Data Sets

For test points A, B, and C in the vicinity of the strut, a single sample of data planned for each component at each point was first collected without the struts installed. The struts were installed and the left strut surveyed into proper position with the nozzles operating. Data were then collected in the following order: one data set for the planned components at points C and A; two data sets at point B; and the remaining struts-on configuration data set at points A and C. The struts were then removed and the final data sets for each point and applicable components were collected. The transmitting and receiving optics were switched between the x- and y-component optics on the

one- and two-component probes as required. Each time the optics were switched the transmitting optics had to be realigned per the procedures detailed in Reference 7. The procedure took approximately ten minutes.

Data sets at points in the vicinity of the wing were collected on three separate days during test periods of approximately nine hours each. The data for a single component was collected on each of the days. The time between repeated data sets for a given strut configuration at a point varied from approximately one minute to an hour and a half.

4. Seeding

A qualitative assessment of the optimum saturation seeding density to achieve acceptable data rates was made during the pre-calibration tests. In the optimum seeding condition the lab looked like a smoke-filled saloon in an old western movie. Because of natural ventilation in the space, short bursts of smoke had to be discharged approximately every ten minutes to maintain the proper concentration. Real-time monitoring of the density of the doppler bursts displayed on the oscilloscope also provided a good qualitative indication of the density of seeding passing through the probe volume.

F. POST-TEST DATA ANALYSIS

Data were processed post-test using the FIND software to determine the mean component velocities and standard deviations for each data set. The results are tabulated in Appendix B. One advantage of using the FIND software for post-processing was a limited capability to apply Chauvenet's criterion to the data sets. Although Reference 11 indicates that for 1000 data points, 3.48 standard deviations is the appropriate rejection criteria, the software only allows selection of integer multiples. Three standard deviations was the value chosen for the analysis.

IV. RESULTS AND DISCUSSION

The pragmatic decision to saturate seed the room surrounding the test rig with smoke and the unavailability of any meaningful information about the character of the unsteady flow in the vicinity of the model were the primary issues of concern in assessing the utility of the LDV measurements. The central question posed a priori was whether a statistically consistent mean velocity measurement with struts installed and with struts removed could be interpreted as verification that the struts had not influenced the flow field. The possibility that the inertia of the larger seed particles could mask significant changes in the flow field could not be ruled out.

A. EXPERIMENTAL ACCURACY

The objective of this investigation was not to determine absolutely the component mean velocities at the selected locations; however, an uncertainty analysis was performed for the x-component LDV probe vs the pitot-static system calibration data. The purpose of the analysis was to ensure that LDV measurements of entrained particle velocities varied predictably with the mean flow velocity "truth data" obtained over a range of velocities that could be measured accurately with the pitot-static probe and water manometer. Although the y- and z-component measurements were taken with the optics of a second, two-component probe, otherwise the measurements used the same LDV system components and software configuration as for the x-component measurements. Calibrations were not accomplished for those components, but precisely the same terms considered in the measurement uncertainty analysis of the x-component velocity apply to the analysis of the other two components.

The uncertainty analysis was performed in accordance with the methods outlined in Reference 11, equation (3-2), pp 42. The LDV velocity calculation uncertainty was predicated entirely upon uncertainty in the half-angle measurement. Based upon observations of real-time velocity calculations with the probe volume positioned on a solid reflecting surface and of real-time histograms during calibration, errors in wavelength and time measurements appeared to be random and the distribution of the associated velocity measurement errors was assumed to be gaussian. Accordingly, uncertainties in wavelength and time measurements were accounted for in a statistical confidence interval analysis. Confidence intervals for the LDV samples were calculated in accordance with Reference 12. Measurement uncertainties are tabulated and sample calculations presented in Appendix A. The calibration data are presented in Table IV.1 and plotted in Figure IV.1. In addition to the mean velocities, the upper and lower uncertainty bounds for the pitot-static data, and the uncertainty in the half-angle measurement combined with the 95 percent confidence intervals for each LDV data set are also depicted in Figure IV.1.

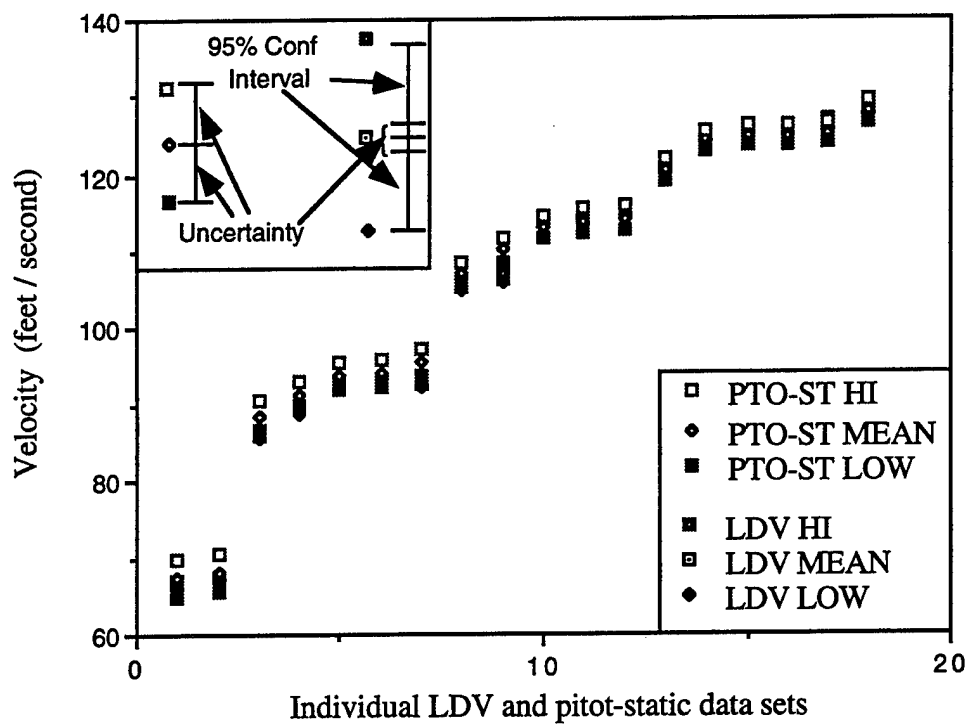


Figure IV.1 LDV vs Pitot-Static Calibration Data Plot

LDV Data:				Pitot-Static Data:							
x-comp	beam;	horizontal)	velocity in ft/sec	water manometer				velocity in ft/sec			
MEAN	STD DEV	POINTS	95% CONF INT	DELTA h	VELOCITY	UNCERTAINTY	LOW	HIGH	LOW	HIGH	
121.14	4.9475	2038	0.2148	3.39	120.52	1.4014	119.12	121.93			
124.70	4.9836	2033	0.2166	3.60	124.32	1.3587	122.96	125.68			
126.42	4.9114	2036	0.2133	3.64	125.00	1.3513	123.64	126.35			
125.49	4.8884	2032	0.2126	3.64	125.00	1.3513	123.64	126.35			
105.59	4.4062	2035	0.1914	2.68	107.17	1.5760	105.60	108.75			
106.55	4.3668	2036	0.1897	2.83	110.28	1.5316	108.75	111.81			
114.19	4.5899	2040	0.1992	3.03	114.04	1.4811	112.56	115.52			
115.01	4.9803	2036	0.2163	3.05	114.41	1.4763	112.94	115.89			
114.33	4.6949	2031	0.2042	2.99	113.30	1.4908	111.81	114.79			
86.07	4.4488	2044	0.1929	1.83	088.62	1.9059	086.72	090.53			
89.43	4.6752	2042	0.2028	1.95	091.44	1.8472	089.59	093.29			
92.51	4.8524	2044	0.2104	2.05	093.72	1.8023	091.92	095.52			
92.82	4.9967	2042	0.2167	2.07	094.17	1.7937	092.37	095.96			
92.78	4.9672	2033	0.2159	2.13	095.50	1.7686	093.74	097.27			
67.20	3.0118	2035	0.1309	1.08	068.15	2.4783	065.68	070.63			
66.86	2.9495	2028	0.1284	1.06	067.53	2.5012	065.03	070.03			
125.01	5.2526	2032	0.2284	3.66	125.33	1.3477	123.99	126.68			
128.13	5.3379	2032	0.2321	3.82	128.00	1.3196	126.68	129.32			

Table 4.1 LDV vs pitot-static calibration data

The data show good agreement between the two sets, within the calculated uncertainties, over the entire range of calibration points. A consistently small, but discernible bias of the mean LDV velocities toward the lower end of the pitot-static data uncertainty bound is predictable considering that the seed particles used for this calibration varied in diameter from 0.25 to 50 microns. It is likely that the larger particles failed to accelerate from rest to the true mean flow velocity in a distance of 4 1/2 feet. Reference 13 notes that typically, particles less than 1 to 2 microns are required to ensure accurate LDV measurements in low- to moderate-speed airflows. Physical limitations of the time response of seed particles to changes in a flow cause the uncertainty in determining velocities in any actual flow field always to be greater than the uncertainty in the measurement of seed particle velocities. For the relatively steady flow and moderate mean accelerations produced by this calibration rig, however, the agreement of the data sets at even the highest velocity point indicates that LDV measurements of particle velocities in the entrained flow were clearly representative of the true mean flow field velocity.

A simple calculation of the minimum linear acceleration required to achieve the maximum calibration point velocity of 128 feet/second in 4 1/2 feet indicates that LDV measurements with the seeding used for this evaluation should be reliable in flow fields characterized by accelerations of at least 1792 feet/second². Using the relationship (radius of curvature) = (velocity)² / (normal acceleration), and assuming no tangential acceleration with an acceleration normal to the flow of 1792 feet/second², the LDV-measured velocities would accurately represent the true entrained flow velocity where the radii of eddies tangent to the flow are greater than 0.082

and 8.2 inches, respectively, for mean flow velocities of 3.5 and 35 feet/second. 3.5 and 35 feet/second are near the minimum and maximum total velocities measured during this investigation. Although no information was available about the character of eddies in the unsteady flow, it is very likely that a significant number of eddies less than 8.2 inches in radius were generated in the fountain flow with the model only six inches above the ground plane.

B. REPEATABILITY

Repeatability of the LDV-measured mean component velocities for a given set of test conditions was an important consideration in planning these tests. Consistent mean velocity measurements at a given set of test conditions without the struts installed was required to ensure that any observed changes in the mean velocity with struts installed was not merely the result of measurement uncertainties. Unfortunately, there were several practical impediments to achieving a statistically stable value for mean velocity.

First, because there was no practical method to ensure a uniform spatial distribution of entrained seed particles, the LDV-measured data sets represent conditionally sampled data. In contrast with continuous, albeit intrusive, measurements from a hot-wire system, a velocity measurement was recorded only when an entrained particle transited the requisite eight fringes in the probe volume. Second, as addressed above, there was uncertainty regarding how well the larger particles followed a strongly accelerated flow. Third, there was no quantifiable information available a priori about the character of the fountain-induced coherent vortex structure that appeared from the wide histograms observed during initial investigation to produce large variations in the measured velocity. Finally, a sample size of 1024 points was determined to be the largest sample size practical to achieve a minimum

acceptable data rate over the entire set of test locations. The combination of these limitations made it very unlikely that the means of the time-dependent turbulence and the time-dependent unsteady flow components of velocity would be zero for any data set. Accordingly, the LDV-measured total particle velocities, comprising a time-invariant mean component and the time-dependent turbulence and unsteady flow components, would be unlikely to be distributed normally about the true mean.

1. Statistical Confidence Intervals

The statistical confidence intervals calculated in accordance with Appendix A assumed a normal distribution of measurement errors. Given two independent data sets such that the mean velocity of one set fell within the ninety-five percent confidence interval about the mean of the second set, and vice-versa, it is not mathematically rigorous to conclude that the true mean flow field velocity remained unchanged during the period in which the data were collected. It does, however, increase confidence in the repeatability of the measurement. Similarly, if the mean velocity of each set of data without struts fell within the ninety-five percent confidence interval of the other set(s), but outside of the ninety-five percent confidence intervals of the data sets with struts installed, it is very likely that the observed mean velocity had changed.

2. Short-term Velocity Variations

Because of the decision to collect nominally 1024 points data points for each sample velocity measurement and the physical and processing software constraints of the test setup, the time required to collect a data set varied from eight to nearly three hundred seconds. Clearly, as a stand-alone piece of information, the mean velocity calculated from data collected at the slower data rates provided little meaningful information relevant to the

primary question of the investigation: were there significant short-term (3-5 seconds) variations in the flow field? In the absence of time-tagging of the sample points and because of the conditional sampling issues previously addressed, observation of the real-time histogram display of velocity provided the only useful insight into the transient behavior of the flow.

In general, the real-time histograms formed symmetrically with no discernible "wandering" peaks, indicating an essentially steady mean velocity for each data set. In most cases, the mean velocities of two or more consecutive data sets collected in the real-time histogram mode varied less than five percent. Only in cases where consecutive real-time histograms of fewer than twenty points were examined did variations in the mean velocity exceed ten percent. In such cases, the data rates were very slow (less than 10 Hz) indicating a flow that was extremely sparsely populated with entrained seed particles. Accordingly, it is unlikely that such samples accurately represented the attributes of the true flow field.

C. VARIATION OF COMPONENT MEAN VELOCITIES

Reduced data from this investigation are presented graphically in Figures IV.2 through IV.6 and in tabular and graphic form in Appendix B. Figures IV.2 through IV.4 are planform views of the left wingtip region at the traverse system z-coordinates corresponding to the upper, mid, and lower planes depicted in Figure III.1. The x-y plane projections of the mean velocity vectors are depicted with their origins at their corresponding test matrix coordinates. Length and velocity scales are also provided, along with graphics showing the orientation of the traverse system and LDV velocity component coordinate axes. Figure IV.5 presents three profile views of the wingtip region along the traverse system y-coordinate axis. The projections of the mean velocity vectors into the traverse system x-z plane are depicted with

their origins at their corresponding test matrix coordinates. As with the planform views, length and velocity scales are also provided.

Figure IV.6 depicts test point geometry in the vicinity of the strut closest to the left wingtip. Velocity measurements in the vicinity of the strut location were made at a single traverse system z-coordinate of -34.37 mm. Mean velocity data with and without struts installed are presented graphically in boxes adjacent the test points. Length and velocity scales are provided, but the scales are not the same as for Figures IV.2 through IV.5. The box adjacent point A contains the projection of the mean velocity vector into the x-y plane. The box adjacent point B shows the projection of the mean velocity vector into the LDV velocity x-z coordinate plane. The x-component velocity could not be measured at point B with the strut installed because the strut obscured the beams from the x-component probe. The box adjacent point C shows the x-component of the mean velocity vector oriented parallel to the LDV x-coordinate axis with separate origins for the conditions with and without struts installed. The y and z velocity components could not be measured at point C with the strut installed because the strut obscured the beams from the two-component probe. A dashed line is drawn through the separate origins (parallel to the LDV velocity y-coordinate axis). A second dashed line is drawn parallel to that line and contacting the head of one vector to assist in comparing the lengths of the vectors.

The tables of Appendix B present the mean LDV component velocity, the standard deviation, the 95% confidence interval, and the mean plus and minus the 95% confidence interval for each data set at each test point defined in traverse system coordinates. The units for velocity are meters per second.

The graphics of Appendix B present the tabulated data by grouping data sets for like strut configurations and plotting the mean and the mean plus and minus the 95% confidence interval.

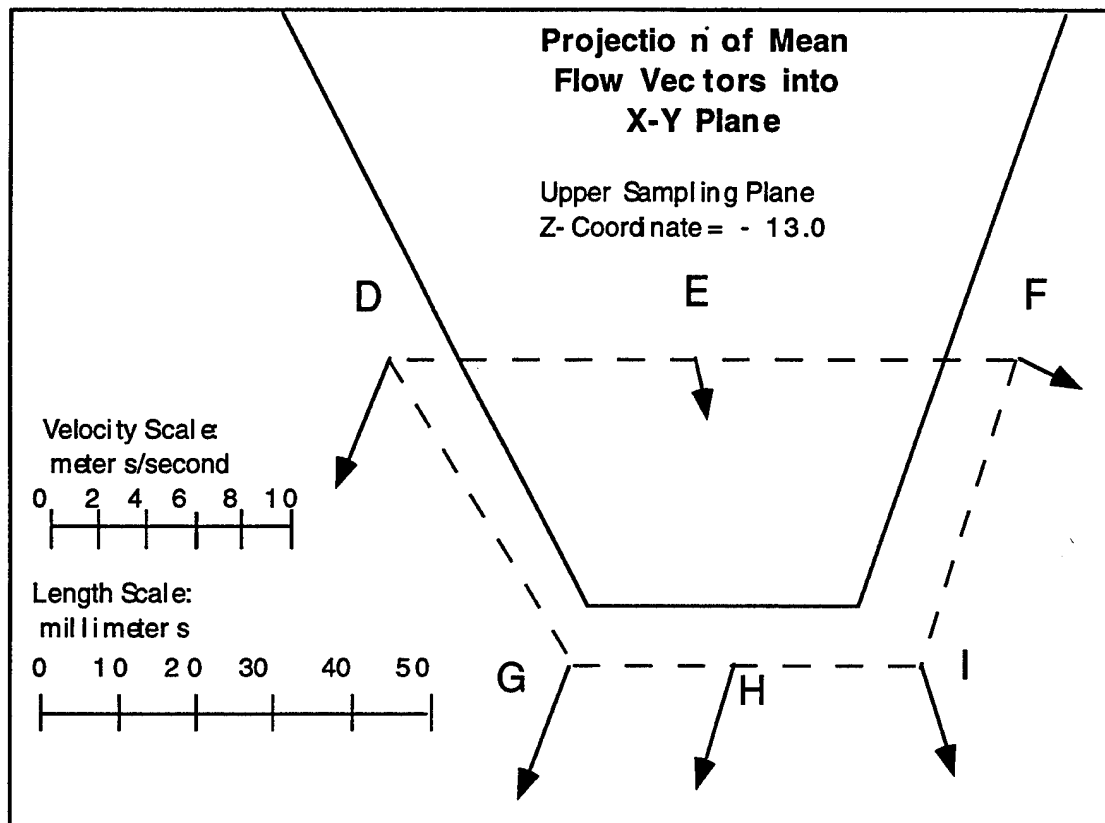


Figure IV.2 Planform View of Flow in Upper Plane

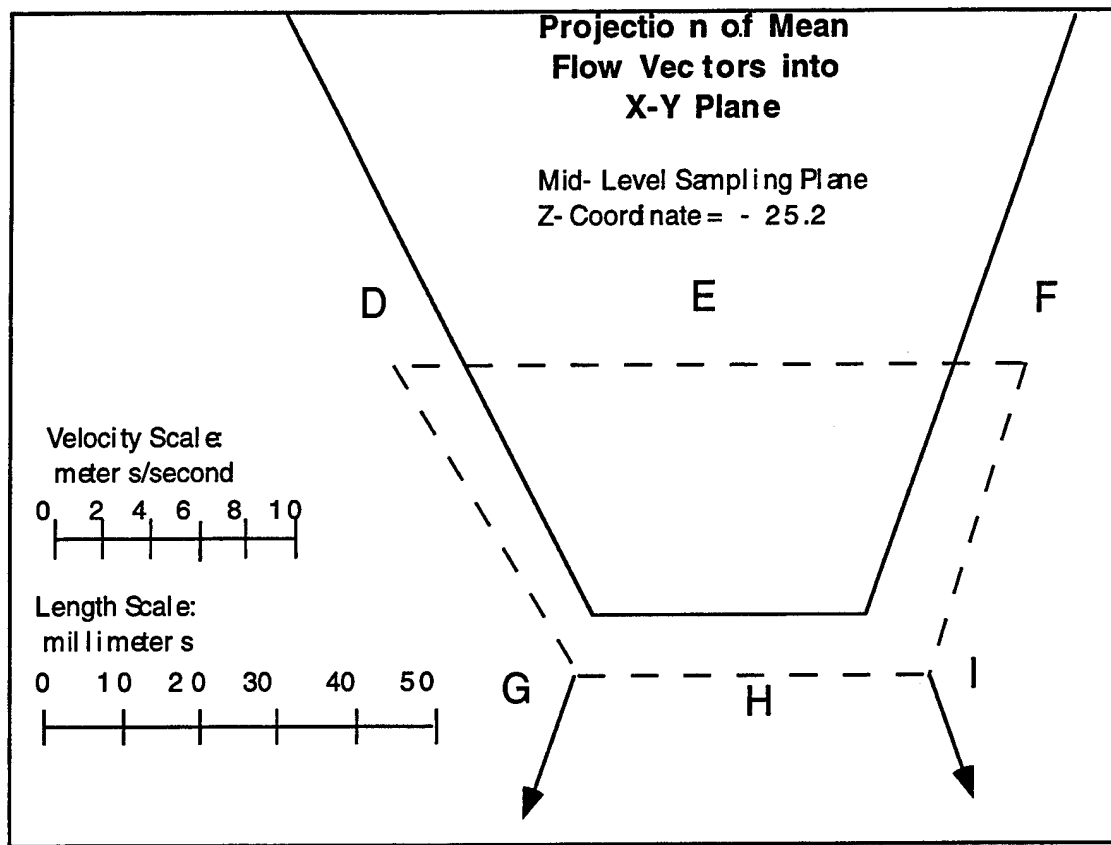


Figure IV.3 Planform View of Flow in Mid Plane

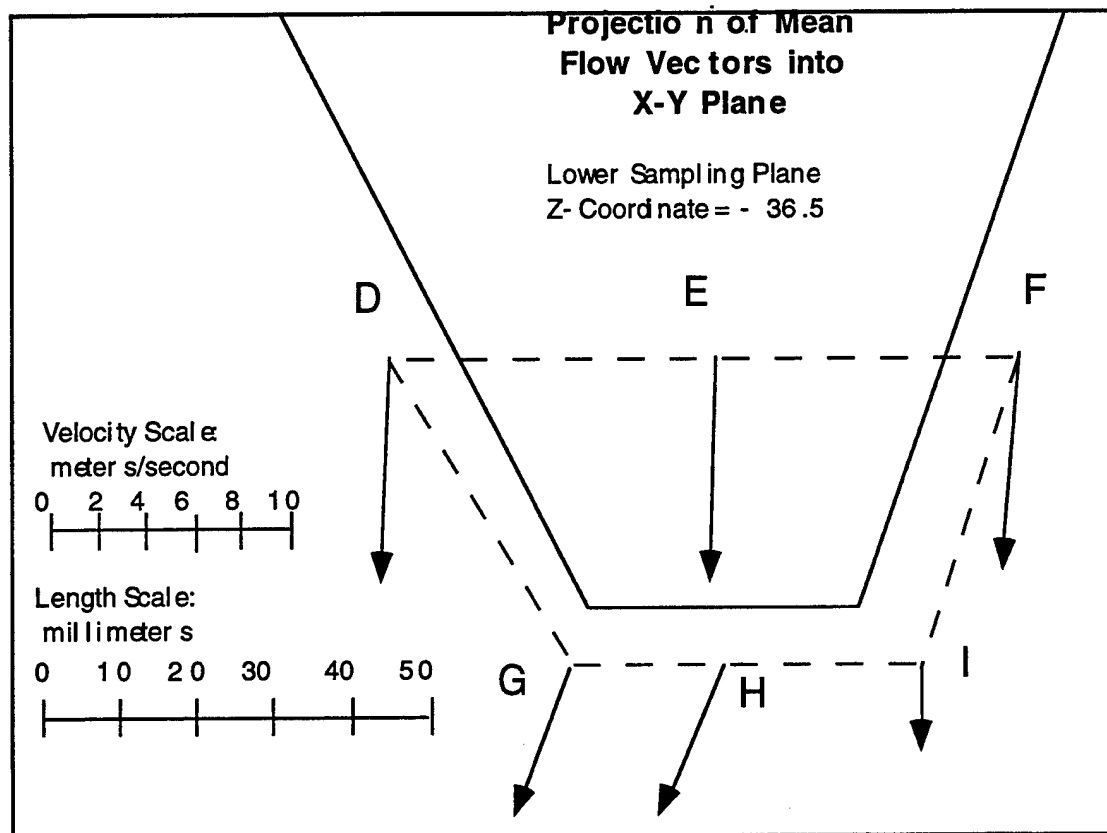


Figure IV.4 Planform View of Flow in Lower Plane

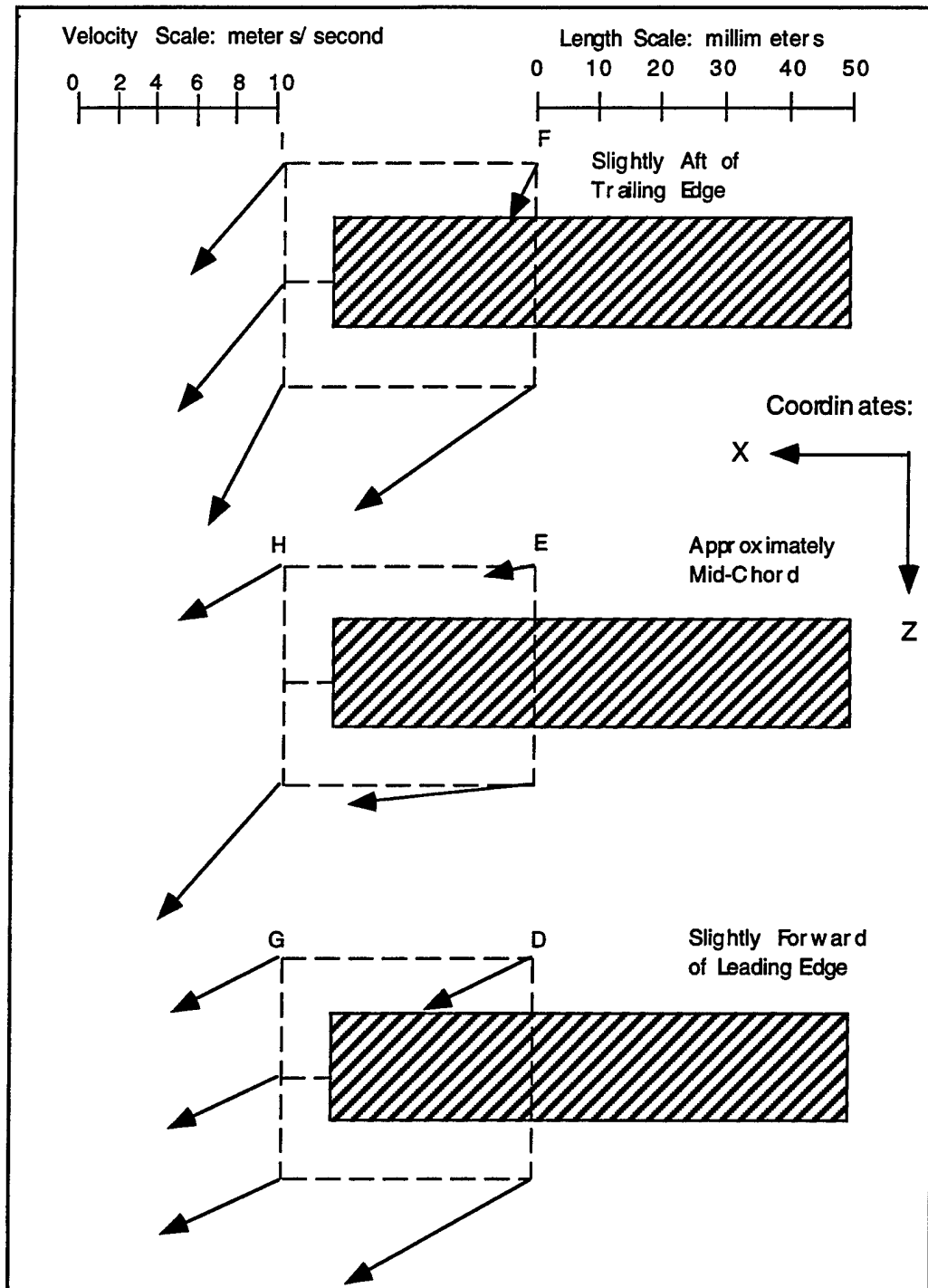


Figure IV.5 Profile View (X-Z Plane) of Flow Velocity Vectors at Selected Test Points

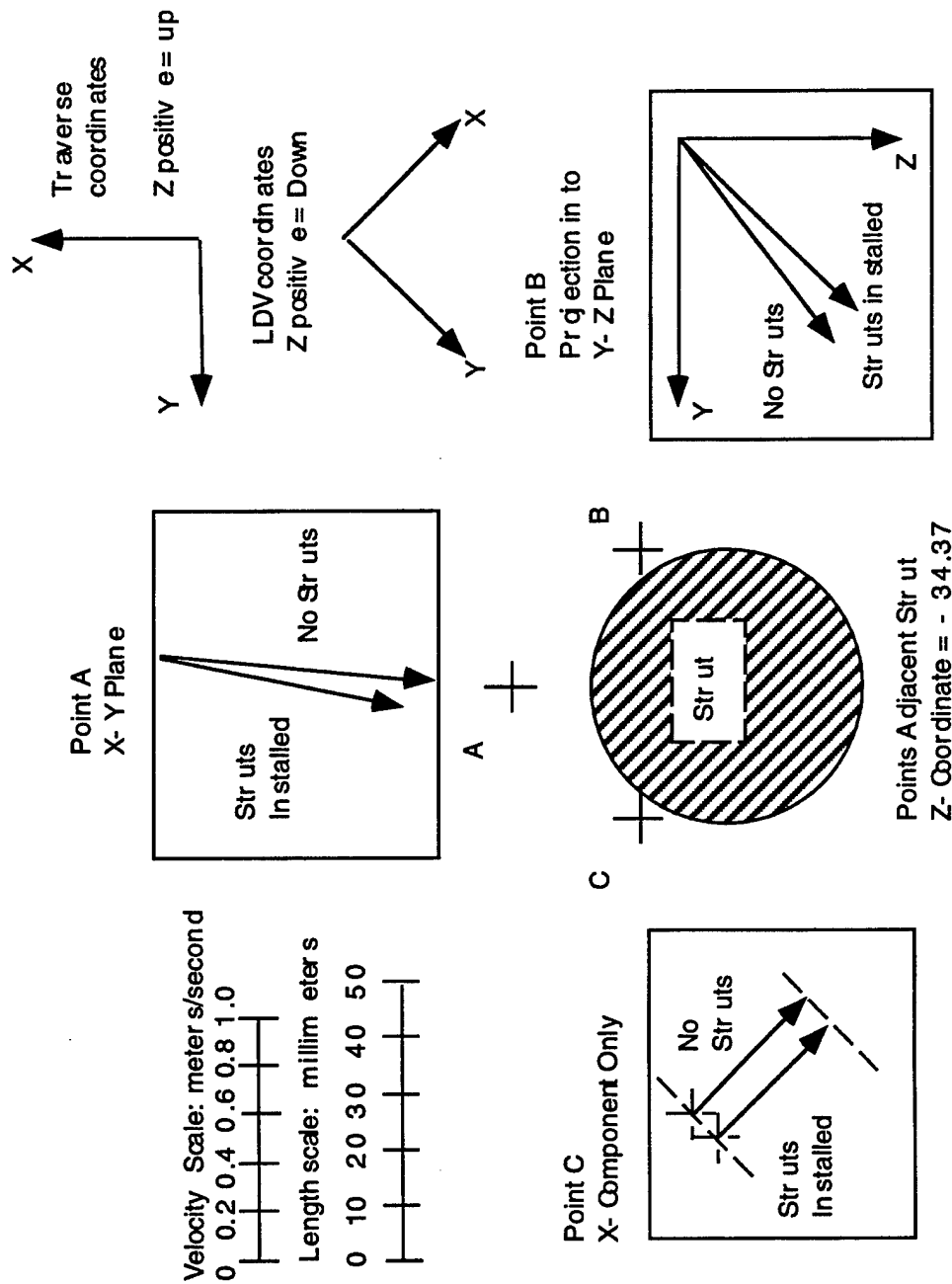


Figure IV.6 Flow in vicinity of Strut

1. Qualitative analysis

The mean flow velocities at test points A and B clearly changed in magnitude and direction between the struts-installed and struts-removed configurations. The magnitude of the velocity at point A decreased significantly, but the direction changed only slightly indicating point A was located near the stagnation streamline (strut-installed). Flow visualization using a smoke wand and a tufted wand also indicated this to be the case. A review of ground plane oil streak flow visualization photographs in Reference 3 for the same test configuration and the same test conditions showed results similar to the wand tests.

The magnitude of the only velocity component measured at point C (the x-component) remained unchanged for both strut configurations. However, if the magnitude of the flow velocity were to increase with the strut installed, as is the case in a simple velocity potential solution for a doublet and uniform flow combination, the resultant increase in the y-component of velocity would also produce a change in the direction of the vector in the x-y plane that was consistent with the doublet and uniform flow solution.

In the vicinity of the wing the general orientation of the velocity vectors in the x-y plane (horizontal) was consistent with intuition. At the level of the plane slightly above the wing, the entrained flow cascades off the model as would water if poured from a pitcher onto the center of the left wing panel. At the plane beneath the wing, the cascading flow from above is accelerated laterally relative to the model centerline by the confluence of flows from the jet-induced fountain bounded above and below by the model planform and the ground plane, respectively. Flow at the mid-plane is consistent with the transition between the two flows previously described.

Profile (x-z plane) views of the velocity vectors were also consistent with intuition --- a downward trend of the cascading entrained flow accelerated beneath the wing as by an ejector nozzle. In close proximity to the wing inboard of the tip and near mid-chord, the flow is restricted by the wing surface and is more nearly horizontal. Smoke- and tufted-wand surveys confirmed the flow was generally oriented as depicted in Figures IV.2 through IV.6.

Examining the graphics of Appendix B, it is clear that the mean component velocity for a given test data set and strut configuration was not consistently statistically repeatable in the vicinity of the wingtip. As previously stated, this result was entirely predictable in an unsteady flow field. Nonetheless, when an average mean velocity is calculated using both data sets with struts-removed and again with struts-installed, variations in the average means for the two configurations are generally indiscernible. Accordingly, the vectors depicted in Figures IV.2 through IV.5 are derived from all the component mean velocities measured at each of the corresponding test point coordinates.

The graphics of Appendix B also reveal that in the vicinity of the strut, measurements of the mean component velocities were both statistically stable and exhibited significant statistical differences between strut configurations. This results merely confirms that the LDV system can detect the obvious result --- the flow changes when a strut is introduced immediately adjacent to the point of interest.

2. Quantitative Analysis

The standard deviations of most velocity component data sets in the vicinity of the wingtip were typically 15 to 20 percent of the mean indicating significant turbulence and unsteadiness in the flow. In the vicinity of the

strut, where mean velocities were low and smoke wand surveys indicated even greater unsteadiness than near the wing, the standard deviations varied between approximately 55 and 75 percent of the mean.

Variations in component mean velocities between data sets for a given strut configuration at a given test point were generally less than six percent, although in two cases the variations were approximately 10.7 and 14.7 percent. However, when average mean velocities were calculated using both data sets as described above, variations in the average means were 2.3 percent or less.

V. CONCLUSIONS

A. CONFIDENCE IN MEASUREMENTS

Considerable effort was made to ensure the reasonableness of the LDV measurements. Calibration of the LDV vs a pitot-static system using the same seeding as in the actual tests established confidence in the velocity measurements and suitability of the seed particle response within quantifiable acceleration limits. Smoke- and tufted-wand surveys of the test regions supported the LDV test results. The test results are therefore considered reasonable and representative of the true mean flow field of the entrained flow.

B. MEAN VELOCITIES

Although the mean velocity components measured in the vicinity of the wingtip were not, in many cases, statistically stable (repeatable within the chosen confidence interval), the variations in mean values were generally relatively small. Over the entire wingtip region, variations in the average of the mean component velocities for each strut configuration were very small (less than 2 1/2 percent). The effect of the struts on the mean flow field in the vicinity of the wingtip is therefore essentially negligible.

C. SHORT-TERM FLOW FIELD VARIATIONS

Mean velocities were not obtained from short-duration samples (2-5 seconds) because insufficient data rates produced insufficient sample sizes. Accordingly, a meaningful quantitative evaluation of transient variations in flow velocities that would directly affect the forces and moments on the wingtip was not accomplished. Based upon observation of real-time

histograms as they formed during the tests, however, there was no discernible difference between the struts-removed and struts-installed configurations in the manner in which the histograms took shape.

D. SUMMARY

Within the scope of this investigation, the influence of support struts on the flow field in the vicinity of the model wingtip is indiscernible. Since the wingtip is the most likely region for the flow field to be affected by the struts and the region in which flow field changes can produce the greatest variations in rolling moment, it is unlikely that the struts would contaminate measurements of short-term variations or long-term averages of the forces and moments on the Lockheed configuration LSPM in the NASA Ames OARF test rig.

VI. RECOMMENDATIONS

A. SEED PARTICLE CHARACTERISTICS

Saturation seeding of the area surrounding the test rig was chosen for this test primarily to improve the uniformity of particle distribution in the entrained flow. This seeding method is promising for future use if evaluations are required with higher fidelity models and test rigs, but is currently of limited utility. The upper limit of velocities tested in the calibration rig, and indirectly the upper limit of the acceleration for which future test results could be assumed accurate, was established by the physical limitations of the rig. Further testing should be conducted to determine the true frequency response limits ("3-dB Frequency" in Reference 13) of the seed produced by the Rosco smoke generator.

B. SURFACE PRESSURE MEASUREMENTS

The McDonnell Douglas LSPM is a larger model and its wingtips will be physically closer to the struts in the OARF than the Lockheed model. Additionally, OARF tests will include force and moment measurements in other than fuselage- and wings-level attitudes. To ensure the present configuration of struts does not significantly influence the flow field around the model and contaminate any force and moment measurements in the planned LSPM test matrices, further risk reduction tests are recommended. The tests should use a reasonably high fidelity model including cavities and landing gear and a higher fidelity model of the OARF support structure including taper of the support struts with increasing height. The model should be instrumented for direct measurements of surface pressures

through ports in the model skin. The pressure measurement instrumentation should allow essentially simultaneous and continuous measurements over the instrumentation array. Emphasis should be placed on measurements near both wingtips, the nose and tail areas, and the region between lift nozzles. The test matrix should include evaluation of a range of pitch and roll attitudes greater than that planned for the OARF tests.

APPENDIX A. SAMPLE CALCULATIONS

A. UNCERTAINTY ANALYSIS

LDV velocity uncertainty:

$$df = \lambda / (2 \sin \kappa)$$

$$V = 8 df / t = 4\lambda / t \sin \kappa$$

$$W_V = [(W_\lambda)^2 (\partial V / \partial \lambda)^2 + (W_\kappa)^2 (\partial V / \partial \kappa)^2 + (W_t)^2 (\partial V / \partial t)^2]^{1/2}$$

$$\partial V / \partial \lambda = 4 / (t \sin \kappa)$$

$$\partial V / \partial \kappa = -4\lambda \cot(\kappa) \csc(\kappa) / t$$

$$\partial V / \partial t = -4\lambda / t^2 \sin \kappa$$

for t and λ errors assumed random and associated errors in V are gaussian:

$$W_V = [(W_\kappa)^2 (\partial V / \partial \kappa)^2]^{1/2} = (W_\kappa) \partial V / \partial \kappa$$

$$= -4 W_\kappa \lambda \cot(\kappa) \csc(\kappa) / t$$

Pitot-static velocity uncertainty:

$$V \text{ (ft/sec)} = 65.5 (\Delta h)^{1/2} \quad (h \text{ in inches})$$

$$\partial V / \partial h = 32.8 (\Delta h)^{-1/2}$$

TABLE A.1 MEASUREMENT UNCERTAINTIES

Parameter	Description	Uncertainty	Method of Determination
p_t	Stagnation pressure	0.5 mm	Water manometer/judgment
p_a	Ambient pressure	0.03 in	Mercury barometer@airport
λ	Wavelength	0.1 %	TSI Corp.
κ	Beam Half Angle	0.2%	Tape meas of beam extension.
t	Time for 8 fringe crossings	2 nsec	TSI Corp.
df	Fringe Spacing	0.3 %	Derived
V	LDV Velocity	0.33 %	Derived @ 10 m/sec
W_x	Uncertainty in "x" parameter		

B. CONFIDENCE INTERVALS

for t and λ errors assumed random and associated errors in V are gaussian:

$$95 \% \text{ Confidence Interval} = 1.96 (\text{Standard Deviation}) / (\text{No. of Points})^{1/2}$$

APPENDIX B. REDUCED TEST DATA

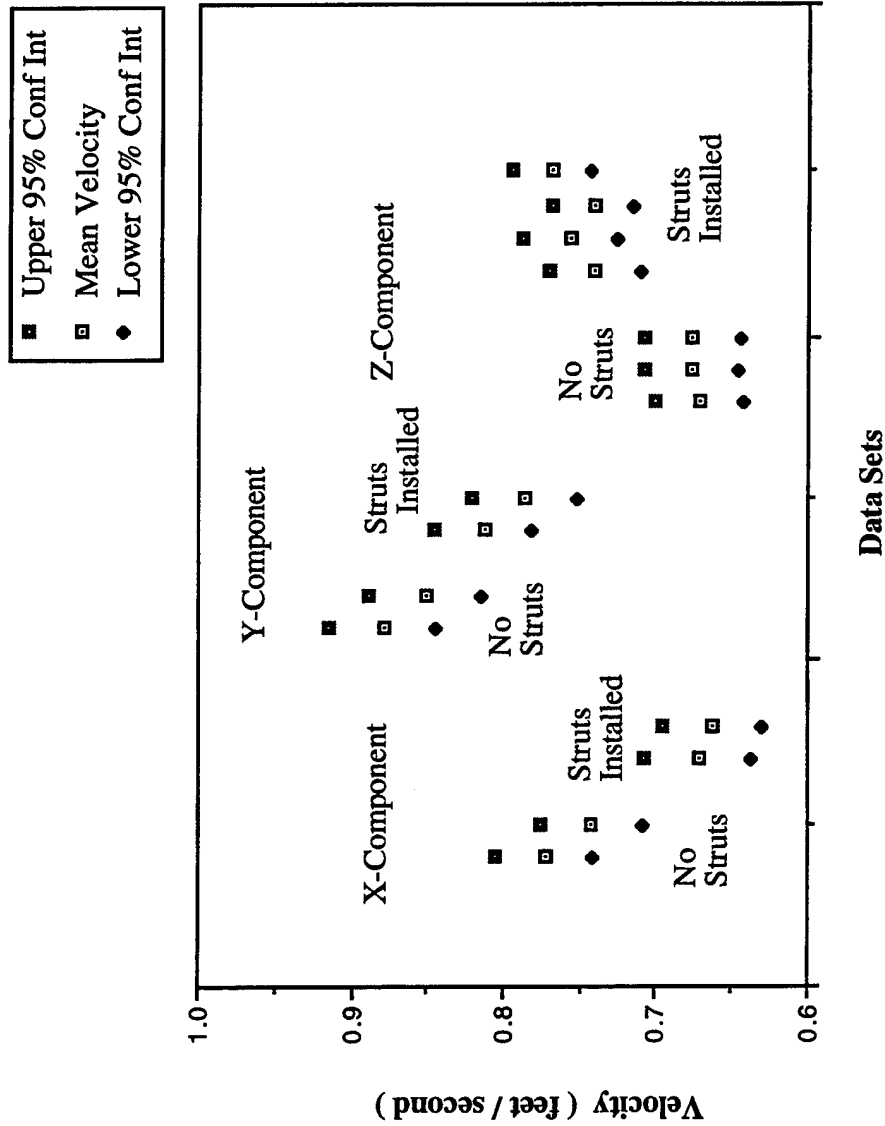
Reduced test data are presented in this appendix in tabular and graphic form. Points "A" through "I" and Levels "Lower" through "Upper" refer to the traverse system coordinates detailed in Table III.1 and illustrated in Figure III.1. All velocities (e.g. ordinate for graphics; mean, standard deviation, 95% confidence interval, low, and high in tables) are in meters per second. "Points" indicates the number of velocity measurements samples in the data set.

Point A Data

POINT	STRUTS	COMPONENT	MEAN	STD DEV	POINTS	95% CONF INT	LOW	HIGH
A	OFF	X	0.6156	0.5681	1023	0.0348	0.5808	0.6504
A	OFF	X	0.6045	0.5612	1024	0.0344	0.5701	0.6389
A	ON	X	0.0640	0.5324	1021	0.0327	0.0313	0.0967
A	ON	X	0.0689	0.5332	1024	0.0327	0.0362	0.1016
A	OFF	Y	3.6340	1.4020	1018	0.0861	3.5479	3.7201
A	OFF	Y	3.6450	1.4810	1021	0.0908	3.5542	3.7358
A	ON	Y	0.6825	0.5474	1024	0.0335	0.6490	0.7160
A	ON	Y	0.6898	0.5501	1023	0.0337	0.6561	0.7235
A	OFF	Z	0.7030	0.4698	1023	0.0288	0.6742	0.7318
A	OFF	Z	0.7318	0.4880	1023	0.0299	0.7019	0.7617
A	ON	Z	0.7788	0.5006	1024	0.0307	0.7481	0.8095
A	ON	Z	0.8267	0.5421	1024	0.0332	0.7935	0.8599

Point A

Three Component Mean Velocities for each Data Set
with Upper and Lower Bounds of 95 % Confidence Intervals

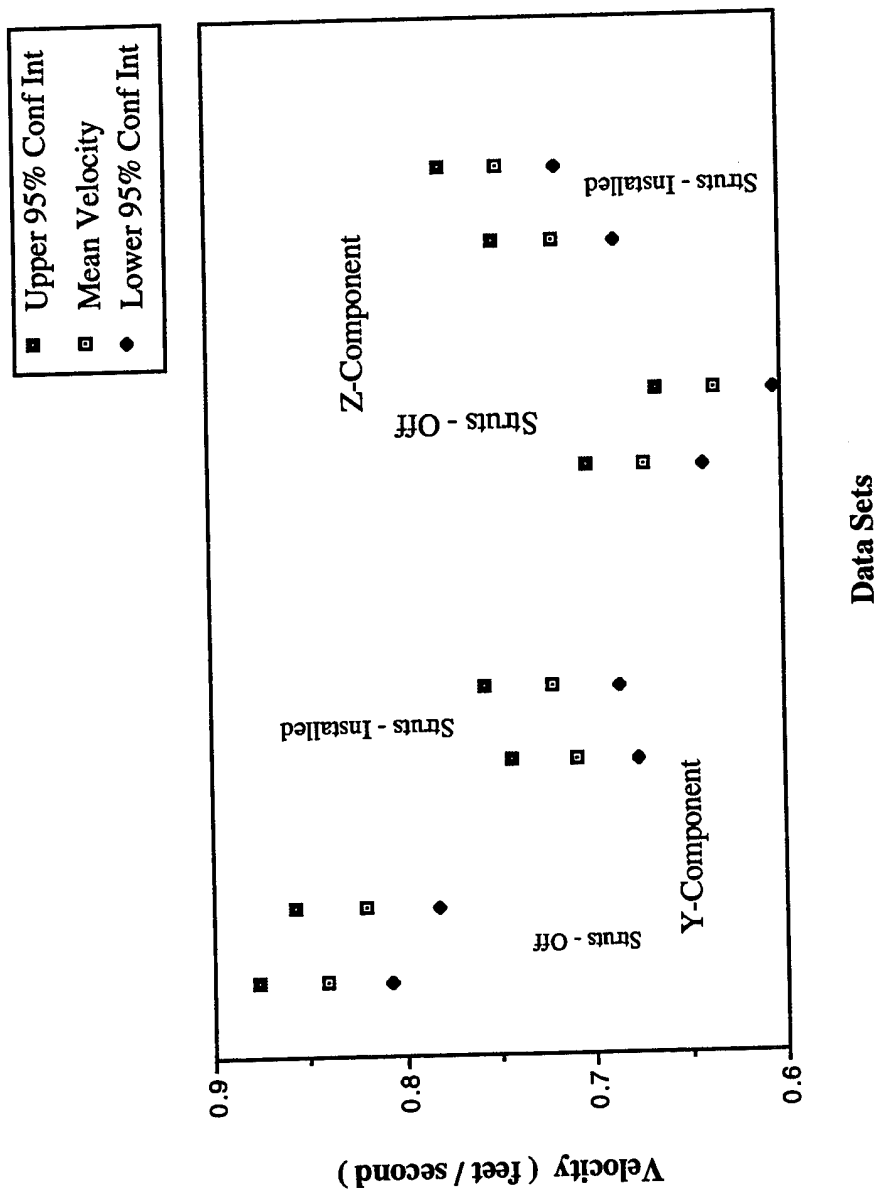


Points B and C
Data

POINT	STRUTS	COMPONENT	MEAN	STD DEV	POINTS	95% CONF INT	LOW	HIGH
B	OFF	Y	0.7384	0.5967	1024	0.0365	0.7019	0.7749
B	OFF	Y	0.7172	0.5825	1024	0.0357	0.6815	0.7529
B	ON	Y	0.6938	0.5452	1024	0.0334	0.6604	0.7272
B	ON	Y	0.7262	0.5291	1024	0.0324	0.6938	0.7586
B	OFF	Z	0.7212	0.4393	1020	0.0270	0.6942	0.7482
B	OFF	Z	0.6944	0.5035	1024	0.0308	0.6636	0.7252
B	ON	Z	0.8079	0.5177	1024	0.0317	0.7762	0.8396
B	ON	Z	0.8038	0.5091	1020	0.0312	0.7726	0.8350
C	OFF	X	0.6323	0.6086	1024	0.0373	0.5950	0.6696
C	OFF	X	0.6923	0.6209	1024	0.0380	0.6543	0.7303
C	OFF	X	0.6423	0.5771	1024	0.0353	0.6070	0.6776
C	ON	X	0.6461	0.5381	1024	0.0330	0.6131	0.6791
C	ON	X	0.6728	0.5452	1024	0.0334	0.6394	0.7062

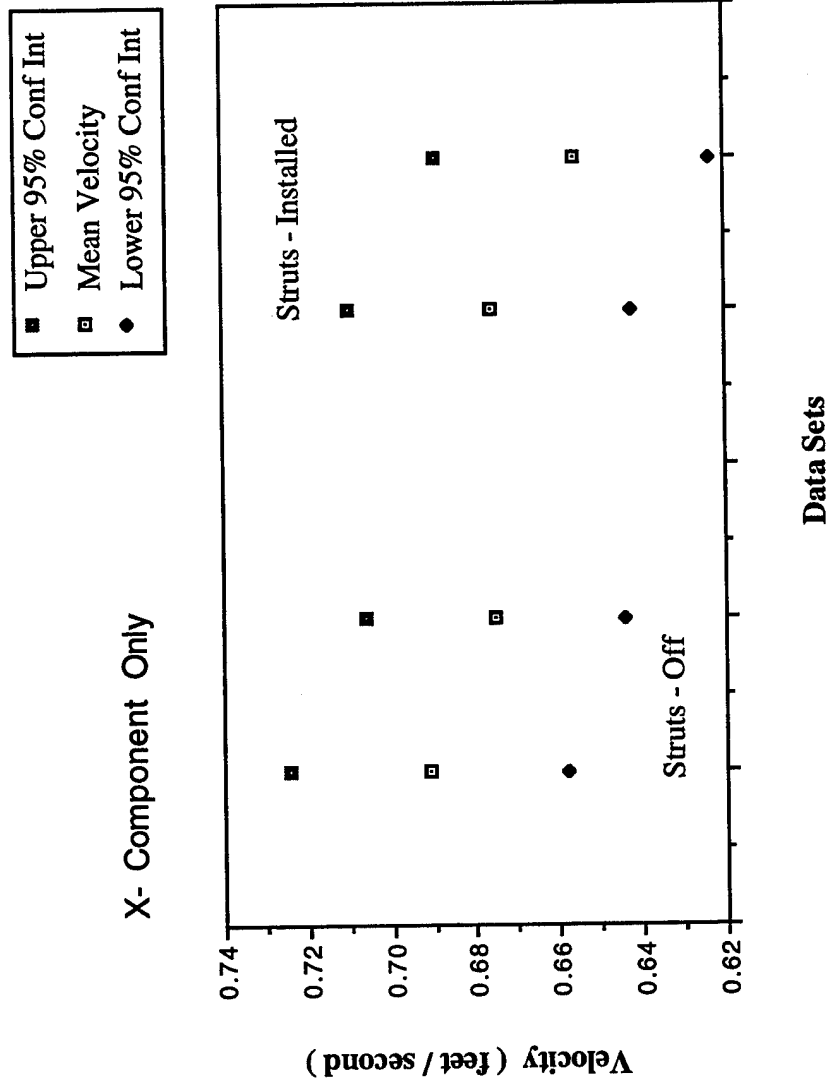
Point B

Two Component Mean Velocities for each Data Set
with Upper and Lower Bounds of 95 % Confidence Intervals



Point C

Single Component Mean Velocities for each Data Set
with Upper and Lower Bounds of 95 % Confidence Intervals



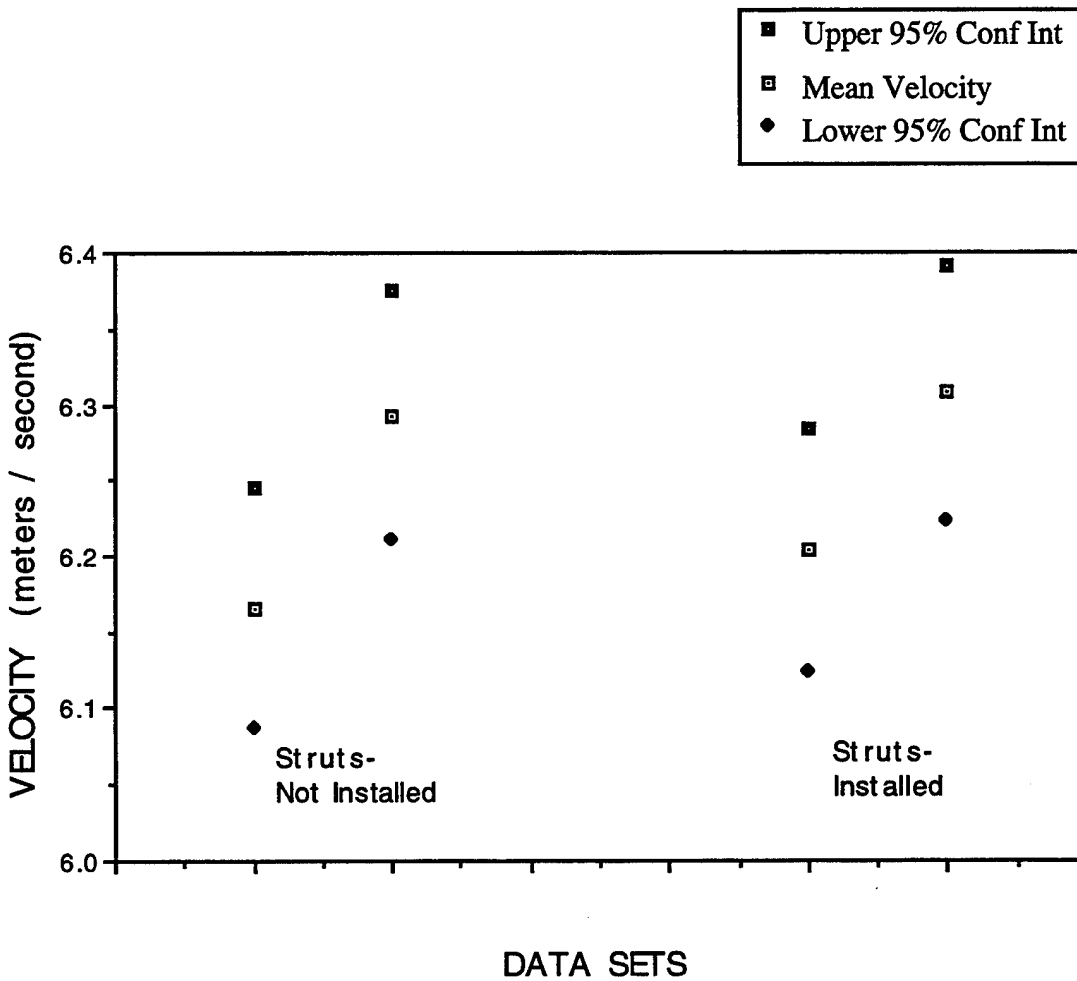
Point D/ Lower Level

Data

POINT	STRUTS	COMPONENT	MEAN	STD DEV	POINTS	95% CONF INT	LOW	HIGH
D	OFF	X	6.166	1.289	1022	0.079	6.087	6.245
D	OFF	X	6.293	1.338	1020	0.082	6.211	6.375
D	ON	X	6.203	1.307	1015	0.080	6.123	6.283
D	ON	X	6.307	1.380	1023	0.085	6.222	6.392
D	OFF	Y	6.648	1.568	1023	0.096	6.552	6.744
D	OFF	Y	6.766	1.542	1023	0.094	6.672	6.860
D	ON	Y	6.688	1.600	1024	0.098	6.590	6.786
D	ON	Y	6.772	1.569	1024	0.096	6.676	6.868
D	OFF	Z	5.360	1.529	1023	0.094	5.266	5.454
D	OFF	Z	5.410	1.598	1024	0.098	5.312	5.508
D	ON	Z	5.217	1.544	1022	0.095	5.122	5.312
D	ON	Z	5.367	1.602	1024	0.098	5.269	5.465

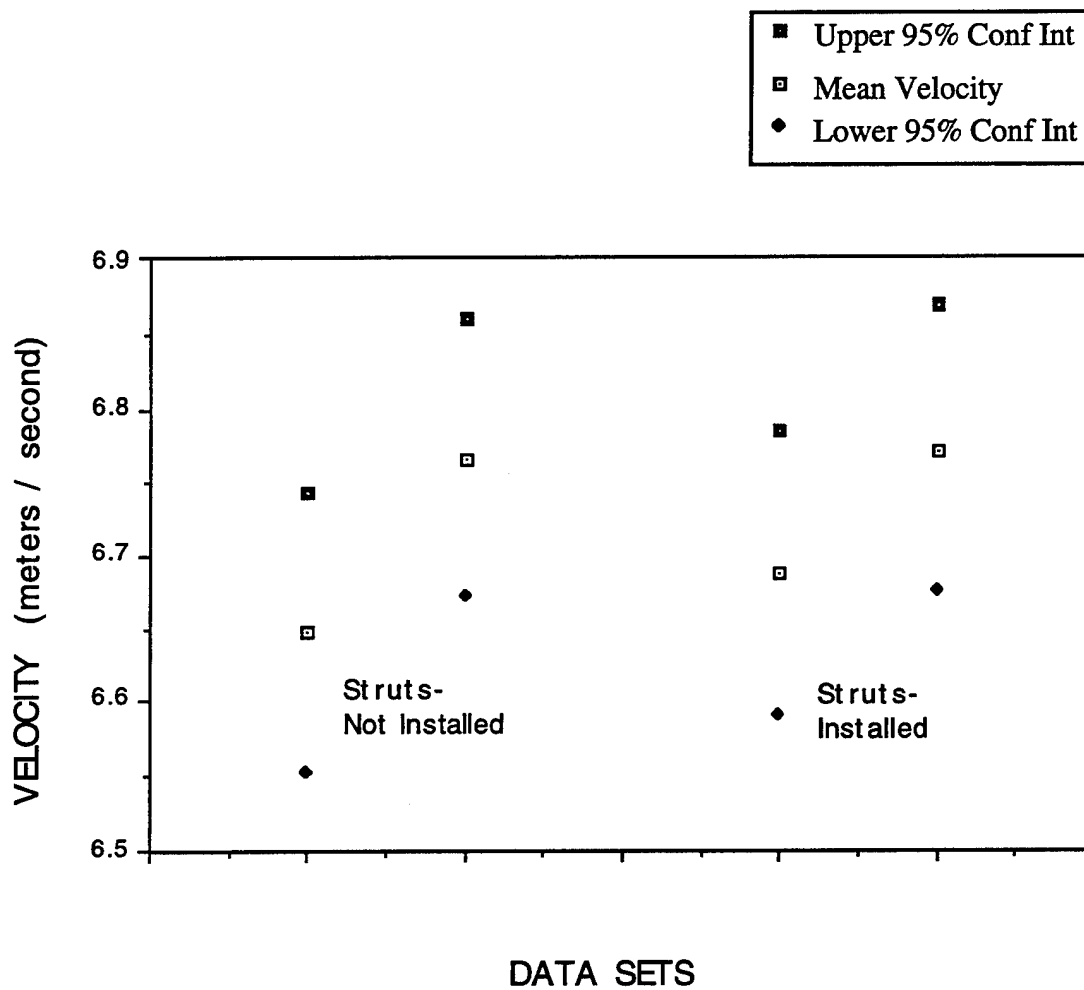
Point D / Lower Level / X- Component

Mean Velocity Components for Data Sets with
Upper and Lower Bounds of 95 % Confidence Intervals



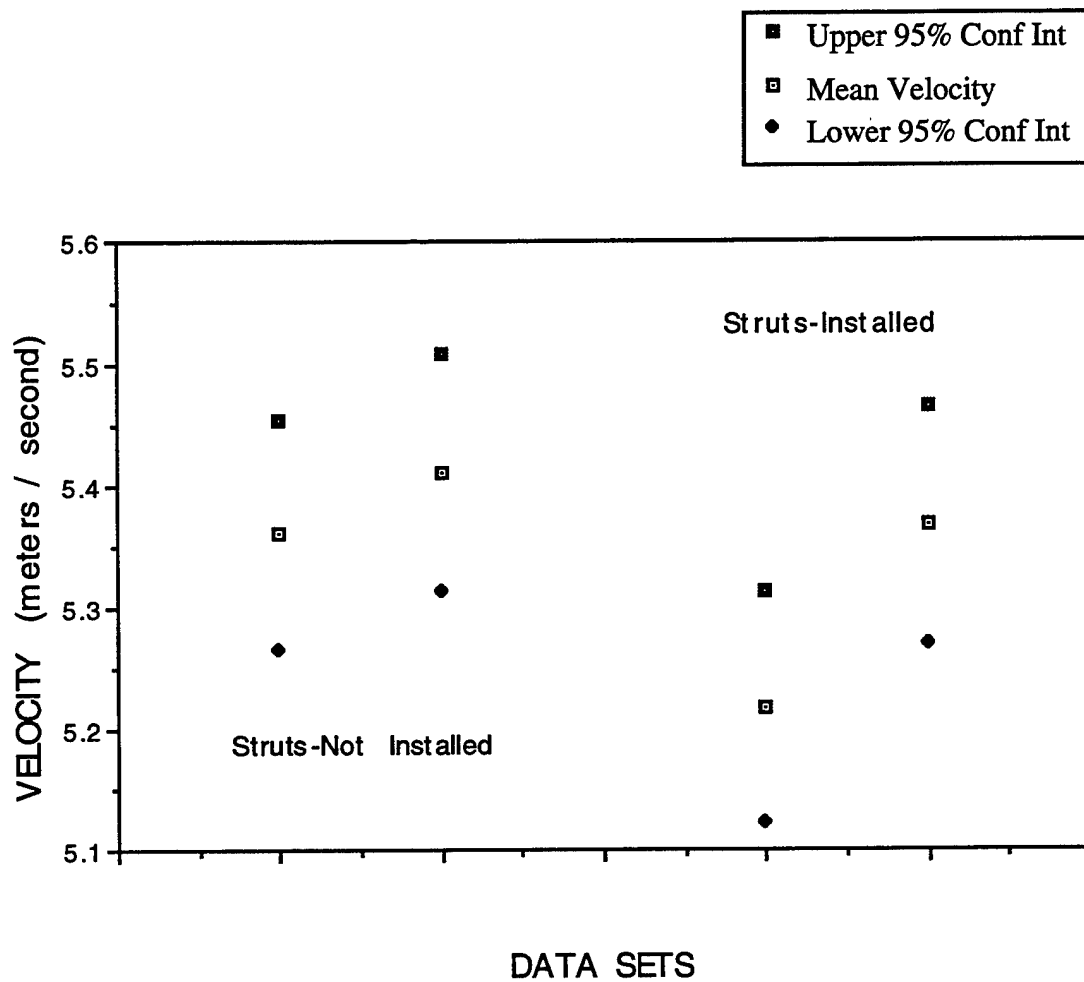
Point D / Lower Level / Y- Component

Mean Velocity Components for Data Sets with
Upper and Lower Bounds of 95 % Confidence Intervals



Point D / Lower Level / Z- Component

Mean Velocity Components for Data Sets with
Upper and Lower Bounds of 95 % Confidence Intervals



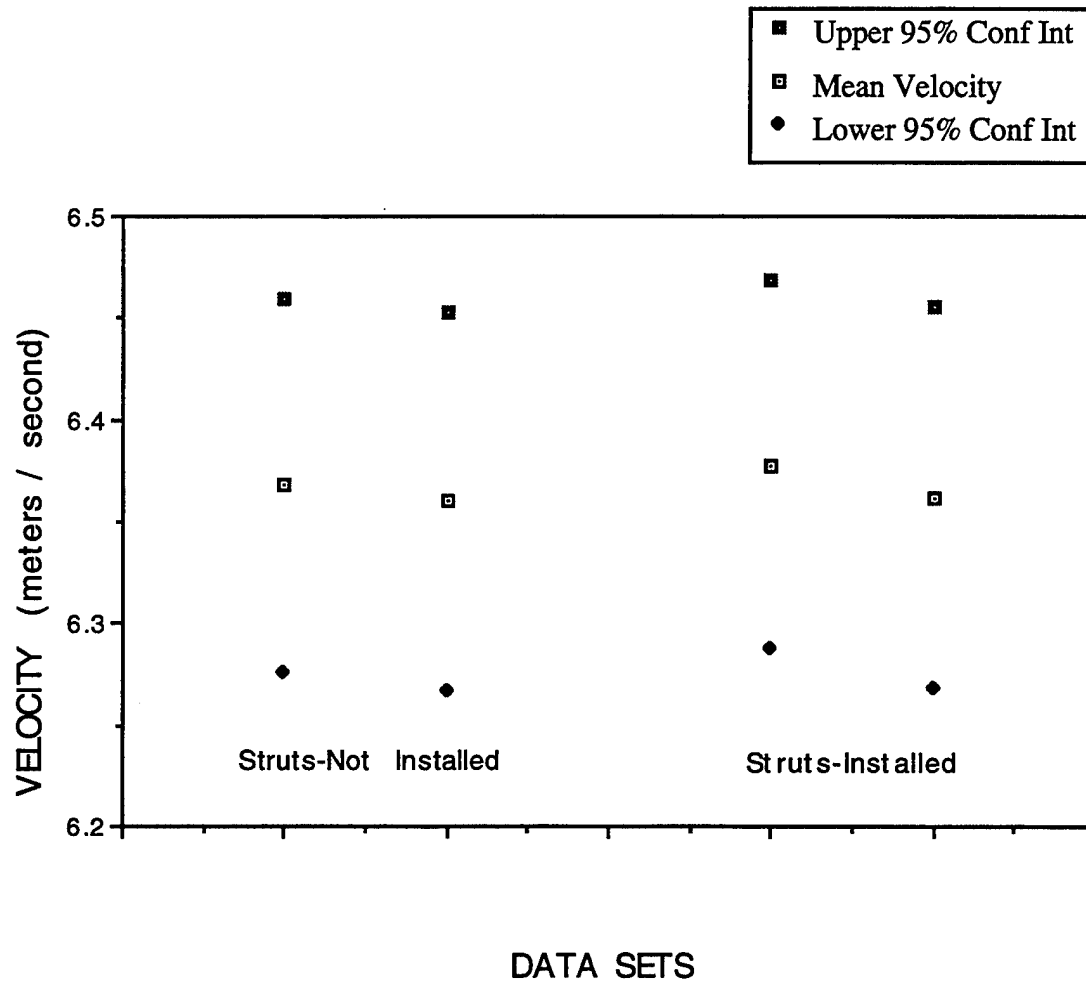
Point E/ Lower Level

Data

POINT	STRUTS	COMPONENT	MEAN	STD DEV	POINTS	95% CONF INT	LOW	HIGH
E	OFF	X	6.368	1.498	1022	0.092	6.276	6.460
E	OFF	X	6.360	1.507	1018	0.093	6.267	6.453
E	ON	X	6.378	1.481	1022	0.091	6.287	6.469
E	ON	X	6.362	1.525	1021	0.094	6.268	6.456
E	OFF	Y	6.838	1.729	1024	0.106	6.732	6.944
E	OFF	Y	6.771	1.661	4096	0.051	6.720	6.822
E	ON	Y	6.851	1.716	4095	0.053	6.798	6.904
E	ON	Y	6.842	1.764	1024	0.108	6.734	6.950
E	OFF	Z	0.907	0.440	1018	0.027	0.880	0.934
E	OFF	Z	0.898	0.401	1023	0.025	0.873	0.922
E	ON	Z	0.903	0.407	1022	0.025	0.878	0.928
E	ON	Z	0.884	0.428	1022	0.026	0.857	0.910

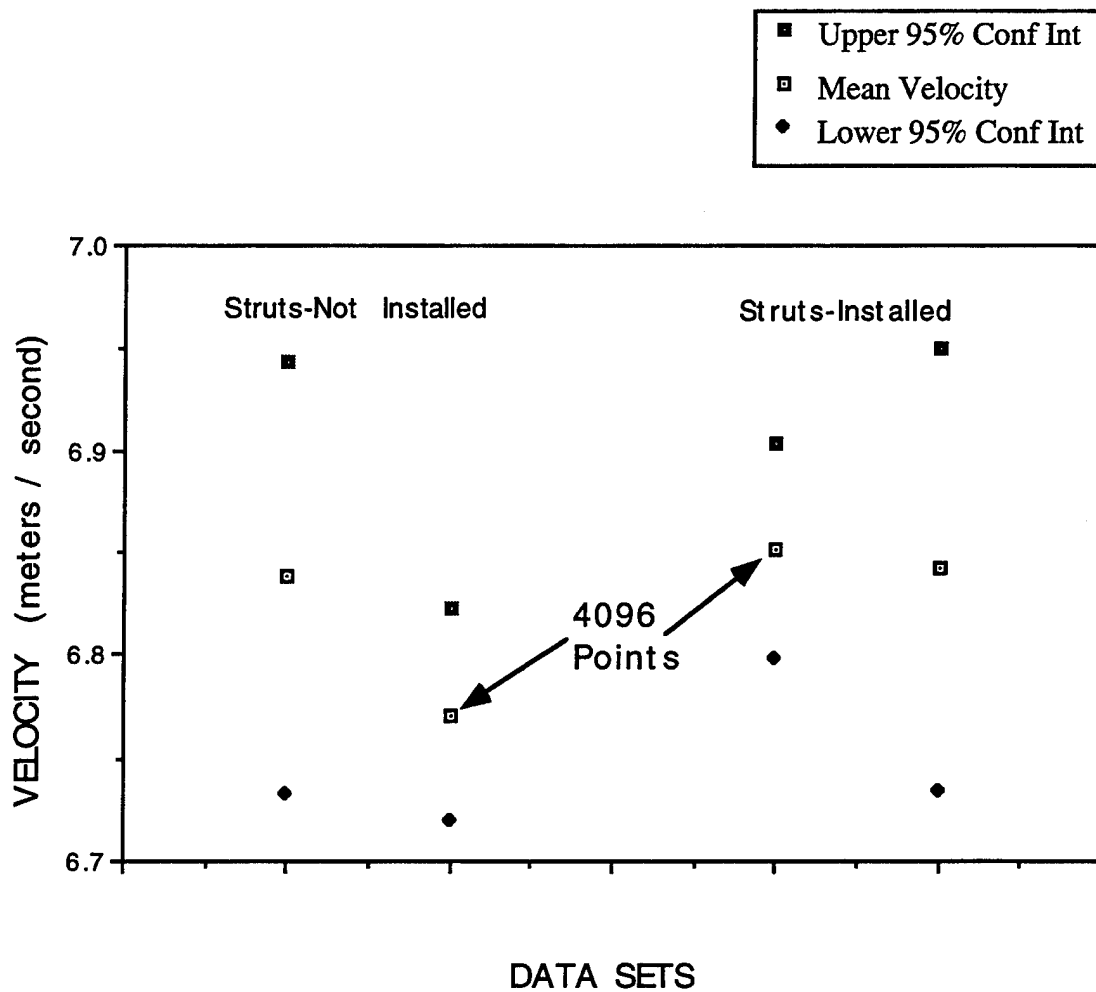
Point E / Lower Level / X- Component

Mean Velocity Components for Data Sets with
Upper and Lower Bounds of 95 % Confidence Intervals



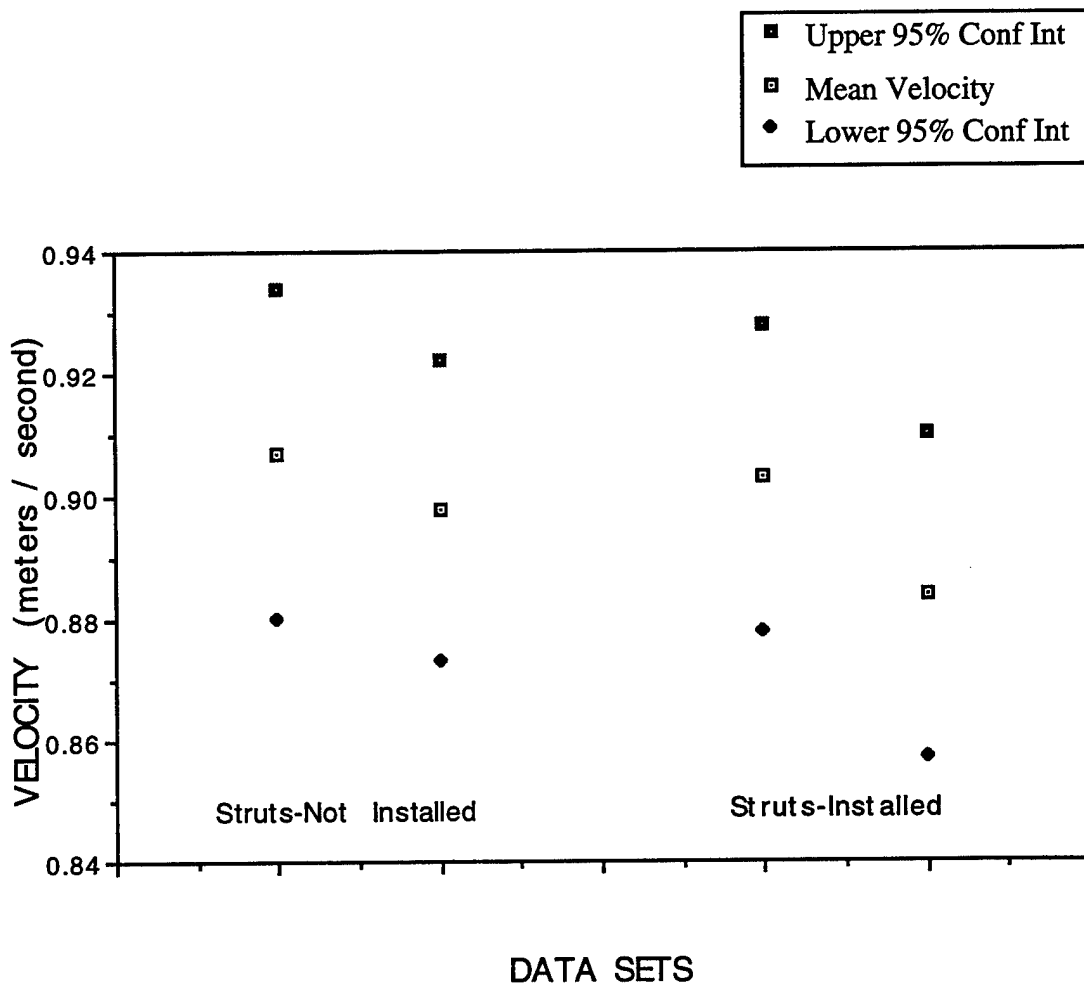
Point E / Lower Level / Y- Component

Mean Velocity Components for Data Sets with
Upper and Lower Bounds of 95 % Confidence Intervals



Point E / Lower Level / Z- Component

Mean Velocity Components for Data Sets with
Upper and Lower Bounds of 95 % Confidence Intervals



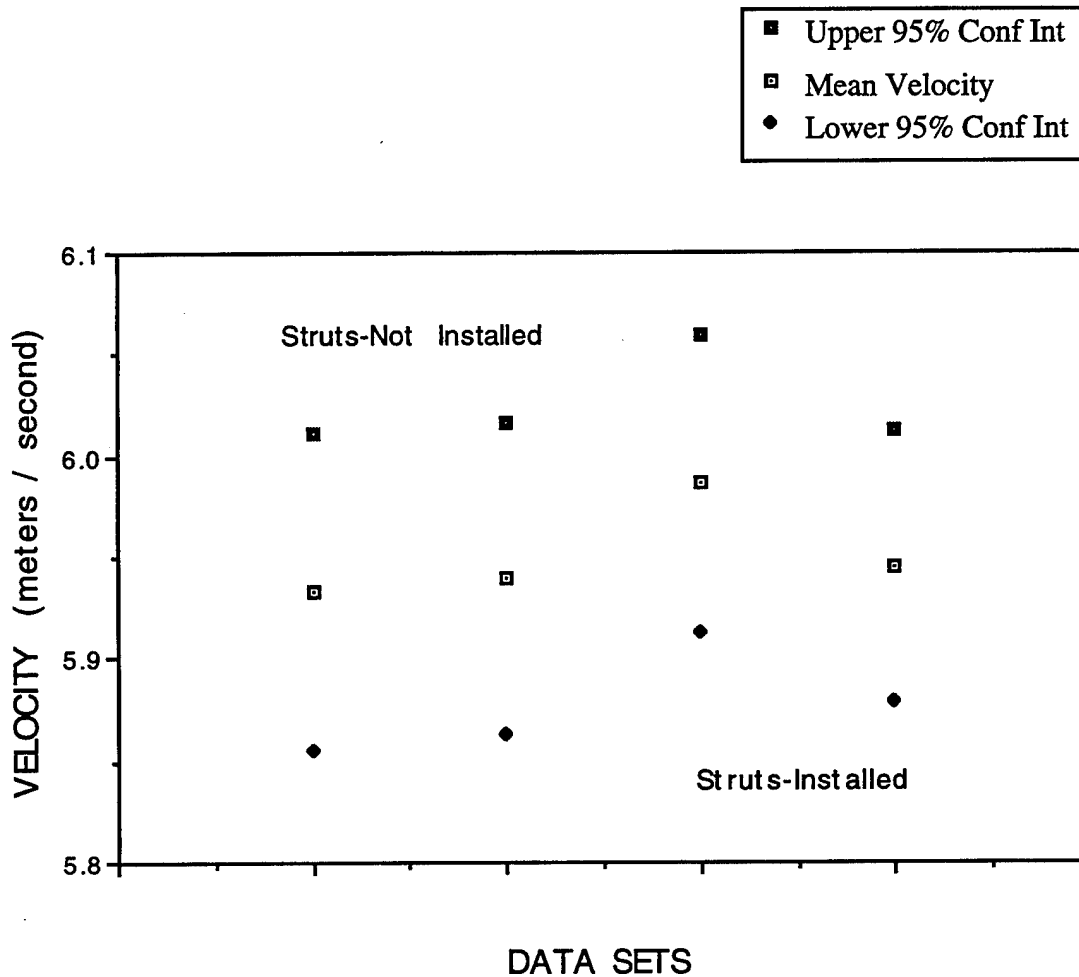
Point F/ Lower Level

Data

POINT	STRUTS	COMPONENT	MEAN	STD DEV	POINTS	95% CONF INT	LOW	HIGH
F	OFF	X	5.933	1.264	1018	0.078	5.855	6.011
F	OFF	X	5.940	1.265	1024	0.077	5.863	6.017
F	ON	X	5.986	1.202	1020	0.074	5.912	6.060
F	ON	X	5.945	1.097	1022	0.067	5.878	6.012
F	OFF	Y	6.783	1.777	1024	0.109	6.674	6.892
F	OFF	Y	6.701	1.702	1024	0.104	6.597	6.805
F	ON	Y	6.828	1.786	1024	0.109	6.719	6.937
F	ON	Y	6.703	1.664	1024	0.102	6.601	6.805
F	OFF	Z	6.179	1.005	1023	0.062	6.117	6.241
F	OFF	Z	6.193	1.039	1018	0.064	6.129	6.257
F	ON	Z	6.180	1.044	1021	0.064	6.116	6.244
F	ON	Z	6.215	1.079	1020	0.066	6.149	6.281

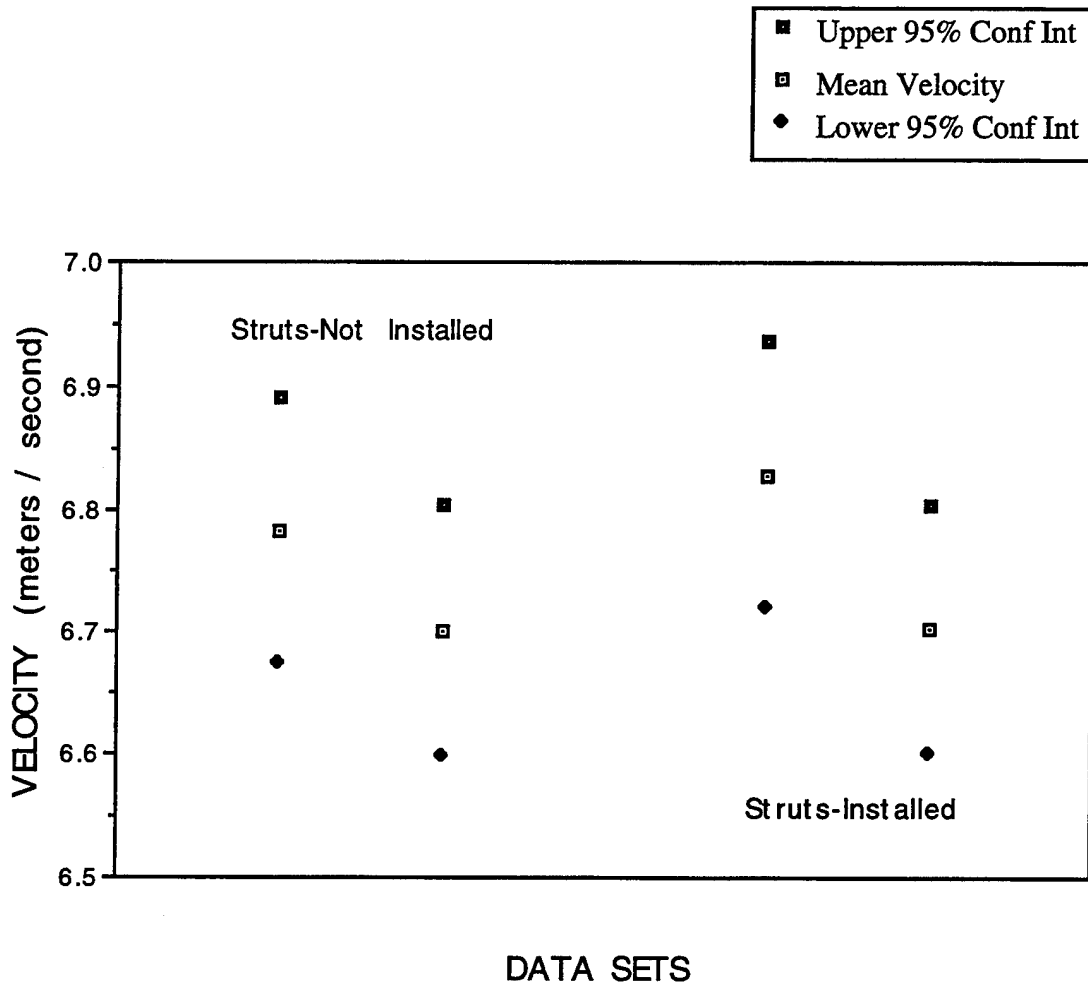
Point F / Lower Level / X- Component

Mean Velocity Components for Data Sets with
Upper and Lower Bounds of 95 % Confidence Intervals



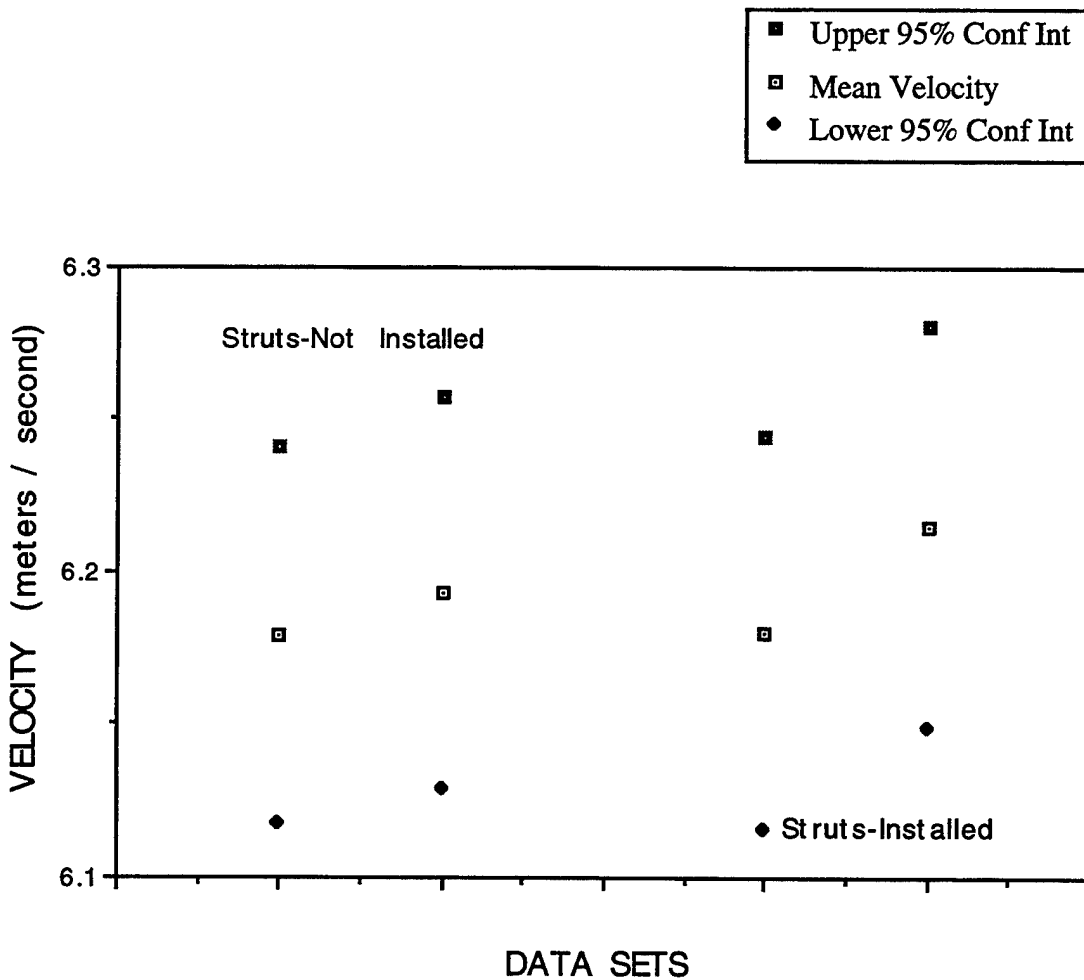
Point F / Lower Level / Y- Component

Mean Velocity Components for Data Sets with
Upper and Lower Bounds of 95 % Confidence Intervals



Point F / Lower Level / Z- Component

Mean Velocity Components for Data Sets with
Upper and Lower Bounds of 95 % Confidence Intervals



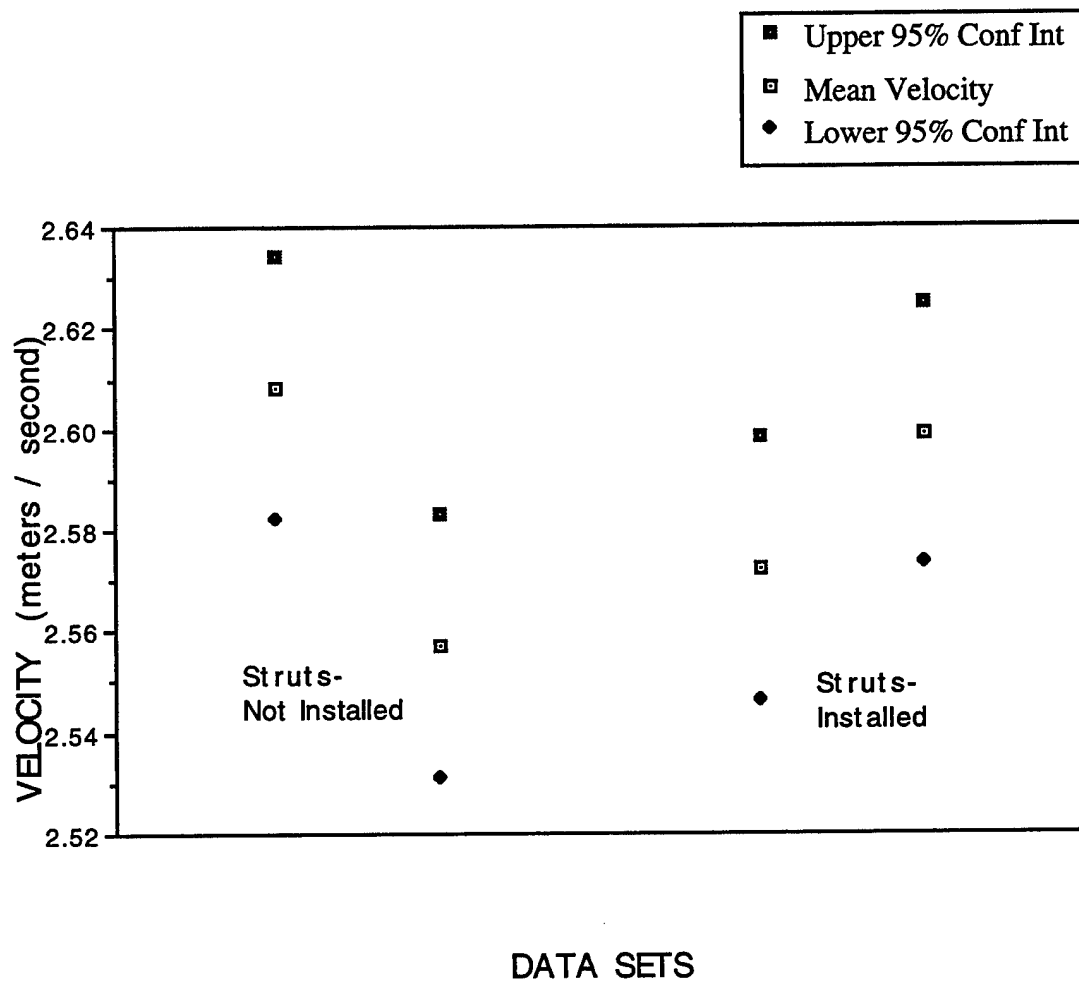
Point G/ Lower Level

Data

POINT	STRUTS	COMPONENT	MEAN	STD DEV	POINTS	95% CONF INT	LOW	HIGH
G	OFF	X	2.608	0.428	1024	0.026	2.582	2.634
G	OFF	X	2.557	0.425	1021	0.026	2.531	2.583
G	ON	X	2.572	0.429	1020	0.026	2.546	2.598
G	ON	X	2.599	0.430	1024	0.026	2.573	2.625
G	OFF	Y	5.952	1.577	1023	0.097	5.855	6.049
G	OFF	Y	5.874	1.482	1022	0.091	5.783	5.965
G	ON	Y	5.968	1.601	1024	0.098	5.870	6.066
G	ON	Y	5.853	1.419	1020	0.087	5.766	5.940
G	OFF	Z	2.728	0.438	1021	0.027	2.701	2.755
G	OFF	Z	2.665	0.424	1023	0.026	2.639	2.691
G	ON	Z	2.709	0.417	1024	0.026	2.683	2.735
G	ON	Z	2.694	0.425	1023	0.026	2.668	2.720

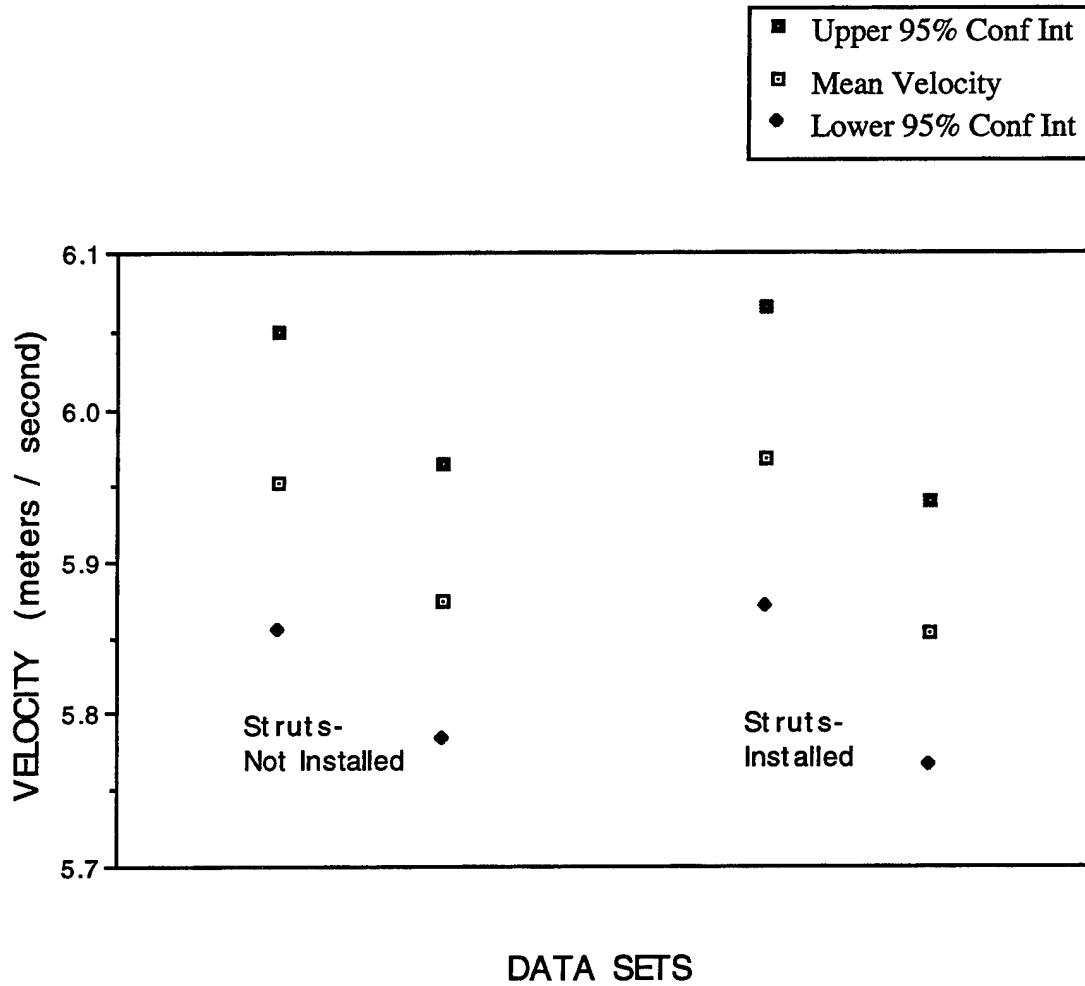
Point G / Lower Level / X- Component

Mean Velocity Components for Data Sets with
Upper and Lower Bounds of 95 % Confidence Intervals



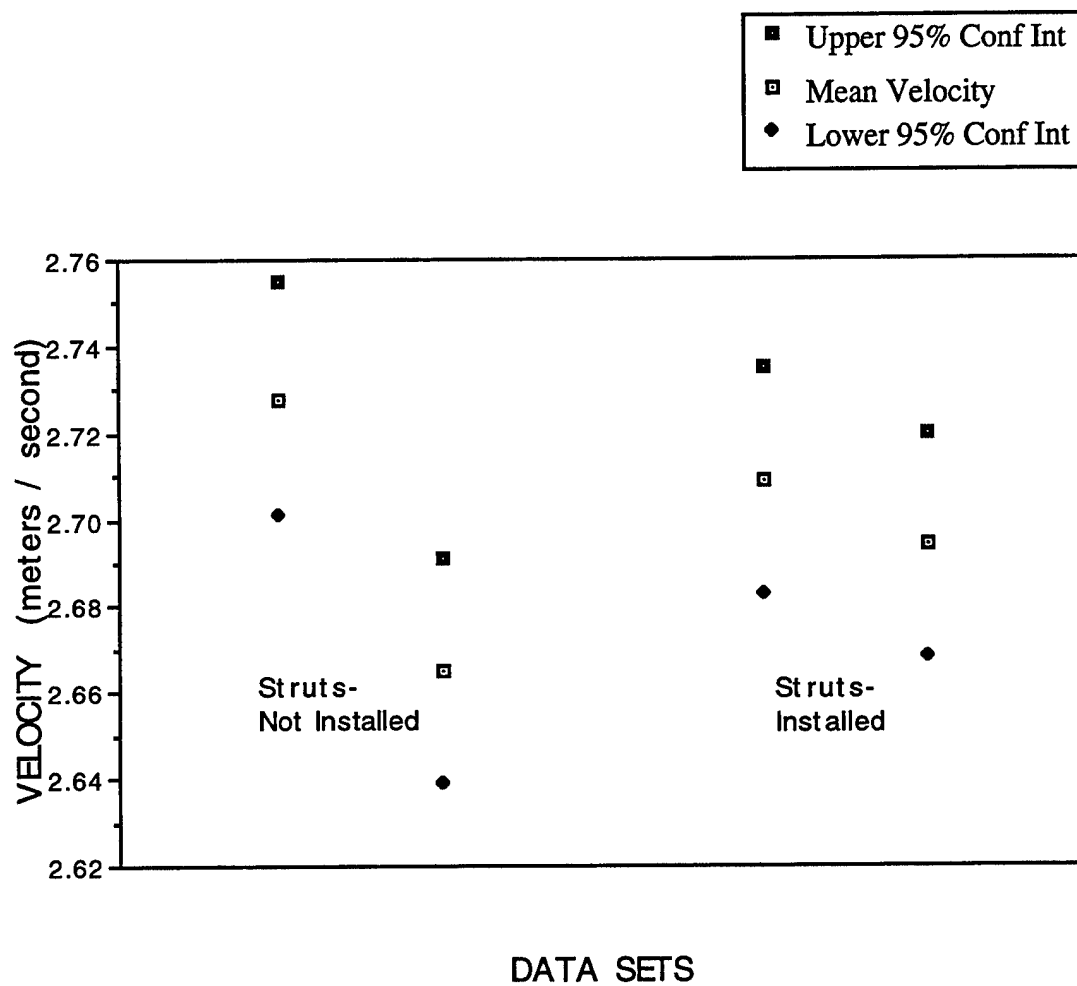
Point G / Lower Level / Y- Component

Mean Velocity Components for Data Sets with
Upper and Lower Bounds of 95 % Confidence Intervals



Point G / Lower Level / Z- Component

Mean Velocity Components for Data Sets with
Upper and Lower Bounds of 95 % Confidence Intervals



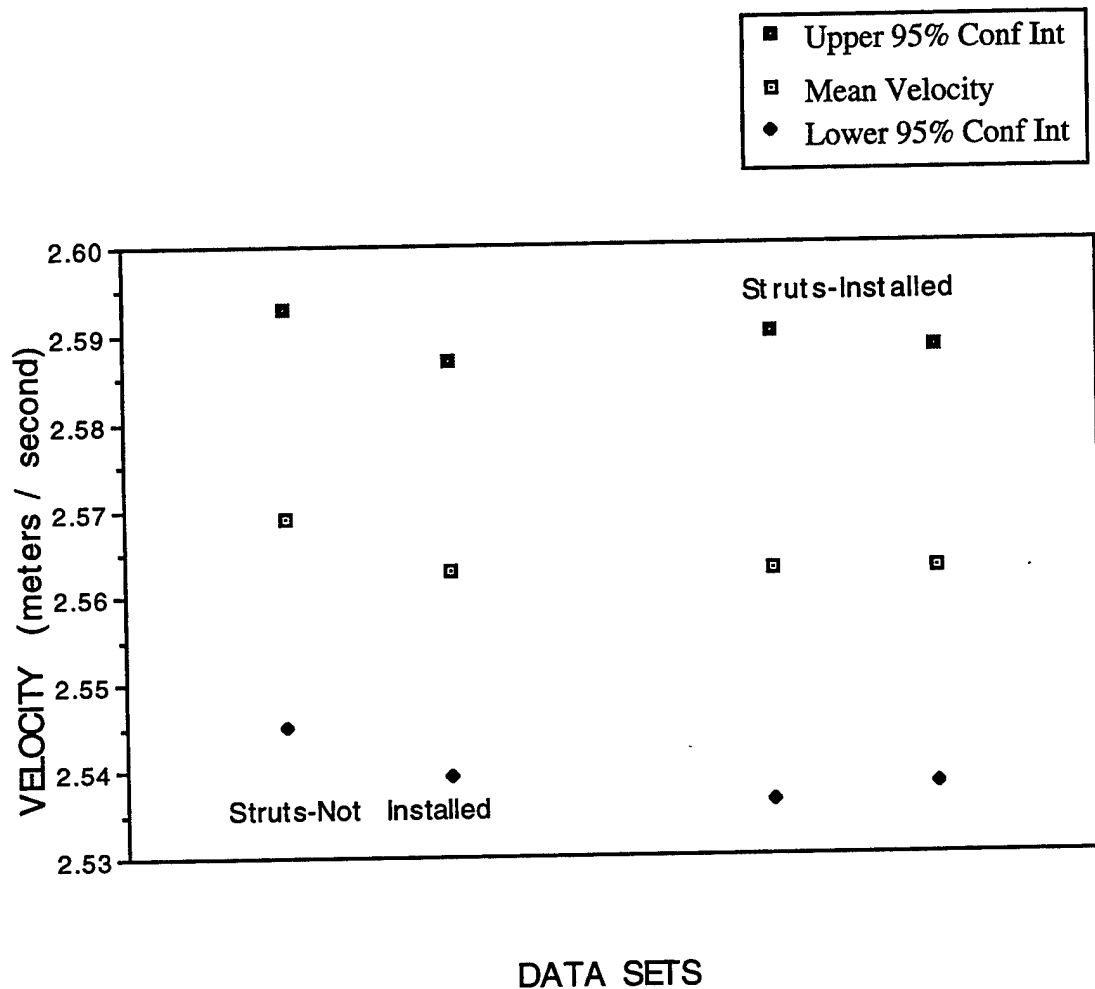
Point H/ Lower Level

Data

POINT	STRUTS	COMPONENT	MEAN	STD DEV	POINTS	95% CONF INT	LOW	HIGH
H	OFF	X	2.569	0.399	1023	0.024	2.545	2.593
H	OFF	X	2.563	0.397	1020	0.024	2.539	2.587
H	ON	X	2.563	0.433	1023	0.027	2.536	2.590
H	ON	X	2.563	0.399	1018	0.025	2.538	2.588
H	OFF	Y	6.373	1.532	1023	0.094	6.279	6.467
H	OFF	Y	6.314	1.489	1024	0.091	6.223	6.405
H	ON	Y	6.369	1.598	1022	0.098	6.271	6.467
H	ON	Y	6.369	1.557	1023	0.095	6.274	6.464
H	OFF	Z	6.930	1.478	1022	0.091	6.839	7.021
H	OFF	Z	6.984	1.460	1023	0.089	6.895	7.073
H	ON	Z	6.887	1.478	1022	0.091	6.796	6.978
H	ON	Z	6.936	1.555	1024	0.095	6.841	7.031

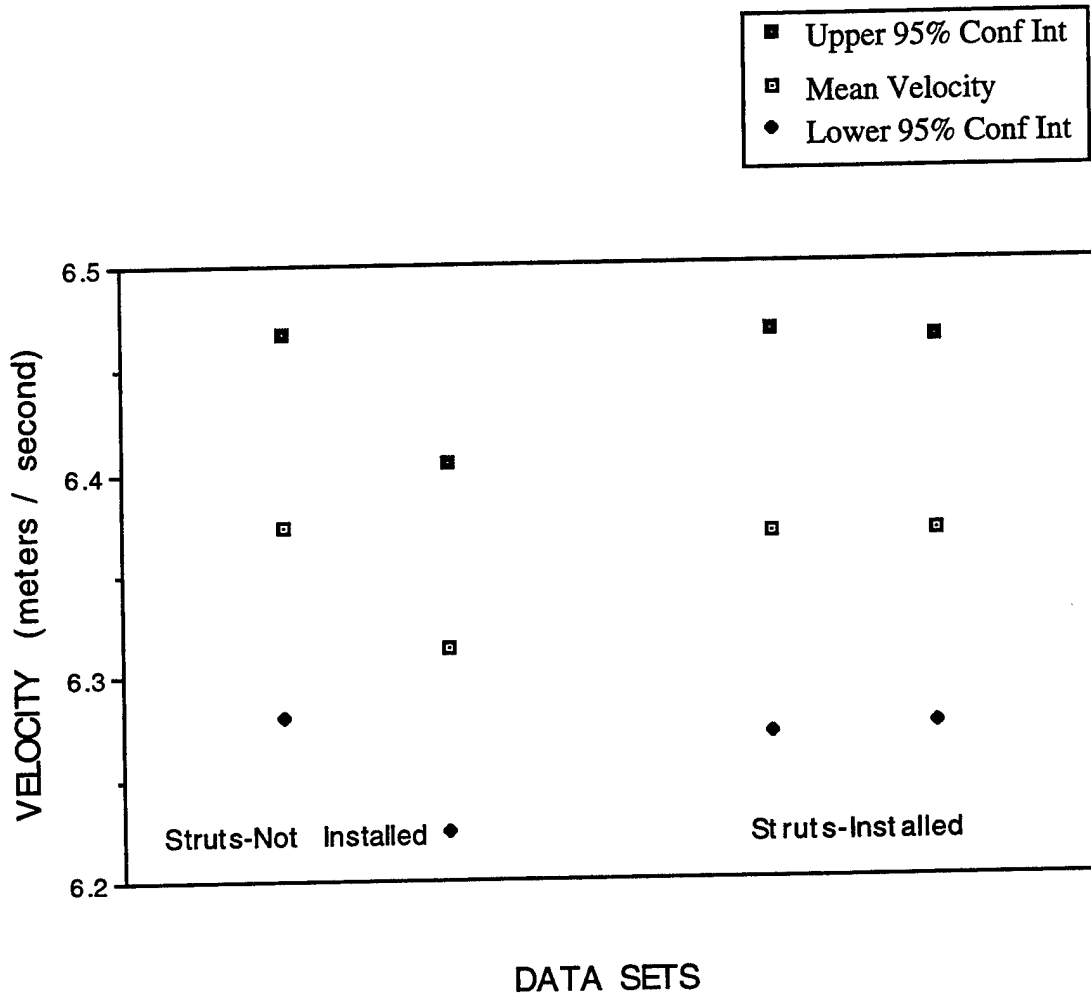
Point H / Lower Level / X- Component

Mean Velocity Components for Data Sets with
Upper and Lower Bounds of 95 % Confidence Intervals



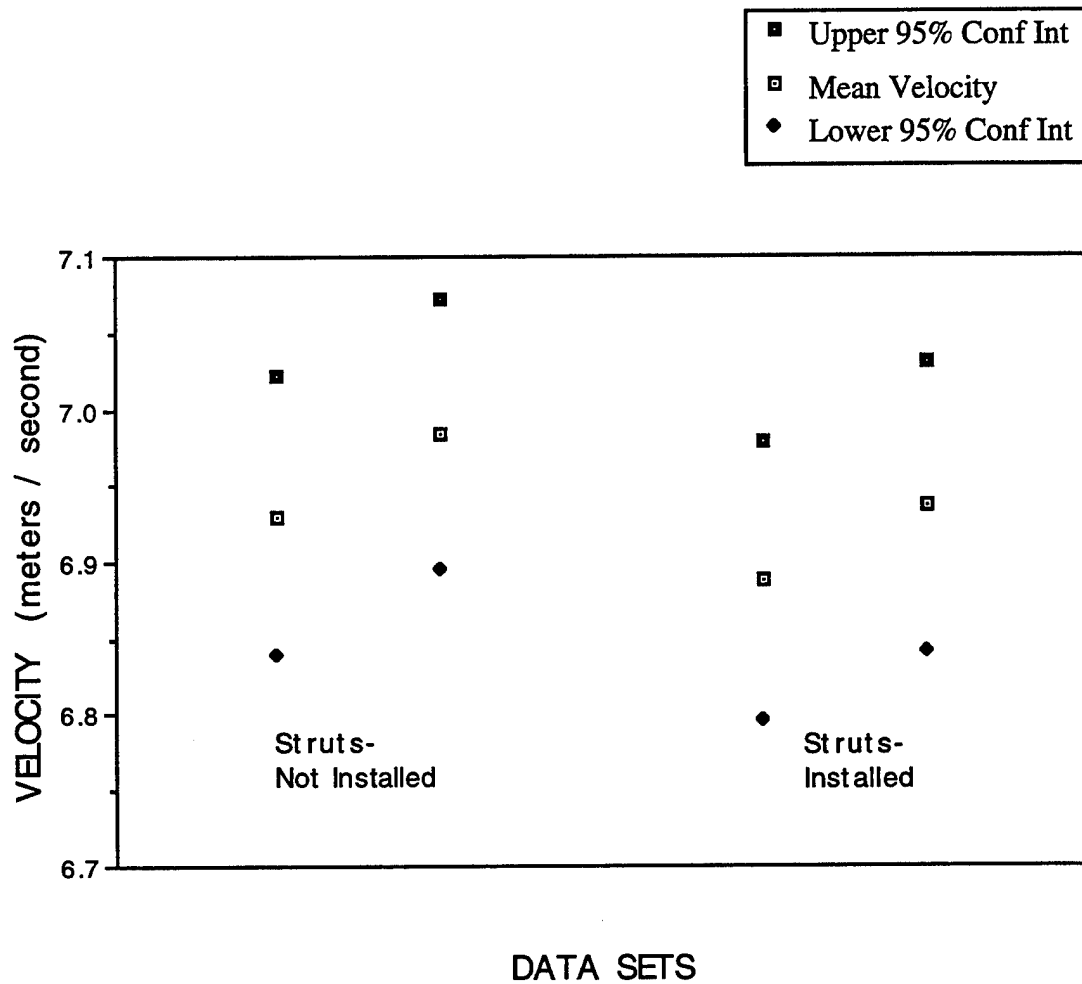
Point H / Lower Level / Y- Component

Mean Velocity Components for Data Sets with
Upper and Lower Bounds of 95 % Confidence Intervals



Point H / Lower Level / Z- Component

Mean Velocity Components for Data Sets with
Upper and Lower Bounds of 95 % Confidence Intervals



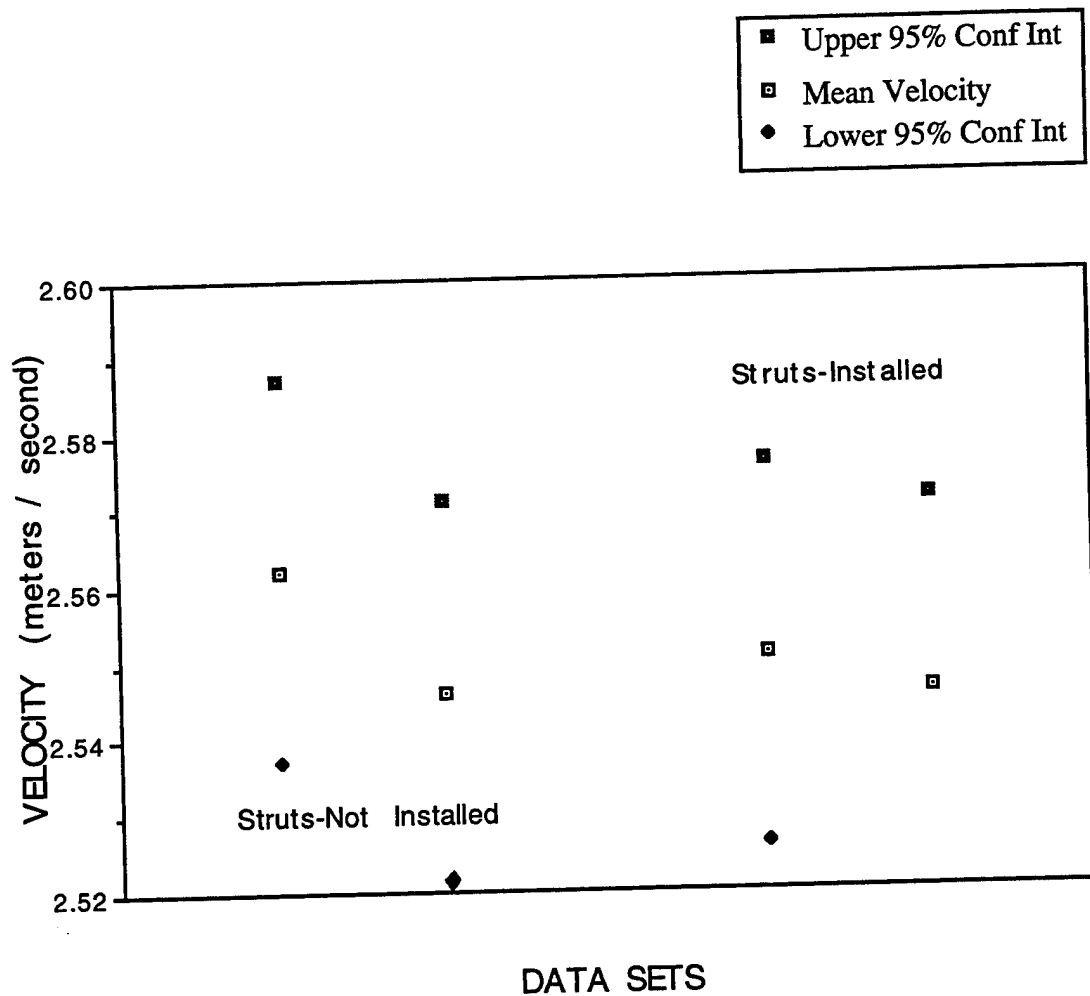
Point I/ Lower Level

Data

POINT	STRUTS	COMPONENT	MEAN	STD DEV	POINTS	95% CONF INT	LOW	HIGH
I	OFF	X	2.562	0.408	1021	0.025	2.537	2.587
I	OFF	X	2.546	0.416	1022	0.025	2.521	2.571
I	ON	X	2.551	0.410	1018	0.025	2.526	2.576
I	ON	X	2.546	0.400	1017	0.025	2.521	2.571
I	OFF	Y	2.634	0.491	1023	0.030	2.604	2.664
I	OFF	Y	2.656	0.445	1023	0.027	2.629	2.683
I	ON	Y	2.649	0.485	1024	0.030	2.619	2.679
I	ON	Y	2.652	0.441	1020	0.027	2.625	2.679
I	OFF	Z	6.837	1.223	1021	0.075	6.762	6.912
I	OFF	Z	6.868	1.319	1000	0.082	6.786	6.950
I	ON	Z	6.845	1.418	1024	0.087	6.758	6.932
I	ON	Z	6.894	1.270	1020	0.078	6.816	6.972

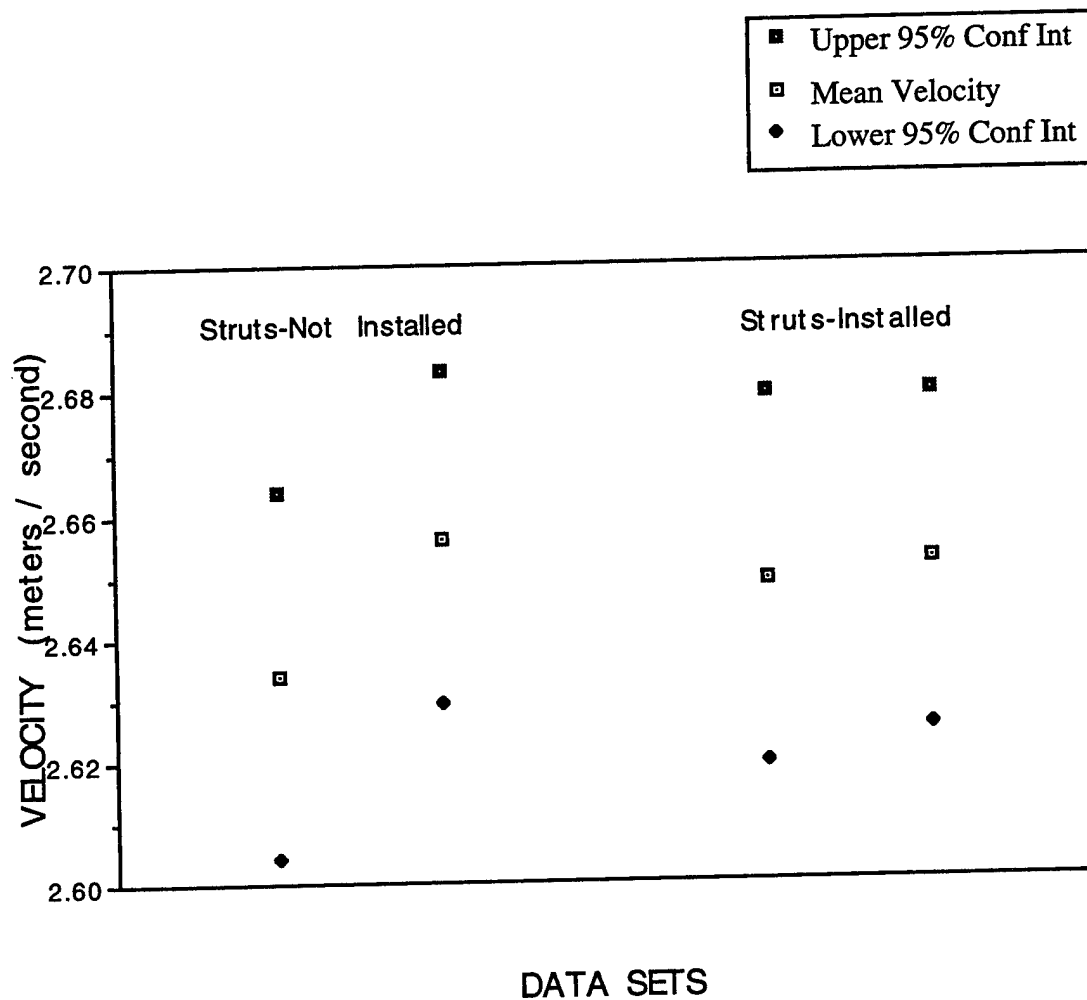
Point I / Lower Level / X- Component

Mean Velocity Components for Data Sets with
Upper and Lower Bounds of 95 % Confidence Intervals



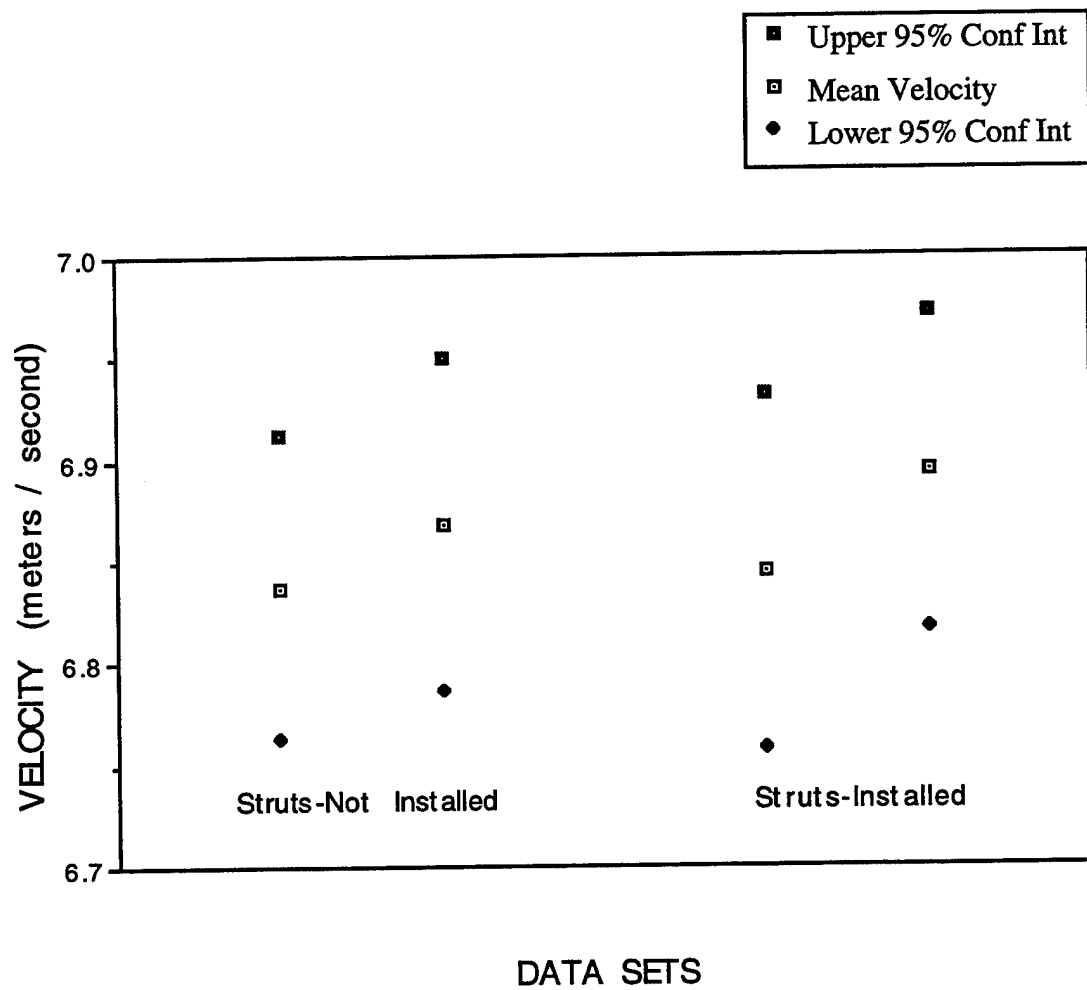
Point I / Lower Level / Y- Component

Mean Velocity Components for Data Sets with
Upper and Lower Bounds of 95 % Confidence Intervals



Point I / Lower Level / Z- Component

Mean Velocity Components for Data Sets with
Upper and Lower Bounds of 95 % Confidence Intervals



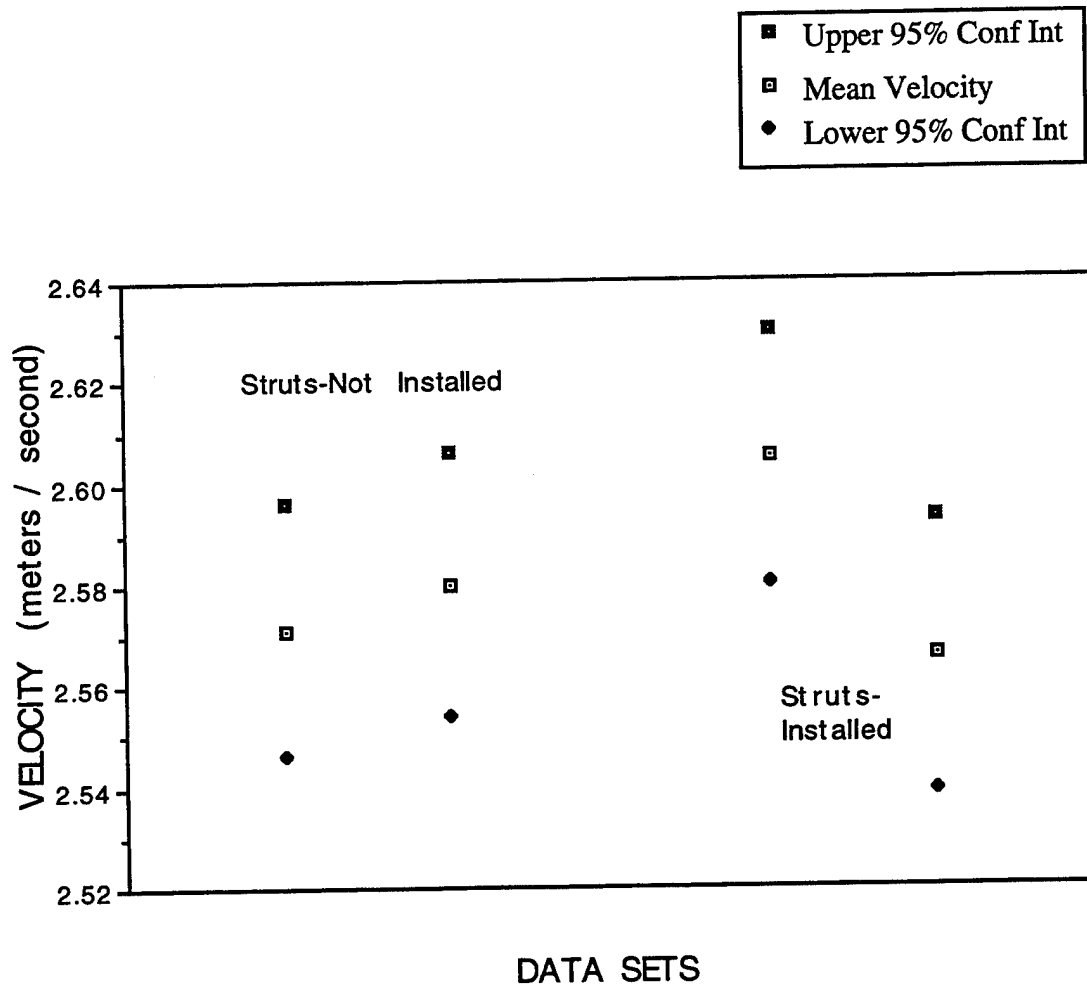
Point G/ Mid Level

Data

POINT	STRUTS	COMPONENT	MEAN	STD DEV	POINTS	95% CONF INT	LOW	HIGH
G	OFF	X	2.571	0.411	1020	0.025	2.546	2.596
G	OFF	X	2.580	0.423	1022	0.026	2.554	2.606
G	ON	X	2.605	0.413	1017	0.025	2.580	2.630
G	ON	X	2.566	0.435	1020	0.027	2.539	2.593
G	OFF	Y	5.452	1.261	1013	0.078	5.374	5.530
G	OFF	Y	5.532	1.265	1020	0.078	5.454	5.610
G	ON	Y	5.483	1.250	1014	0.077	5.406	5.560
G	ON	Y	5.465	1.232	1014	0.076	5.389	5.541
G	OFF	Z	2.659	0.406	1020	0.025	2.634	2.684
G	OFF	Z	2.641	0.447	1023	0.027	2.614	2.668
G	ON	Z	2.665	0.428	1020	0.026	2.639	2.691
G	ON	Z	2.655	0.445	1021	0.027	2.628	2.682

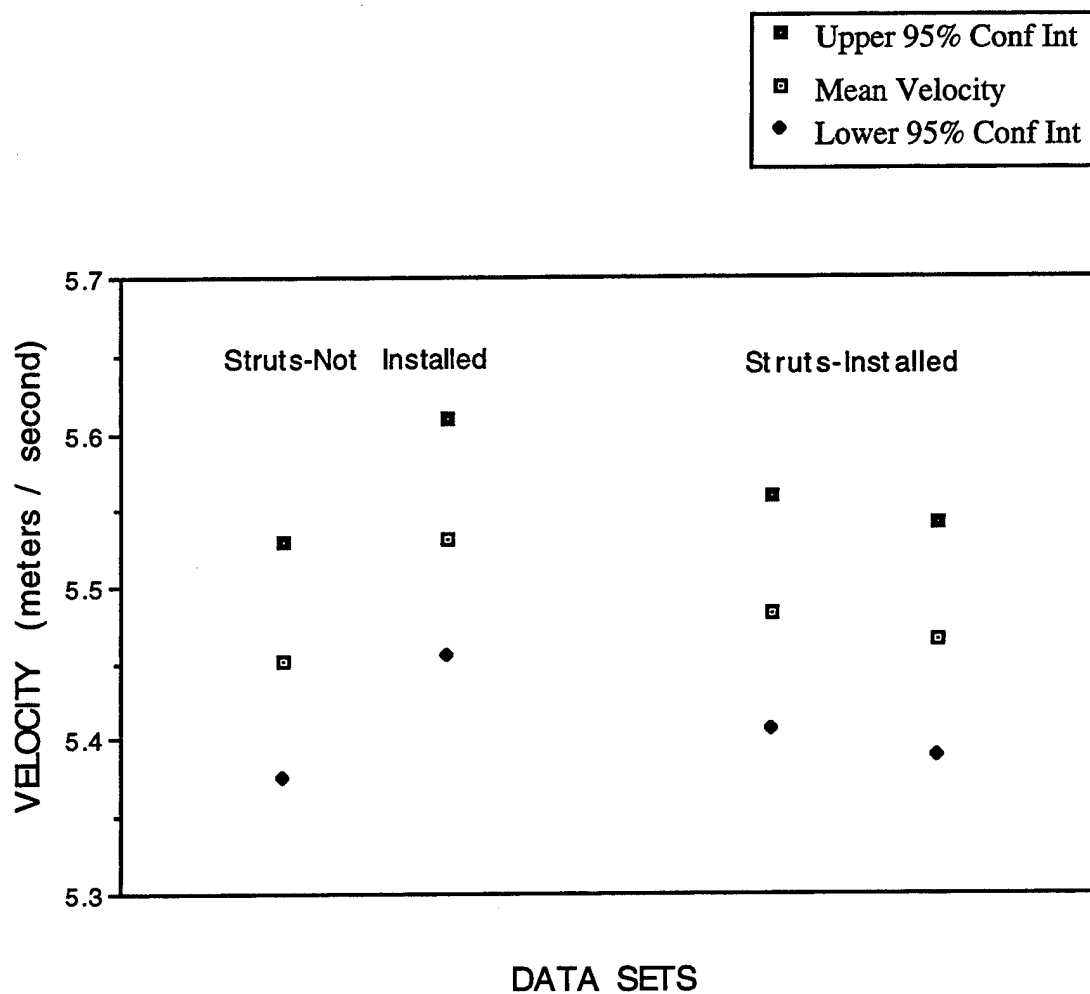
Point G / Mid Level / X- Component

Mean Velocity Components for Data Sets with
Upper and Lower Bounds of 95 % Confidence Intervals



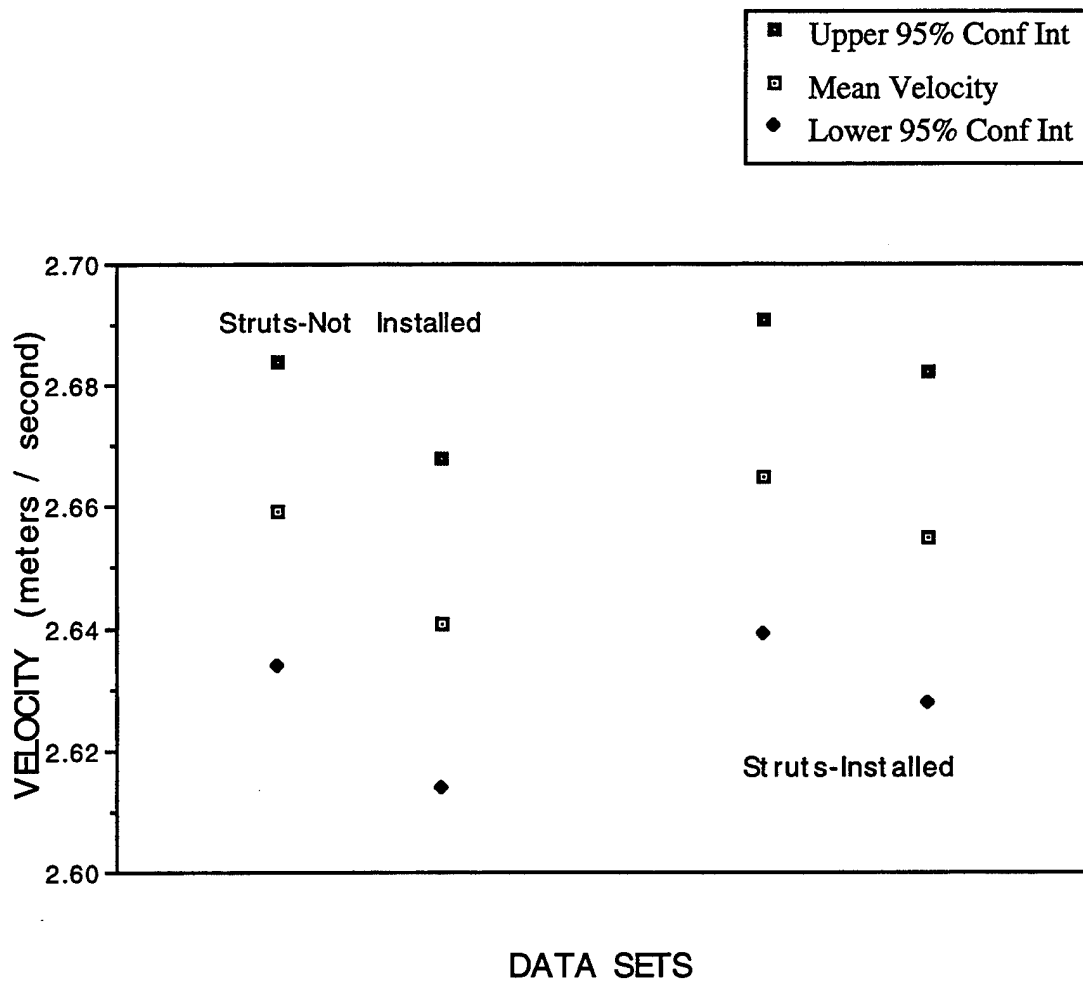
Point G / Mid Level / Y- Component

Mean Velocity Components for Data Sets with
Upper and Lower Bounds of 95 % Confidence Intervals



Point G / Mid Level / Z- Component

Mean Velocity Components for Data Sets with
Upper and Lower Bounds of 95 % Confidence Intervals



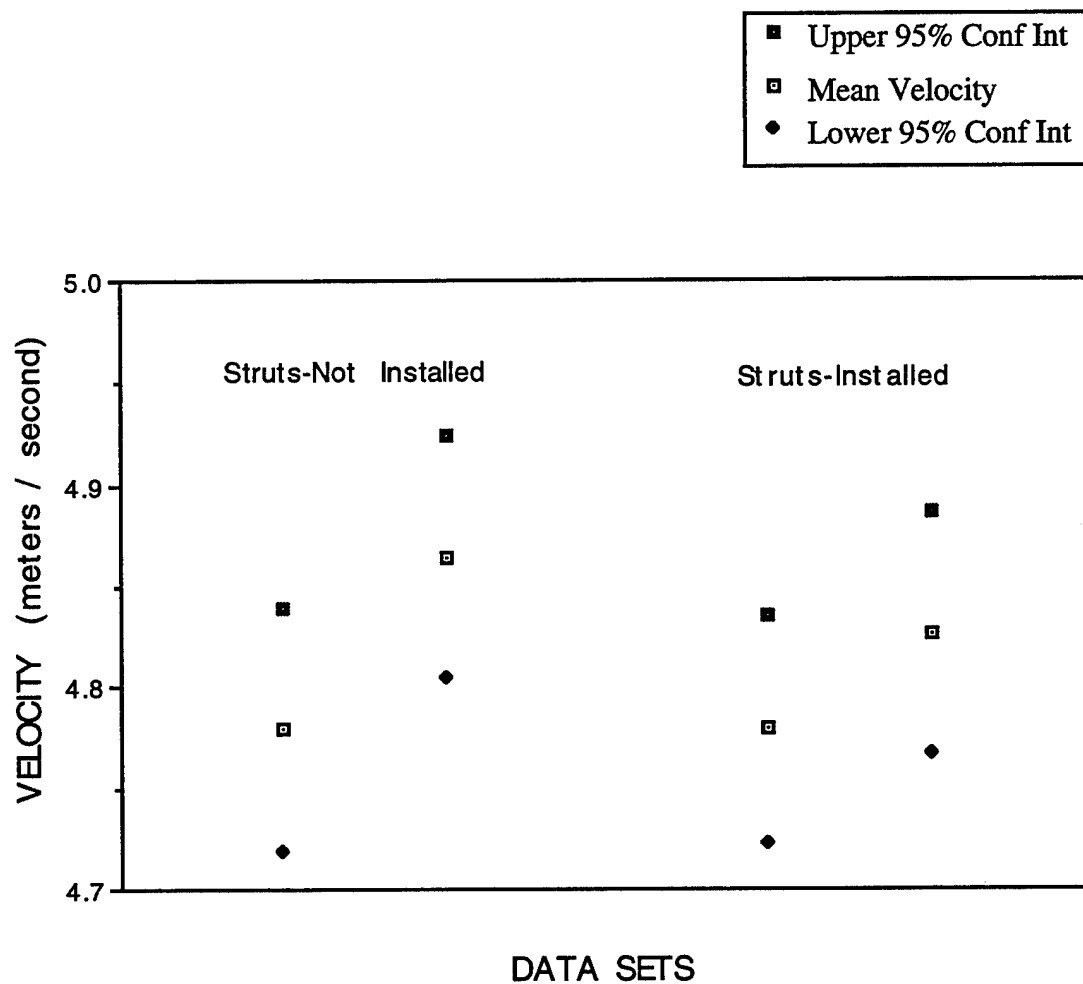
Point I/ Mid Level

Data

POINT	STRUTS	COMPONENT	MEAN	STD DEV	POINTS	95% CONF INT	LOW	HIGH
I	OFF	X	4.779	0.985	1013	0.061	4.718	4.840
I	OFF	X	4.864	0.982	1015	0.060	4.804	4.924
I	ON	X	4.779	0.924	1010	0.057	4.722	4.836
I	ON	X	4.827	0.969	1012	0.060	4.767	4.887
I	OFF	Y	2.467	0.411	1022	0.025	2.442	2.492
I	OFF	Y	2.390	0.422	1022	0.026	2.364	2.416
I	ON	Y	2.424	0.439	1021	0.027	2.397	2.451
I	ON	Y	2.447	0.410	1021	0.025	2.422	2.472
I	OFF	Z	6.369	1.086	1015	0.067	6.302	6.436
I	OFF	Z	6.411	1.127	1019	0.069	6.342	6.480
I	ON	Z	6.420	1.111	1020	0.068	6.352	6.488
I	ON	Z	6.399	1.107	1021	0.068	6.331	6.467

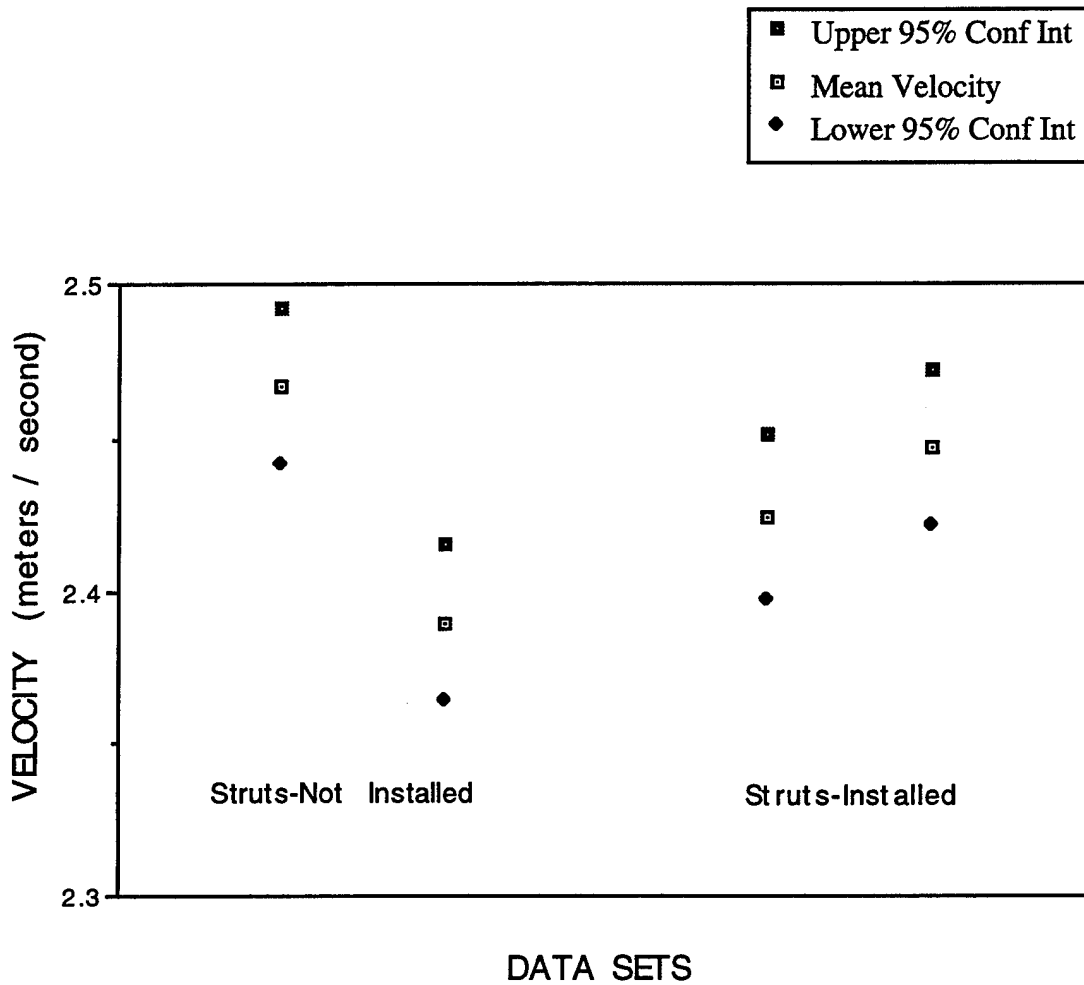
Point I / Mid Level / X- Component

Mean Velocity Components for Data Sets with
Upper and Lower Bounds of 95 % Confidence Intervals



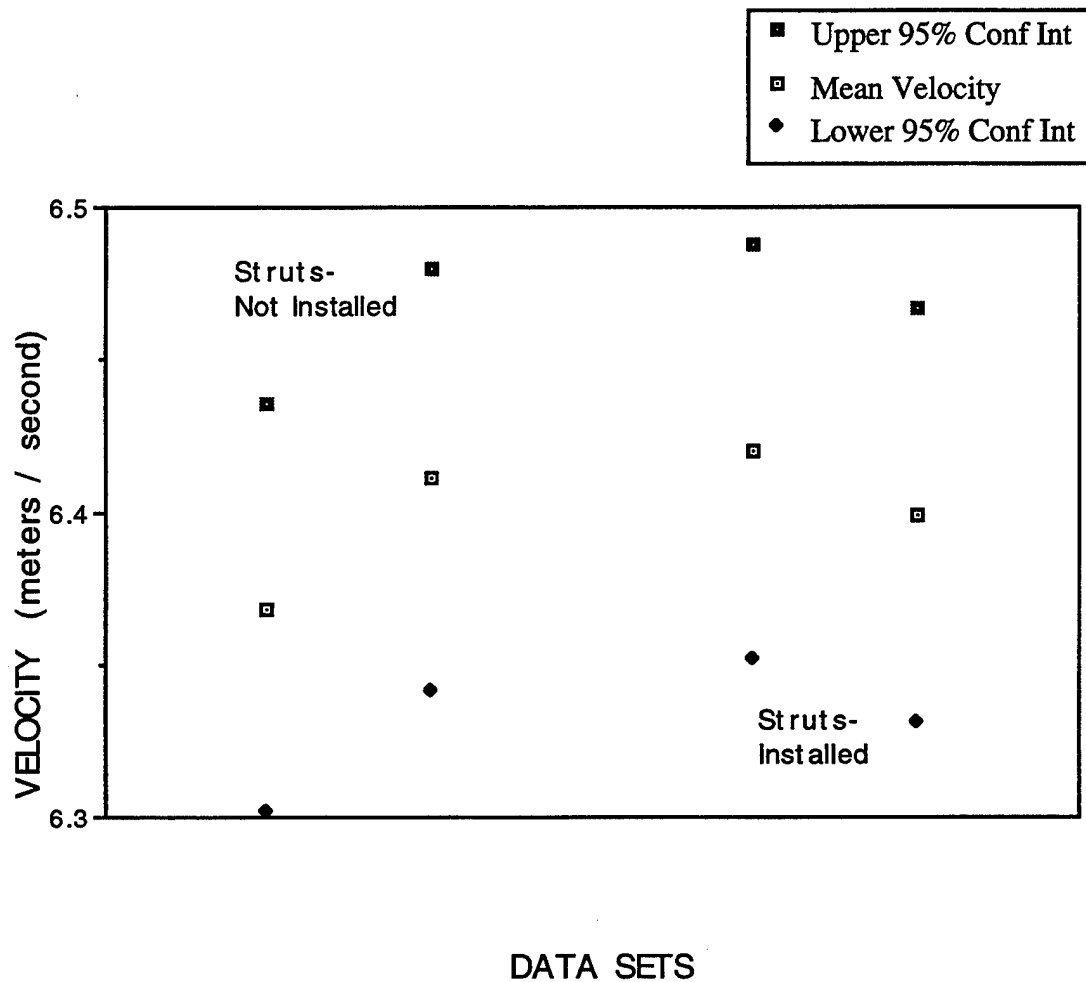
Point I / Mid Level / Y- Component

Mean Velocity Components for Data Sets with
Upper and Lower Bounds of 95 % Confidence Intervals



Point I / Mid Level / Z- Component

Mean Velocity Components for Data Sets with
Upper and Lower Bounds of 95 % Confidence Intervals



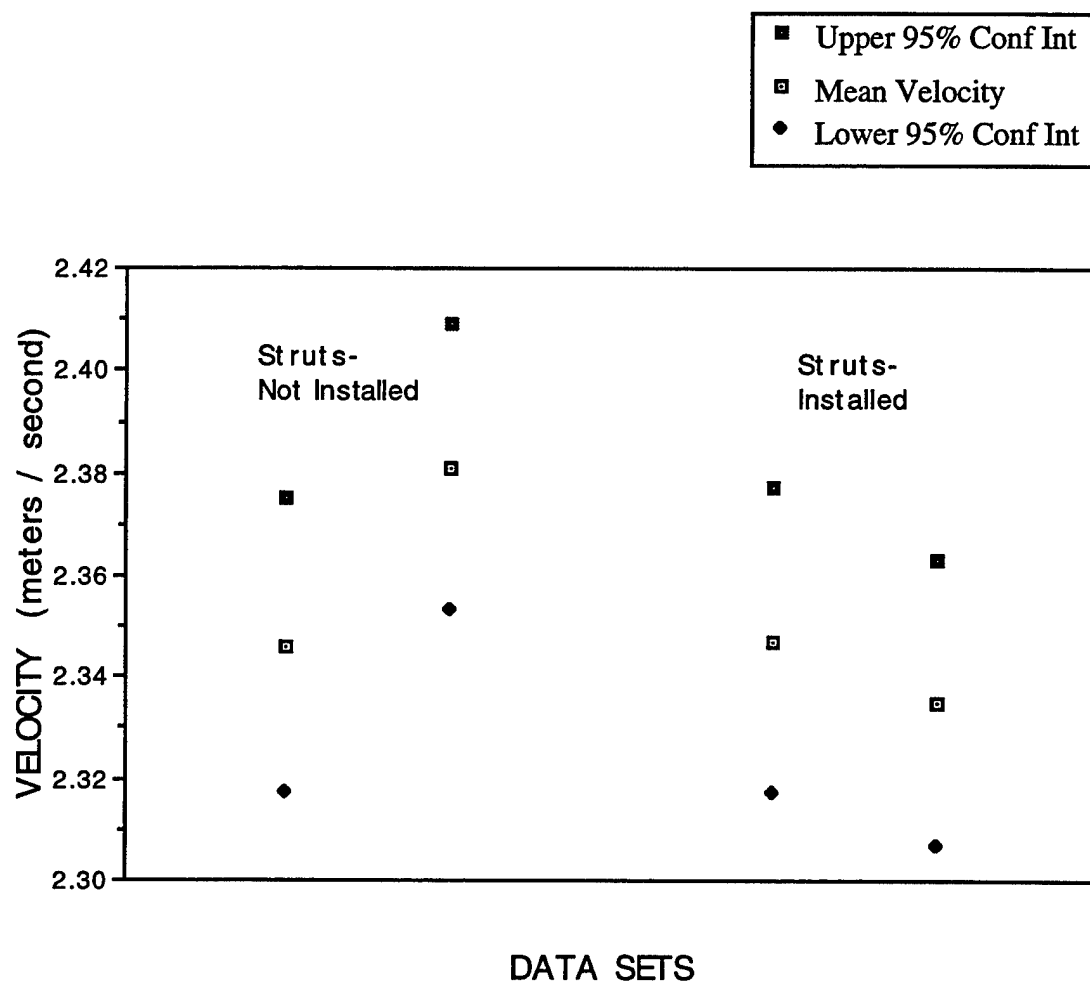
Point D/ Upper Level

Data

POINT	STRUTS	COMPONENT	MEAN	STD DEV	POINTS	95% CONF INT	LOW	HIGH
D	OFF	X	2.346	0.474	1022	0.029	2.317	2.375
D	OFF	X	2.381	0.452	1018	0.028	2.353	2.409
D	ON	X	2.347	0.489	1024	0.030	2.317	2.377
D	ON	X	2.335	0.451	1021	0.028	2.307	2.363
D	OFF	Y	5.460	1.001	1013	0.062	5.398	5.522
D	OFF	Y	5.435	0.992	1015	0.061	5.374	5.496
D	ON	Y	5.459	1.011	1014	0.062	5.397	5.521
D	ON	Y	5.456	0.986	1013	0.061	5.395	5.517
D	OFF	Z	2.680	0.376	1021	0.023	2.657	2.703
D	OFF	Z	2.683	0.407	1024	0.025	2.658	2.708
D	ON	Z	2.687	0.444	1024	0.027	2.660	2.714
D	ON	Z	2.681	0.418	1023	0.026	2.655	2.707

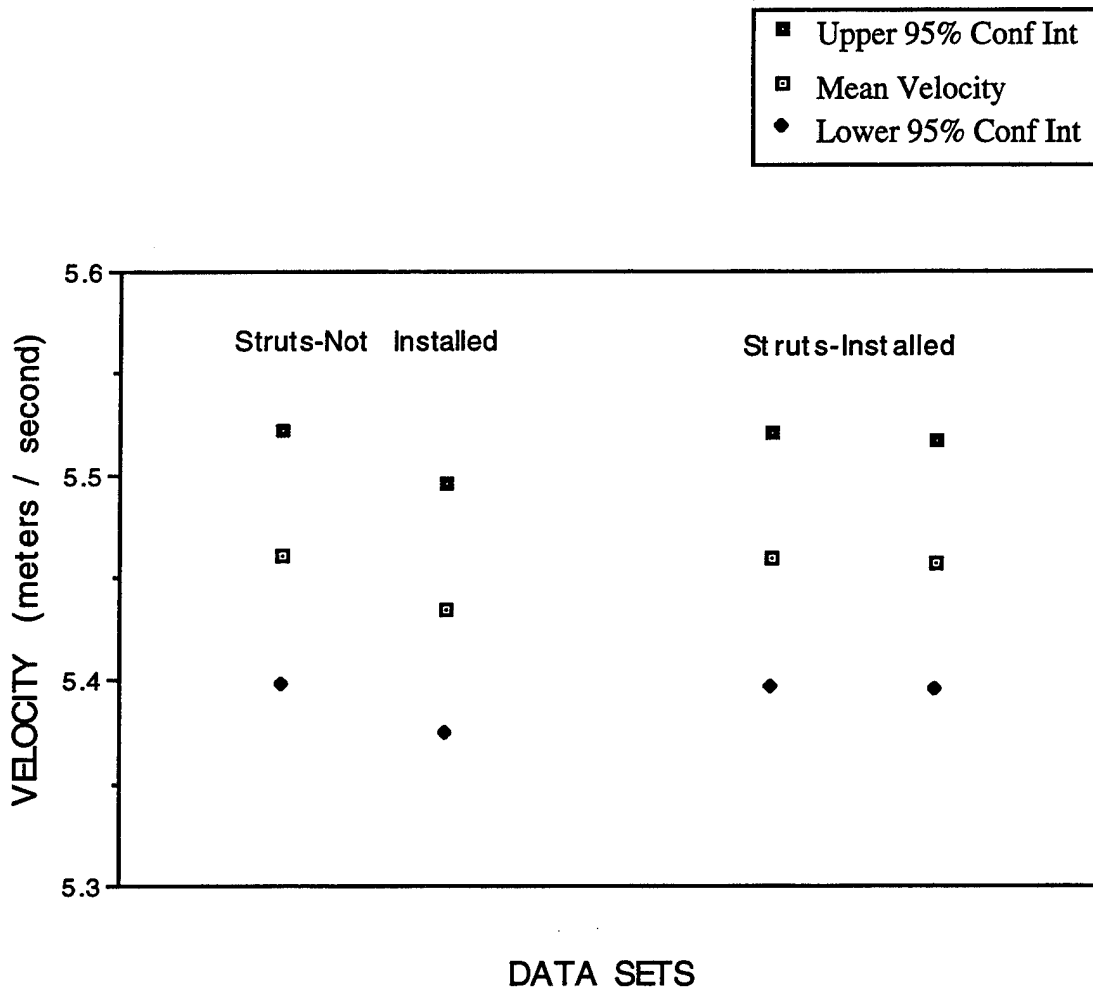
Point D / Upper Level / X- Component

Mean Velocity Components for Data Sets with
Upper and Lower Bounds of 95 % Confidence Intervals



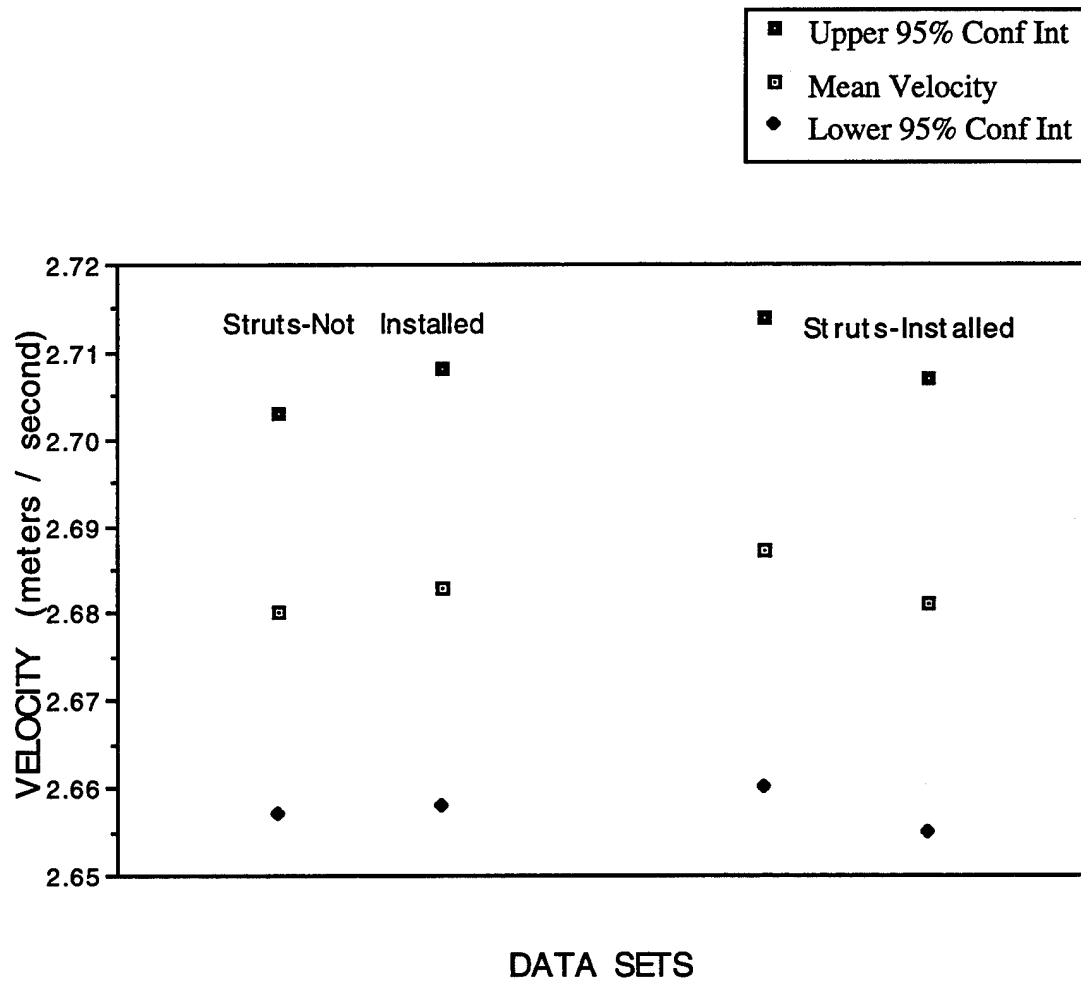
Point D / Upper Level / Y- Component

Mean Velocity Components for Data Sets with
Upper and Lower Bounds of 95 % Confidence Intervals



Point D / Upper Level / Z- Component

Mean Velocity Components for Data Sets with
Upper and Lower Bounds of 95 % Confidence Intervals



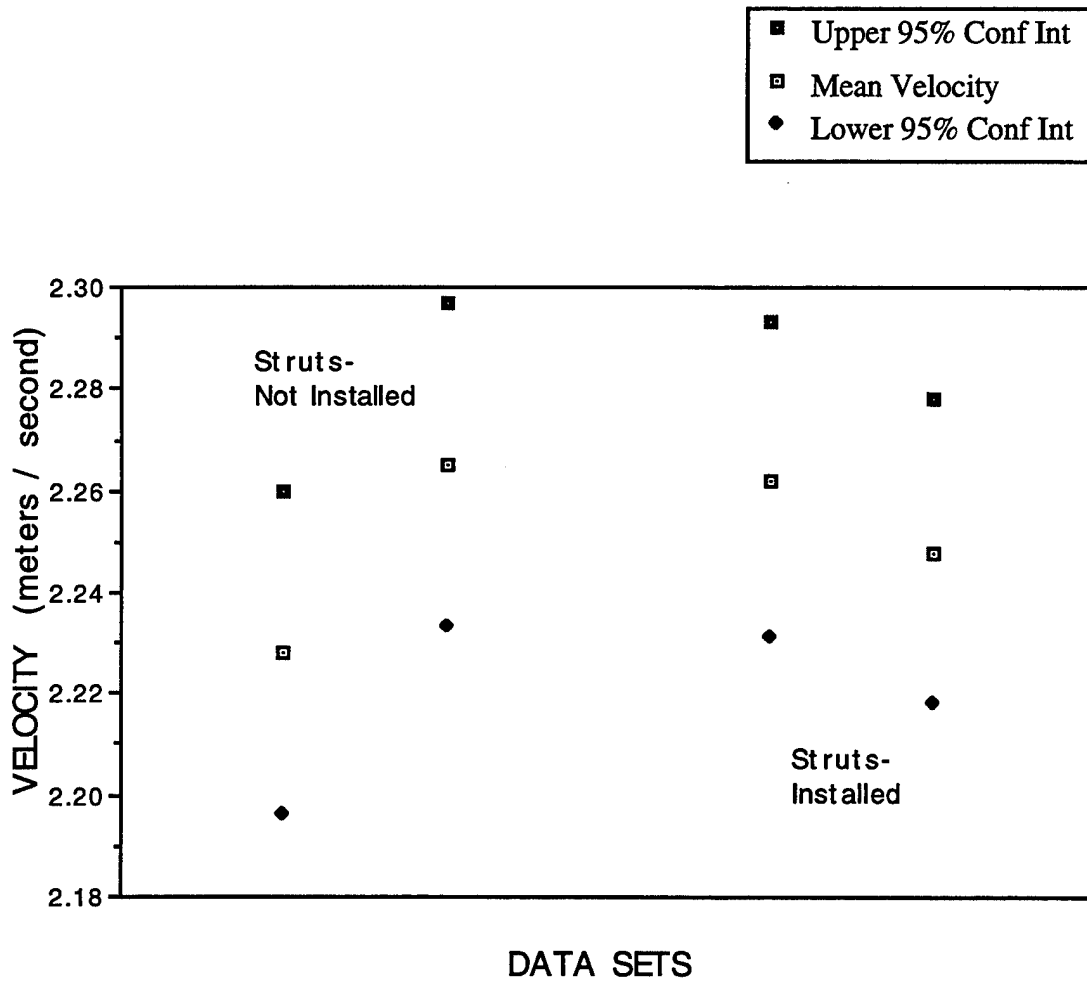
Point E/ Upper Level

Data

POINT	STRUTS	COMPONENT	MEAN	STD DEV	POINTS	95% CONF INT	LOW	HIGH
E	OFF	X	2.228	0.522	1023	0.032	2.196	2.260
E	OFF	X	2.265	0.522	1024	0.032	2.233	2.297
E	ON	X	2.262	0.506	1024	0.031	2.231	2.293
E	ON	X	2.248	0.495	1023	0.030	2.218	2.278
E	OFF	Y	1.711	0.777	1019	0.048	1.663	1.759
E	OFF	Y	1.538	0.914	1018	0.056	1.482	1.594
E	ON	Y	1.594	0.941	1018	0.058	1.536	1.652
E	ON	Y	1.667	0.964	1022	0.059	1.608	1.726
E	OFF	Z	0.628	0.230	1016	0.014	0.614	0.642
E	OFF	Z	0.581	0.202	1013	0.012	0.568	0.593
E	ON	Z	0.616	0.216	1013	0.013	0.602	0.629
E	ON	Z	0.590	0.230	1016	0.014	0.576	0.604

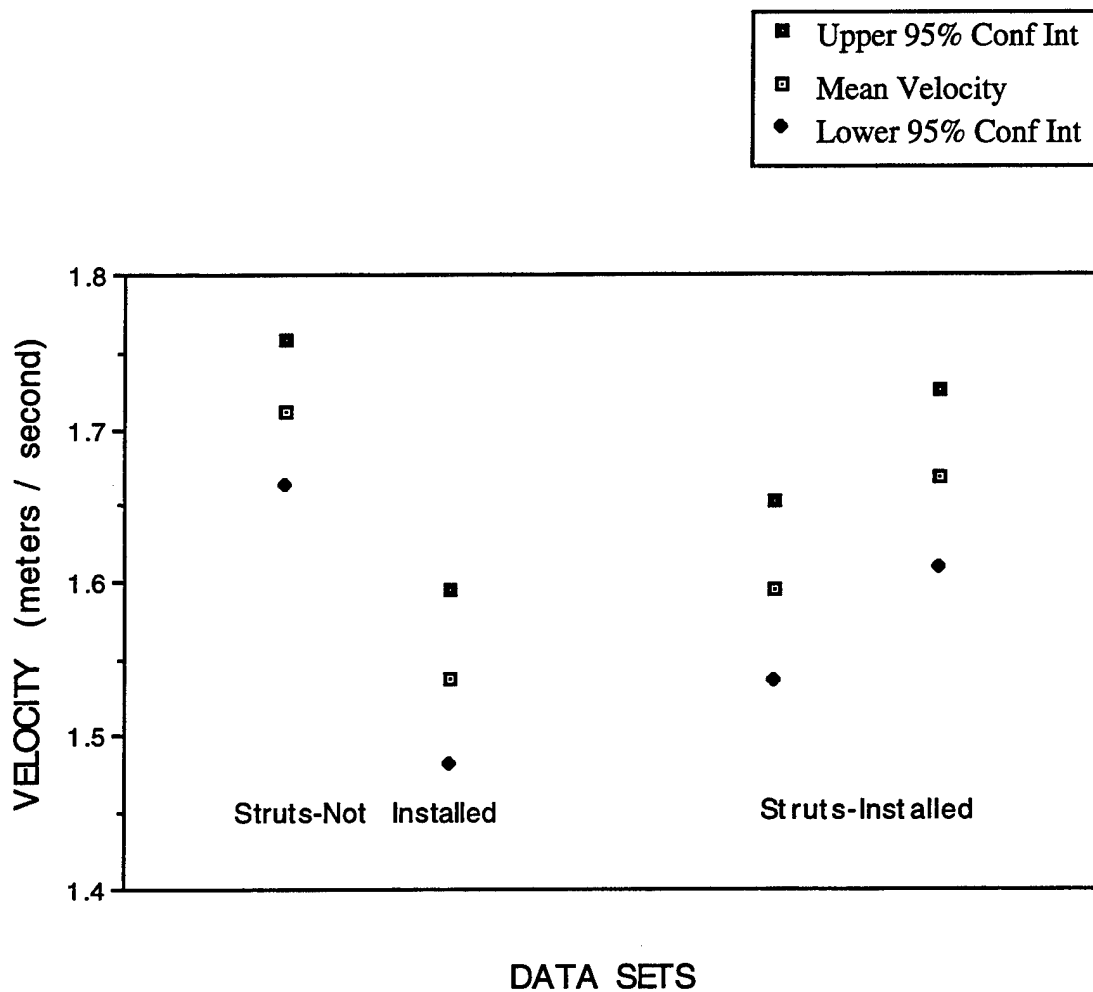
Point E / Upper Level / X- Component

Mean Velocity Components for Data Sets with
Upper and Lower Bounds of 95 % Confidence Intervals



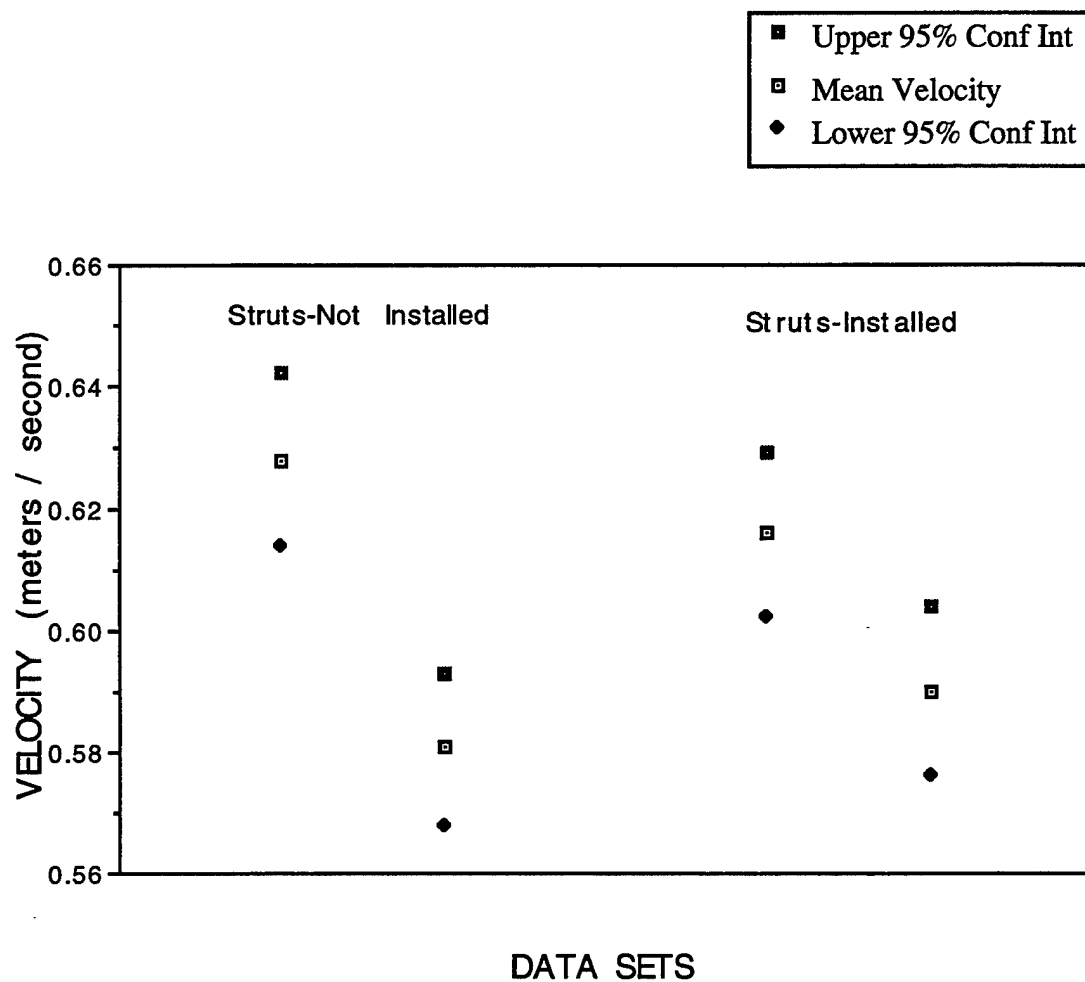
Point E / Upper Level / Y- Component

Mean Velocity Components for Data Sets with
Upper and Lower Bounds of 95 % Confidence Intervals



Point E / Upper Level / Z- Component

Mean Velocity Components for Data Sets with
Upper and Lower Bounds of 95 % Confidence Intervals



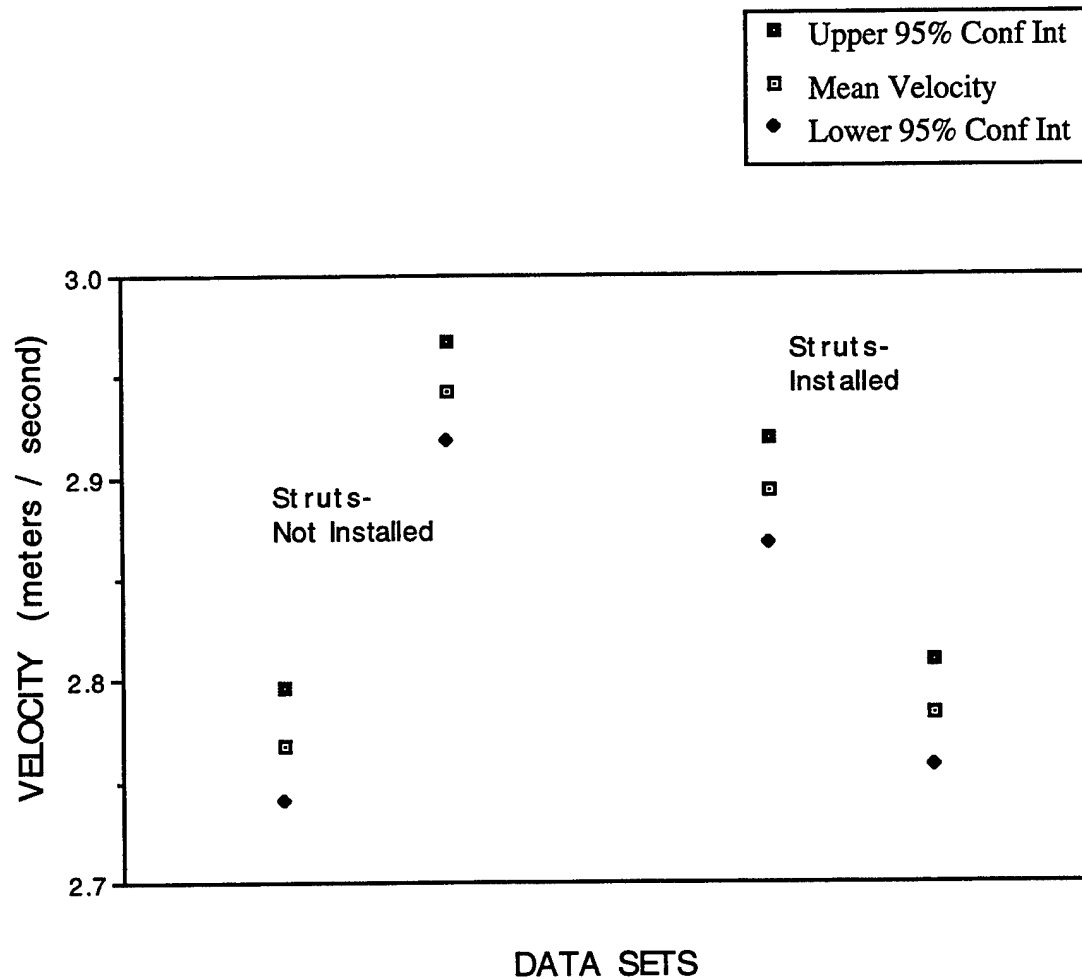
Point F/ Upper Level

Data

POINT	STRUTS	COMPONENT	MEAN	STD DEV	POINTS	95% CONF INT	LOW	HIGH
F	OFF	X	2.768	0.458	1022	0.028	2.740	2.796
F	OFF	X	2.943	0.400	1019	0.025	2.918	2.968
F	ON	X	2.893	0.431	1017	0.026	2.867	2.919
F	ON	X	2.784	0.430	1021	0.026	2.758	2.810
F	OFF	Y	-1.025	0.777	1020	0.048	-1.073	-0.977
F	OFF	Y	-0.884	0.695	1021	0.043	-0.927	-0.841
F	ON	Y	-0.951	0.727	1023	0.045	-0.995	-0.906
F	ON	Y	-0.959	0.687	1021	0.042	-1.001	-0.917
F	OFF	Z	2.938	0.390	1022	0.024	2.914	2.962
F	OFF	Z	2.911	0.377	1022	0.023	2.888	2.934
F	ON	Z	2.917	0.383	1023	0.023	2.894	2.940
F	ON	Z	2.925	0.381	1024	0.023	2.902	2.948

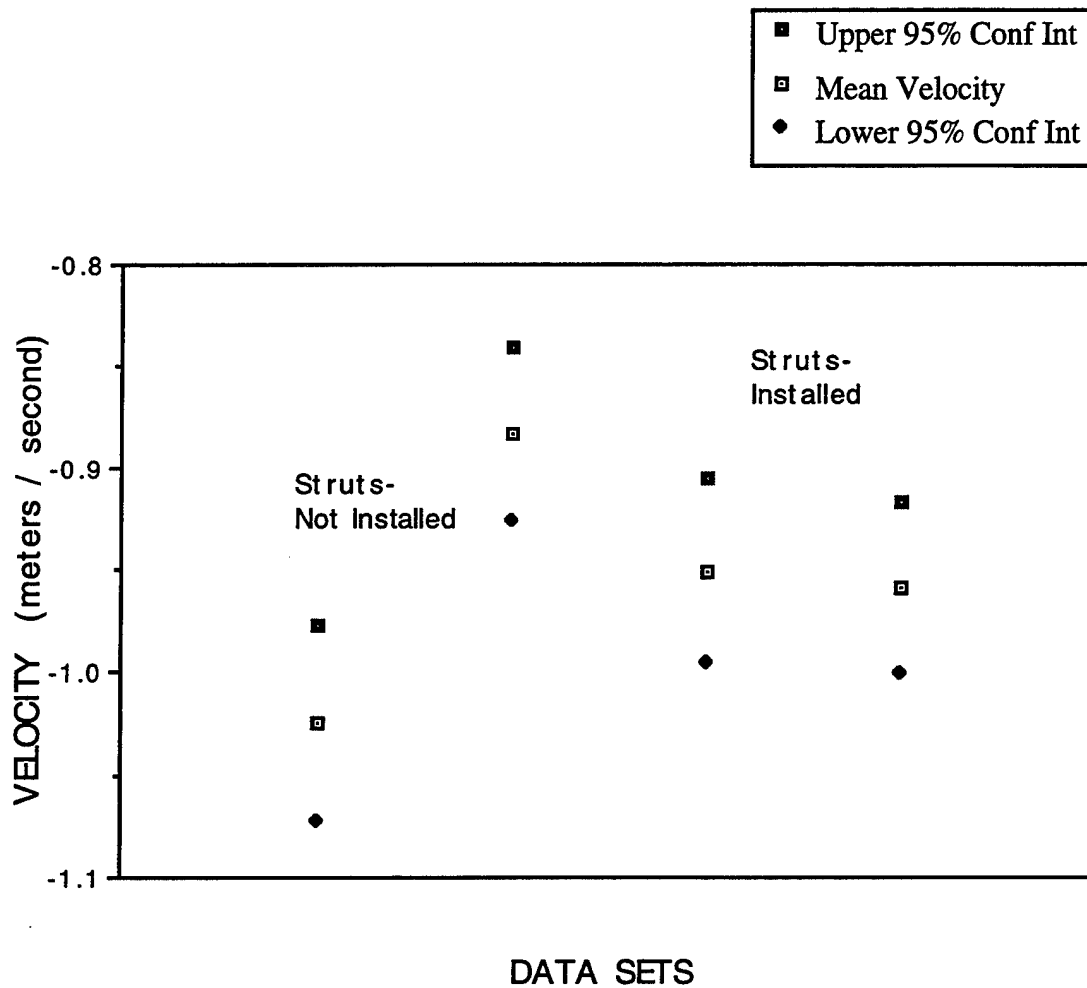
Point F / Upper Level / X- Component

Mean Velocity Components for Data Sets with
Upper and Lower Bounds of 95 % Confidence Intervals



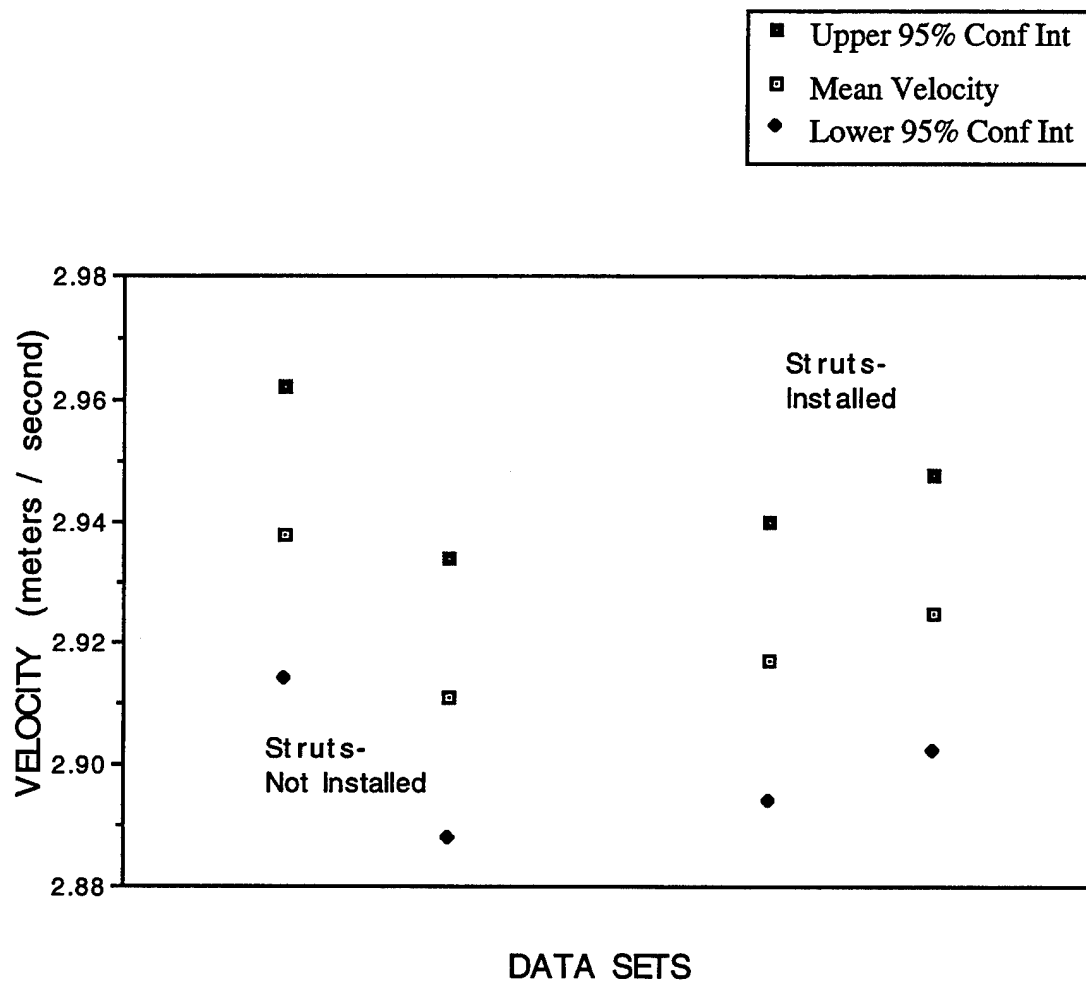
Point F / Upper Level / Y- Component

Mean Velocity Components for Data Sets with
Upper and Lower Bounds of 95 % Confidence Intervals



Point F / Upper Level / Z- Component

Mean Velocity Components for Data Sets with
Upper and Lower Bounds of 95 % Confidence Intervals



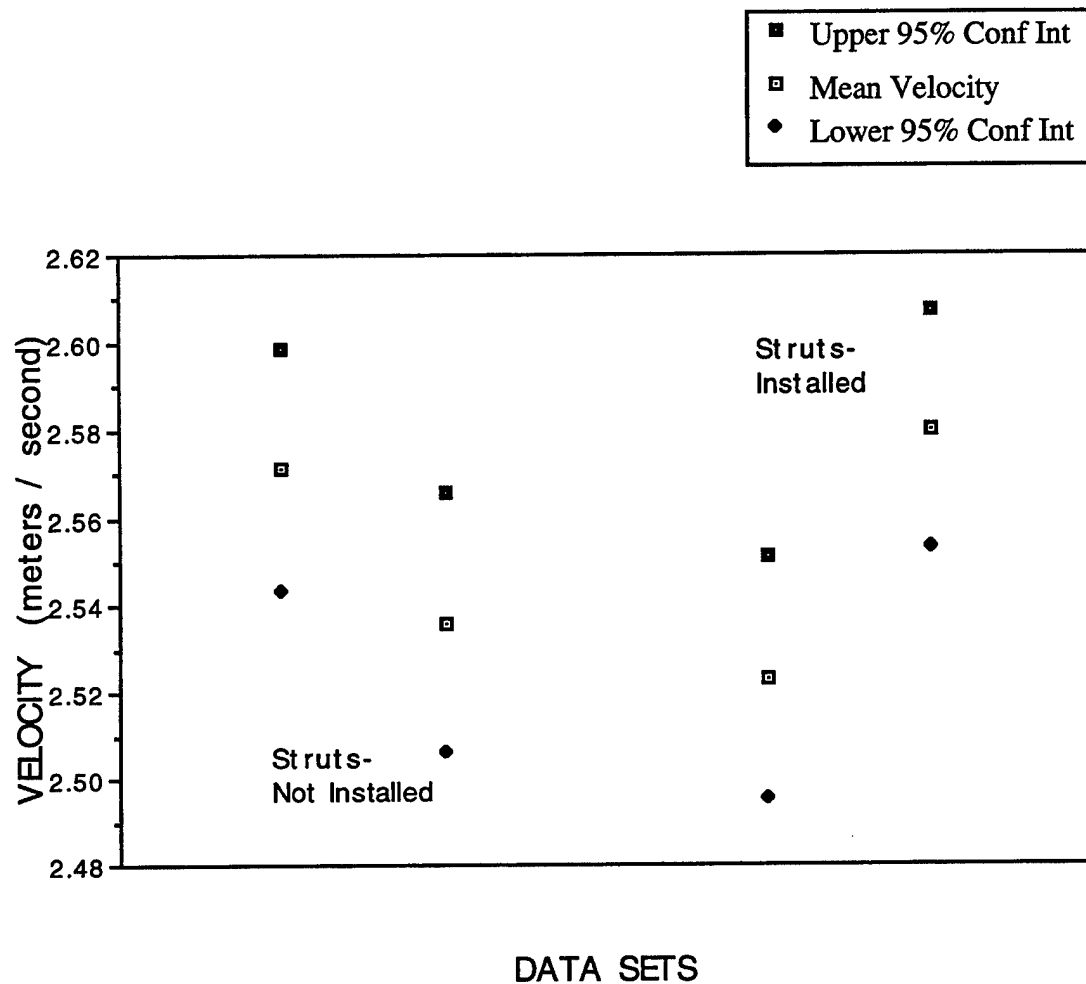
Point G/Upper Level

Data

POINT	STRUTS	COMPONENT	MEAN	STD DEV	POINTS	95% CONF INT	LOW	HIGH
G	OFF	X	2.571	0.453	1020	0.028	2.543	2.599
G	OFF	X	2.536	0.488	1022	0.030	2.506	2.566
G	ON	X	2.523	0.449	1020	0.028	2.495	2.551
G	ON	X	2.580	0.438	1020	0.027	2.553	2.607
G	OFF	Y	5.367	0.954	1020	0.059	5.308	5.426
G	OFF	Y	5.357	1.077	1024	0.066	5.291	5.423
G	ON	Y	5.361	1.101	1020	0.068	5.293	5.429
G	ON	Y	5.338	1.033	1016	0.064	5.274	5.402
G	OFF	Z	2.723	0.438	1023	0.027	2.696	2.750
G	OFF	Z	2.711	0.439	1000	0.027	2.684	2.738
G	ON	Z	2.709	0.413	1015	0.025	2.684	2.734
G	ON	Z	2.720	0.425	1000	0.026	2.694	2.746

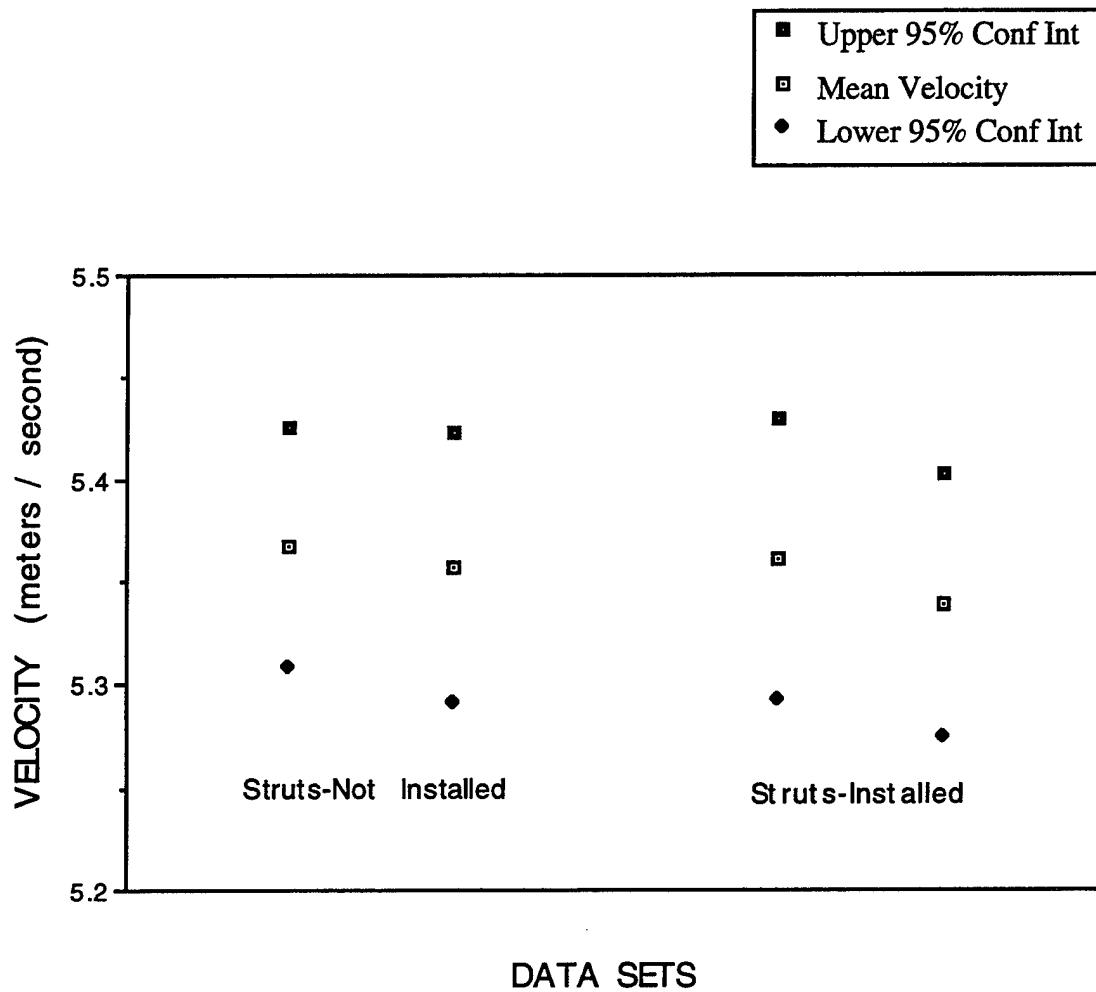
Point G / Upper Level / X- Component

Mean Velocity Components for Data Sets with
Upper and Lower Bounds of 95 % Confidence Intervals



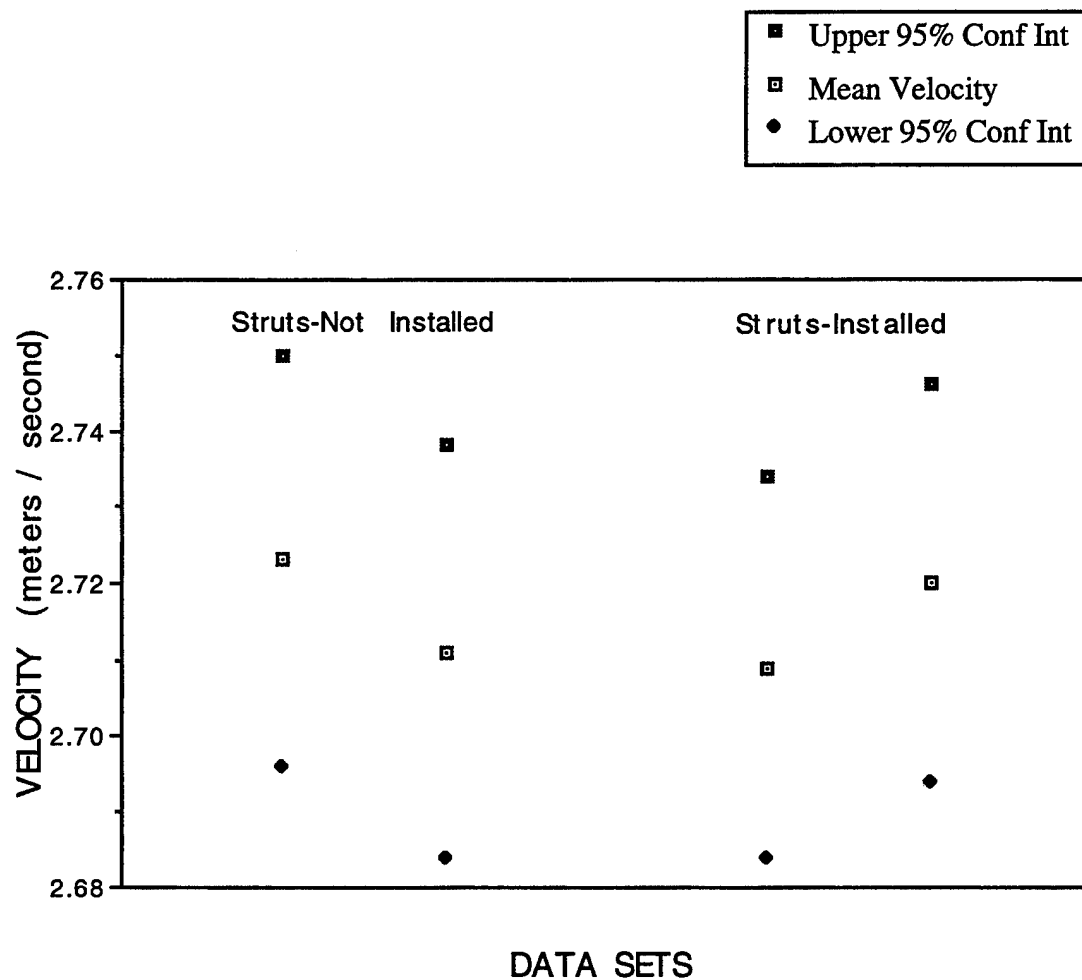
Point G / Upper Level / Y- Component

Mean Velocity Components for Data Sets with
Upper and Lower Bounds of 95 % Confidence Intervals



Point G / Upper Level / Z- Component

Mean Velocity Components for Data Sets with
Upper and Lower Bounds of 95 % Confidence Intervals



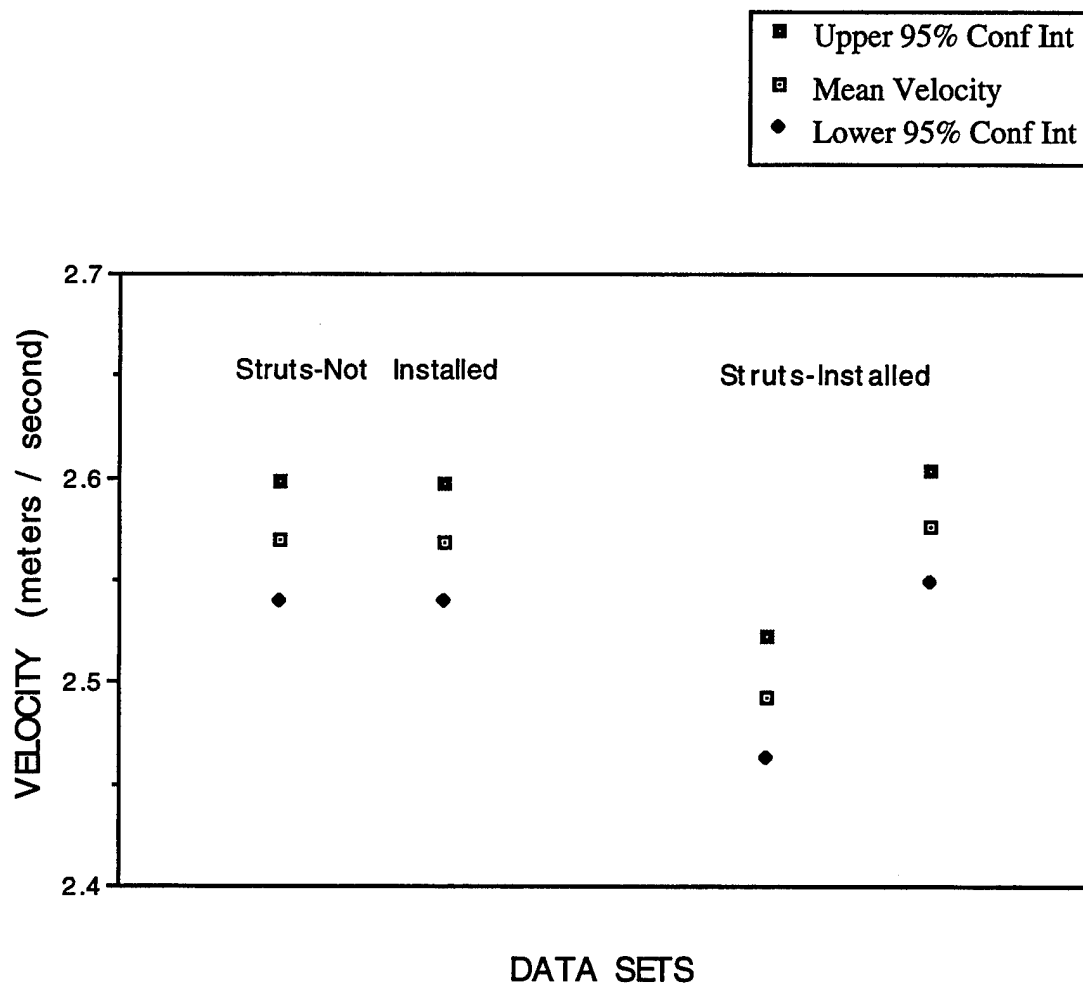
Point H/ Upper Level

Data

POINT	STRUTS	COMPONENT	MEAN	STD DEV	POINTS	95% CONF INT	LOW	HIGH
H	OFF	X	2.569	0.480	1024	0.029	2.540	2.598
H	OFF	X	2.568	0.467	1021	0.029	2.539	2.597
H	ON	X	2.492	0.487	1023	0.030	2.462	2.522
H	ON	X	2.576	0.444	1020	0.027	2.549	2.603
H	OFF	Y	4.836	0.974	1016	0.060	4.776	4.896
H	OFF	Y	4.858	1.036	1020	0.064	4.794	4.922
H	ON	Y	4.796	1.032	1017	0.063	4.733	4.859
H	ON	Y	4.837	1.005	1017	0.062	4.775	4.899
H	OFF	Z	2.780	0.447	1020	0.027	2.753	2.807
H	OFF	Z	2.783	0.460	1021	0.028	2.755	2.811
H	ON	Z	2.780	0.452	1021	0.028	2.752	2.808
H	ON	Z	2.778	0.456	1024	0.028	2.750	2.806

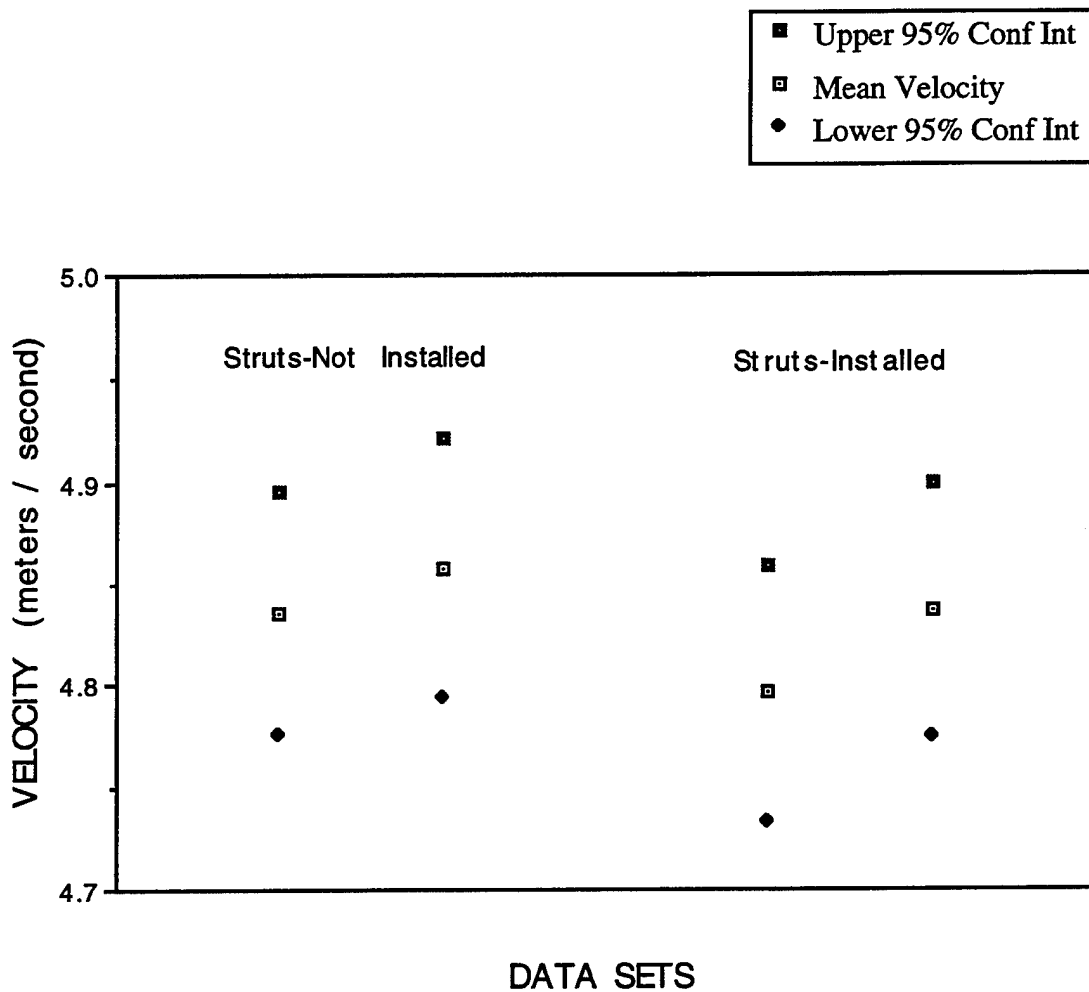
Point H / Upper Level / X- Component

Mean Velocity Components for Data Sets with
Upper and Lower Bounds of 95 % Confidence Intervals



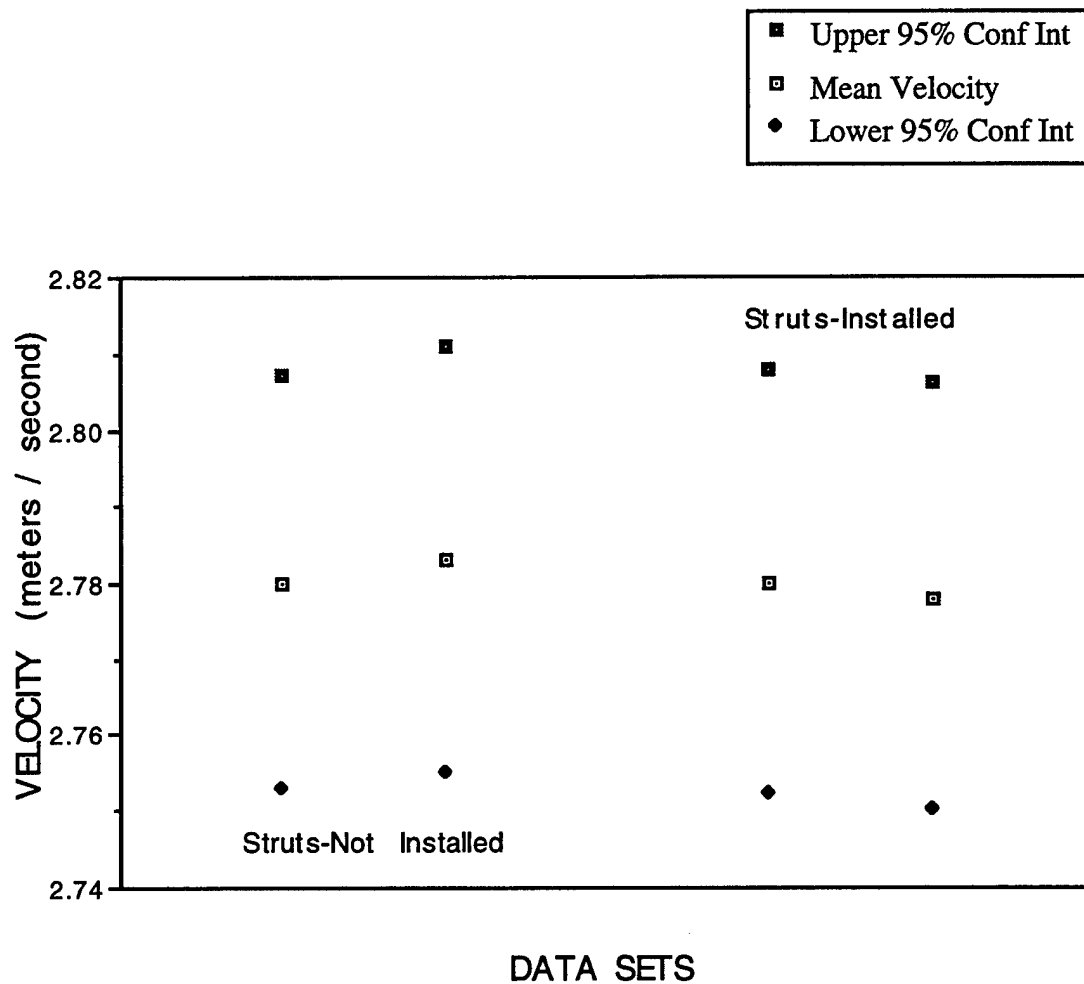
Point H / Upper Level / Y- Component

Mean Velocity Components for Data Sets with
Upper and Lower Bounds of 95 % Confidence Intervals



Point H / Upper Level / Z- Component

Mean Velocity Components for Data Sets with
Upper and Lower Bounds of 95 % Confidence Intervals



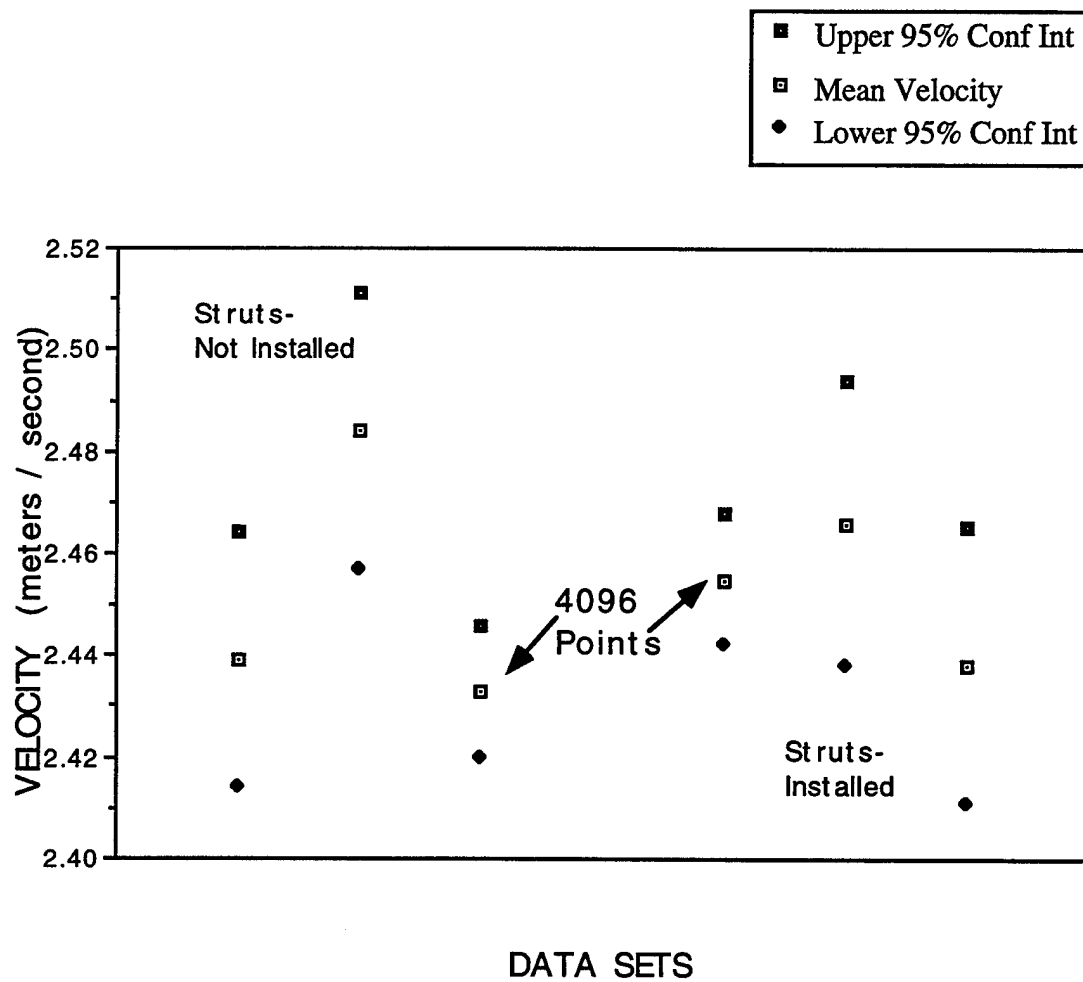
Point I/ Upper Level

Data

POINT	STRUTS	COMPONENT	MEAN	STD DEV	POINTS	95% CONF INT	LOW	HIGH
I	OFF	X	2.439	0.410	1022	0.025	2.414	2.464
I	OFF	X	2.484	0.438	1022	0.027	2.457	2.511
I	OFF	X	2.433	0.434	4090	0.013	2.420	2.446
I	ON	X	2.455	0.429	4089	0.013	2.442	2.468
I	ON	X	2.466	0.455	1023	0.028	2.438	2.494
I	ON	X	2.438	0.439	1024	0.027	2.411	2.465
I	OFF	Y	4.234	1.118	1018	0.069	4.165	4.303
I	OFF	Y	4.323	1.104	1017	0.068	4.255	4.391
I	ON	Y	4.239	1.060	1020	0.065	4.174	4.304
I	ON	Y	4.211	1.136	1022	0.070	4.141	4.281
I	OFF	Z	5.687	0.680	1020	0.042	5.645	5.729
I	OFF	Z	5.688	0.684	1023	0.042	5.646	5.730
I	ON	Z	5.692	0.628	1024	0.038	5.654	5.730
I	ON	Z	5.687	0.685	1021	0.042	5.645	5.729

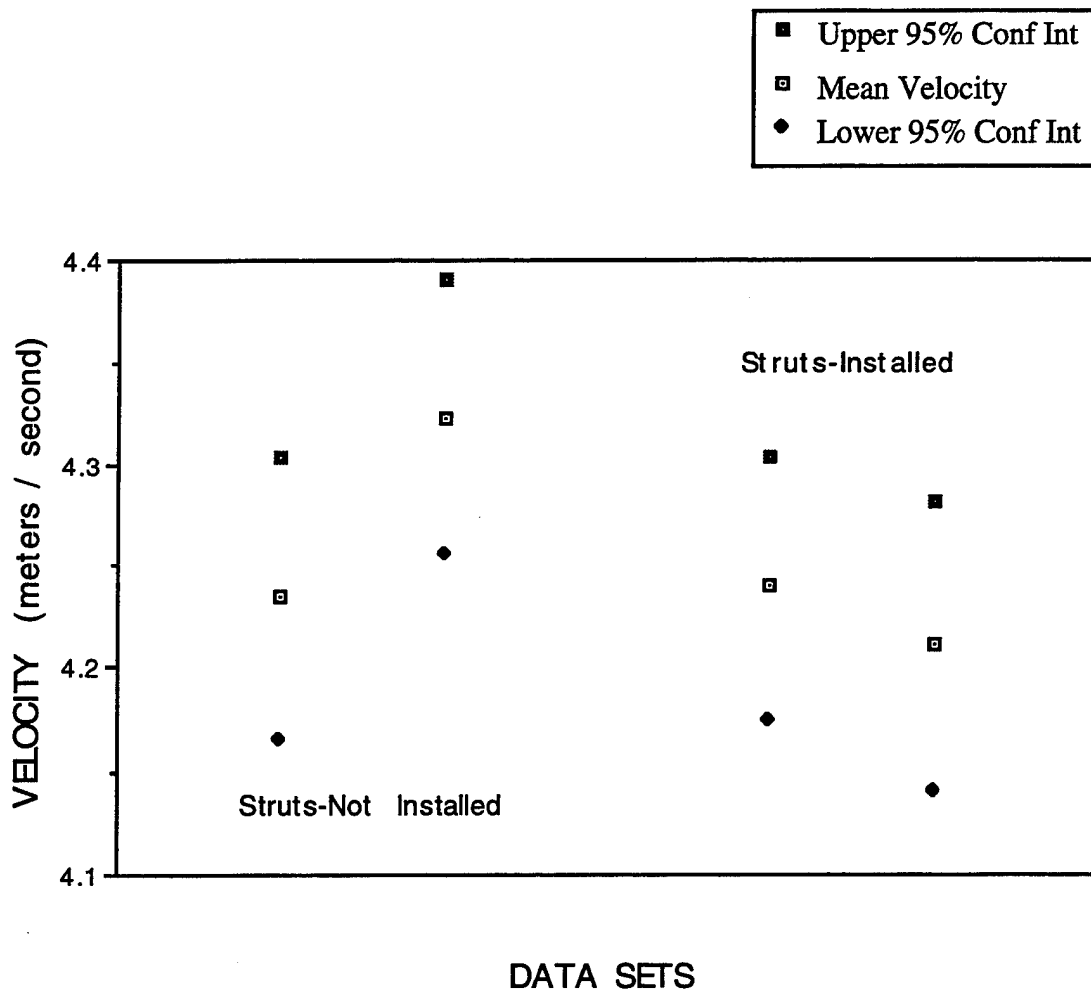
Point I / Upper Level / X- Component

Mean Velocity Components for Data Sets with
Upper and Lower Bounds of 95 % Confidence Intervals



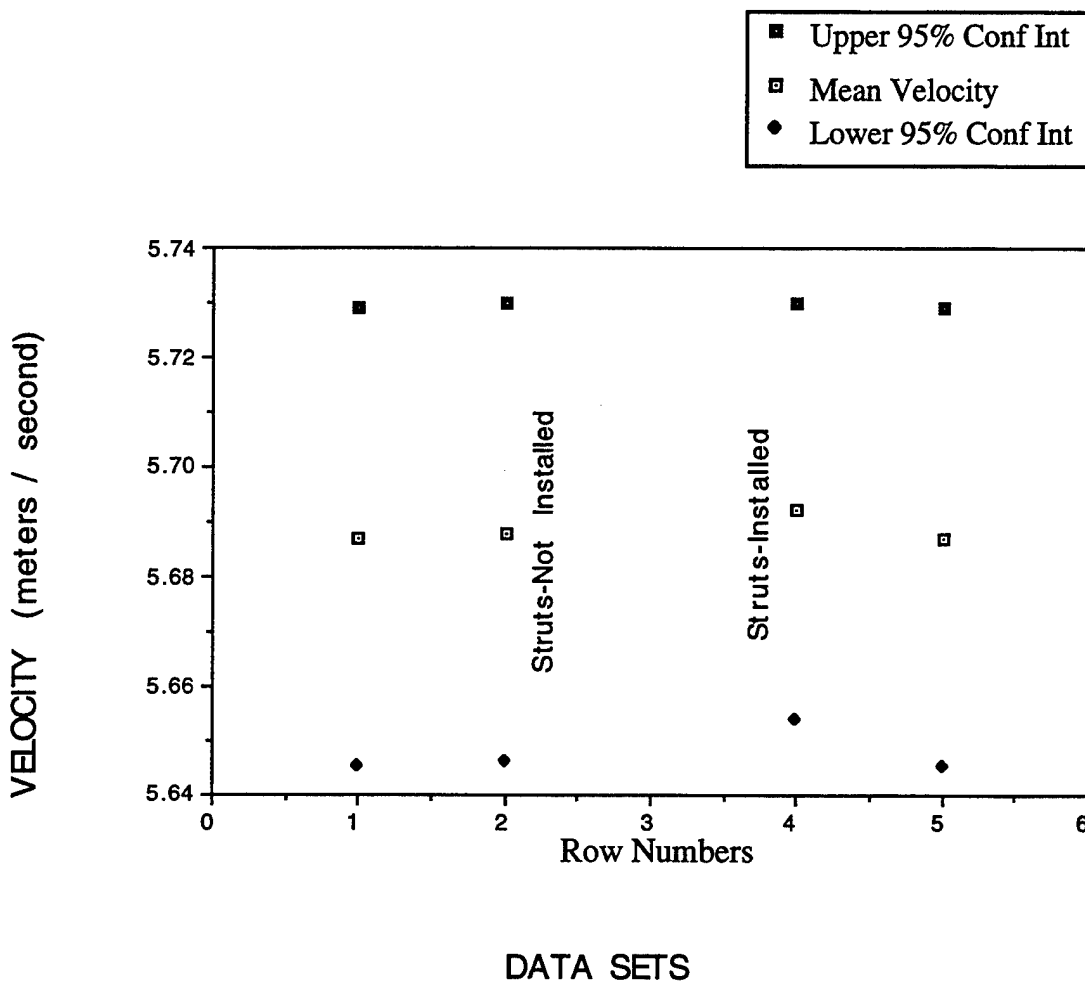
Point I / Upper Level / Y- Component

Mean Velocity Components for Data Sets with
Upper and Lower Bounds of 95 % Confidence Intervals



Point 1 / Upper Level / Z- Component

Mean Velocity Components for Data Sets with
Upper and Lower Bounds of 95 % Confidence Intervals



REFERENCES

1. Morrocco, John D., "House Merges Funds for JAST and ASTOVL", Aviation Week and Space Technology, May 16, 1994.
2. Platzer, M. F. and Margason, R. J., "Prediction Methods for Jet V/STOL Propulsion Aerodynamics", Journal of Aircraft, Volume 15, Number 2, February 1978.
3. Dooley, W. An Experimental Investigation of Jet-Induced Ground Effects and Support Strut Interference on a STOVL Configuration in Hover, Masters Thesis, Naval Postgraduate School, Monterey, California, June 1994.
4. Margason R. J., "CALF Thrust and Effective Velocity Ratio", NASA Ames Research Center, 3 May 1994, (Unpublished).
5. Instruction Manual, Air Cooled Argon Laser Model 543, Omnichrome Incorporated, 09 December 1992.
6. Instruction Manual, Two-component Fiberoptic Probe System, Revision A, TSI Incorporated, October 1987.
7. Instruction Manual, Model 9201 Colorburst Multicolor Beam Separator, Revision A, TSI Incorporated, October 1990.
8. Instruction Manual, Flow Information Display (FIND) Software Version 3.5, TSI Incorporated, January 1992.
9. Instruction Manual, Model IFA 550 LDV Signal Processor, Revision b, TSI Incorporated, February 1988.
10. Instruction Manual, Rosco Model 1500 Fog Machine, Rosco Laboratories Incorporated, September 1984.
11. Holman, J. P. , Experimental Methods for Engineers , Fifth Edition, McGraw-Hill, Inc., 1989.
12. Horne, C. , "LDV Measurement Statistical Attributes", NASA Ames Research Center, 15 February 1994, (Unpublished).
13. Goldstein, R. J., Fluid Mechanics Measurements, Hemisphere Publishing Company, 1983.

14. Elazar, Y. , A Mapping of viscous Flow Behavior in a Controlled Diffusion Compressor Cascade using Laser Doppler Velocimetry and Preliminary Evaluation of Codes for the Prediction of Stall, Ph.D. Dissertation, Naval Postgraduate School, Monterey, California, March 1988.
15. Dober, D. M., Three-Dimensional Fiber-Optic LDV Measurements of the Endwall Region of a Linear Cascade of Controlled Diffusion Stator Blades, Masters Thesis, Naval Postgraduate School, Monterey, California, March 1993.

INITIAL DISTRIBUTION LIST

	<u>Addressee</u>	<u>Number of Copies</u>
1.	Defense Technical Information Center Cameron Station Alexandria, VA 22304-6145	2
2.	Library, Code 52 Naval Postgraduate School Monterey, CA 93943-5000	2
3.	Chairman, Code AA/Co Naval Postgraduate School Monterey, CA 93943-5000	1
4.	Professor S. K. Hebbbar, Code AA/Hb Naval Postgraduate School Monterey, CA 93943-5000	5
5.	Professor M. F. Platzer, Code AA/Pl Naval Postgraduate School Monterey, CA 93943-5000	2
6.	CDR Edgar R. Enochs Director, Cruise Missiles Test and Evaluation (PEO(CU)-CT) Program Executive Officer Cruise Missiles Project and Unmanned Air Vehicles Joint Project Washington, D. C. 20361-1014	2
7.	Michael J. Harris Aircraft Division Code AIR-931 Naval Air Systems Command Washington, D. C. 20361-9320	1
8.	Richard J. Margason Code FFF, M. S. 247-2 NASA Ames Research Center Moffett Field, CA 94035-1000	1
9.	Larry Olson Chief, Code FFF, M. S. 247-2 NASA Ames Research Center Moffett Field, CA 94035-1000	1

- | | | |
|-----|---|---|
| 10. | Sam Wilson
Manager, STOVL/CALF Project
Code FPP, M. S. 237-2
NASA Ames Research Center
Moffett Field, CA 94035-1000 | 1 |
| | | |
| 11. | Doug Wardwell
Aerodynamics Manager, STOVL/CALF Project
Code FPP, M. S. 237-2
NASA Ames Research Center
Moffett Field, CA 94035-1000 | 1 |
| | | |
| 12. | Marvin Walters
Naval Air Warfare Center, Aircraft Division
Street Road
Warminster, PA 18974-5000 | 1 |
| | | |
| 13. | Tim Naumowicz/ Craig Hange/ Tom Arledge
Code FFF, M. S. 247-2
NASA Ames Research Center
Moffett Field, CA 94035-1000 | 3 |
| | | |
| 14. | Paul Atkins/ Gavin Botha
Test Director, STOVL/CALF Project
Code FFN, M. S. 221-5
NASA Ames Research Center
Moffett Field, CA 94035-1000 | 2 |